DOCTORAL SCHOOL
MEDITERRANEA UNIVERSITY OF REGGIO CALABRIA

DEPARTMENT OF INFORMATION ENGINEERING, INFRASTRUCTURES
AND SUSTAINABLE ENERGY
(DIIES)

PHD IN
INFORMATION ENGINEERING

S.S.D. ING-INF/01
XXXVI CYCLE

Silicon Carbide photonic integrated circuits: study of material physical properties and design, fabrication and characterization of innovative active devices

CANDIDATE
Elisa Demetra MALLEMACE

ADVISORS
Prof. Francesco Giuseppe DELLA CORTE
Prof. Sandro RAO

CO-ADVISOR
Dr. Maurizio CASALINO

COORDINATOR
Prof. Antonella MOLINARO

REGGIO CALABRIA, FEBRUARY 2024

Finito di stampare nel mese di **XXX 2024**

Edizione

Quaderno N. XX

Collana *XXXXXXXX*
Curatore *XXX*

ISBN XXX-XX-XXXXX-XX-X

Università degli Studi *Mediterranea* di Reggio Calabria
Via dell'Università 25. Reggio Calabria

ELISA DEMETRA MALLEMACE

Silicon Carbide photonic integrated circuits: study of material physical properties and design, fabrication and characterization of innovative active devices

The Teaching Staff of the PhD course in
INFORMATION ENGINEERING
consists of:

Antonella MOLINARO (Coordinator)
Giuseppe ARANITI
Francesco BUCCAFURRI
Claudia CAMPOLO
Riccardo CAROTENUTO
Giuseppe COPPOLA
Mariantonia COTRONEI
Lorenzo CROCCO
Dominique DALLET
Claudio DE CAPUA
Francesco DELLA CORTE
Giuliana FAGGIO
Gioia FAILLA
Fabio FILIANOTI
Patrizia FRONTERA
Sofia GIUFFRÈ
Giorgio GRADITI
Voicu GROZA
Tommaso ISERNIA
Gianluca LAX
Aimè LAY EKUAKILLE
Gaetano LICITRA
Elena Simona LOHAN
Pietro MANZONI
Francesco Carlo MORABITO
Andrea Francesco MORABITO
Giacomo MORABITO
Rosario MORELLO
Gabriel-Miro MUNTEAN
Giuseppe MUSOLINO
Fortunato PEZZIMENTI
Filippo Gianmaria PRATICÒ
Sandro RAO
Maria ROMANO
Domenico ROSACI
Giuseppe RUGGERI
Mariateresa RUSSO
Alexey VINEL
Antonino VITETTA
Maria Gabriella XIBILIA

Abstract

Silicon Carbide (SiC) has gained increasing attention as a promising platform for advanced photonic applications, due to its excellent physical properties, which include a wide bandgap, high thermal conductivity, and large refractive index. This thesis focuses on an exploration of the potential of SiC in photonic applications through the characterization of its optical properties and the design, fabrication, and characterization of optical devices, such as photosensors and optical modulators.

For a proper design of the optical devices, an in-depth understanding of the material's optical properties is essential. For this reason, after the study of the refractive index of 4H-SiC, 3C-SiC, and GaN via spectroscopic ellipsometry, the thermo-optic coefficient is experimentally evaluated for 4H-SiC and GaN, from room temperature to ≈500 K, at near-infrared (λ=1550 nm) and visible (λ=632 nm) range.

In this thesis, the optical response of 4H-SiC-based photosensors is demostrated. Specifically, an optically controlled power MOSFET, which comprises real-time optical junction temperature monitoring and its optical driving, is theoretically studied. In addition, an ultraviolet *p-i-n* photodetector is demonstrated with a responsivity of 0.168 A/W (quantum efficiency of 72.7%) at zero bias, which is the best value if compared to those found in the literature. Then, an *ad-hoc* numerical model is developed for comprehensive physical characterization.

To enable detection in the visible and near-infrared range, where 4H-SiC exhibits transparency, alternative device structures need to be explored. For this purpose, the fabrication and characterization of a Schottky photodetector based on graphene/4H-SiC is demonstrated. The internal responsivity at zero bias is 3.275 mA/W at λ=406 nm, 0.268 mA/W at λ=633 nm, and 56.73 μA/W at λ=785 nm.

Furthermore, the research involves an amorphous-SiC (a-SiC) thermo-optic modulator (TOM) on a SiC-on-Insulator (SiCOI) platform. Integrated with a Titanium microheater, the TOM demonstrates a noteworthy modulation depth of 96%, with the rise and fall time of 16 μs and 13 μs, respectively. Additionally, a successful demonstration of a single-mode, polarization-independent waveguide based on a 3C-SiC p-i-n structure epitaxially grown on an SOI wafer concludes the study.

This comprehensive exploration contributes valuable insights into the potential of SiC for advanced photonic applications, paving the way for further advancements in this field.

Contents

List of Figures

List of Tables

1

Introduction

The first chapter of this thesis is dedicated to introducing the field of integrated photonics. It begins by discussing the advantages of photonics in comparison to traditional electronics, with a specific focus on Silicon (Si) as the predominant material. The chapter explores the primary application areas where silicon photonics has a significant impact, highlighting its key benefits. Although the impressive success of silicon photonics, recent years have also revealed certain limitations, leading to the exploration of alternative platforms.

1.1 Silicon photonics

Silicon Photonics is the science and technology that involves the generation, transmission, detection, and/or manipulation of light employing silicon (Si) as a primary material [1, 2]. The continuously growing demand for data traffic in recent years has driven the development of technologies that can meet stringent requirements of bandwidth, energy consumption, cost, and scalability.

Silicon photonics has attracted great interest due to its capacity to enhance data transfer both between and within chips while exhibiting significantly lower power consumption and reduced heat generation compared to traditional all-electronic circuits [3]. Indeed, electrical interconnects encounter inherent limitations, including signal loss, dispersion, crosstalk, and limited speed, which become increasingly pronounced as demands for higher interconnect bandwidth over longer distances rise [4]. To address these challenges, optical technologies have emerged as a faster and low-power solution.

Integrated photonics has emerged as one of the most extensive areas of research in photonics. Similar to how integrated electronics revolutionized the electronics industry, integrated photonics aims to miniaturize photonic lightwave circuits. The concept of a photonic integrated circuit (PIC) was first proposed by Soref and Benett [5]. PIC envisions the integration of facilities for light emission, modulation, switching, amplification, and detection on a single chip.

In this context, the silicon-on-insulator (SOI) platform has gained prominence for its quality and utility in silicon photonics development. This platform comprises three distinct layers, with silicon dioxide (SiO_2) sandwiched between two silicon layers. The upper silicon layer is used to create waveguides, enabling the implementation of high-index-contrast waveguides using silicon dioxide cladding.

While the development of individual components progresses, the monolithic integration of all functions in the same chip remains a challenge [6]. The silicon photonics platform has seen the development of various optical components, including waveguides [7], couplers [8], splitters, modulators [6, 9], and photodetectors[10, 11]. Moreover, the success and continued research in silicon photonics have opened doors to exploration in various fields not only telecommunications, including signal processing, sensing, quantum computing, and more. Optical sensors, in particular, offer numerous advantages when compared to traditional electronic sensors. These advantages include immunity to electromagnetic interference, compact form factors, high multiplexing capabilities, durability in challenging environmental conditions, and passive operation at the sensing locations.

Over the past two decades, research and development in silicon photonics have witnessed a substantial acceleration. This growth is primarily due to its compatibility with established silicon manufacturing processes, positioning silicon photonics as an attractive and viable solution for advancing next-generation communication networks, data centers, and high-performance computing infrastructures. One of the most significant advantages of the SOI platform in photonics is its ability to leverage the mature complementary metal-oxide semiconductor (CMOS) fabrication infrastructure originally designed for electronic integrated circuits (ICs). This alignment facilitates cost-effective, high-volume, and high-yield manufacturing.

According to Yole Intelligence, the forecasted market for Silicon photonics-based die, categorized by distinct applications, is expanding exponentially in the coming years. This growth is anticipated to result in a compound annual growth rate (CAGR) of 36% from 2021 to 2027 [12].

Although photonic integrated circuits based on silicon offer substantial advantages, they face noteworthy challenges. The primary focus of Si-integrated platforms is predominantly centered on the infrared region of the electromagnetic spectrum. It is attributed to the narrow bandgap of Si, which is about 1.2 eV. It leads to the absorption of photons with a wavelength lower than 1 μm. This poses a significant challenge when working with wavelengths that fall outside the transparency window for visible light photonics, a domain with diverse applications including next-generation data center interconnects, atomic and quantum sensors, as well as quantum networks and computation. Furthermore, due to the high intensities re-

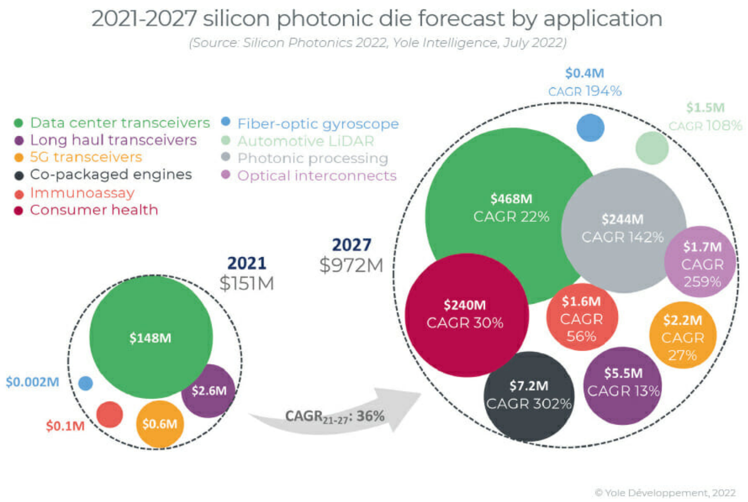

Fig. 1.1: Silicon photonics die forecast by application from Yole Intelligence [12], dated to July 2022.

quired for nonlinear frequency conversion, nonlinear losses can arise within the material, e.g., two-photon absorption (TPA), when pumped in the near-infrared (below a wavelength of 2.2 µm). TPA, attributed to its narrow bandgap, occurs when the energy of two photons is sufficient to be absorbed, exciting an electron. Furthermore, due to its centrosymmetric structure, Silicon doesn't exhibit the Pockels effect, an optical phenomenon characterized by a linear variation of the refractive index in response to an applied electrical field. This effect is pivotal for encoding high-frequency signals onto light, a requisite feature in applications such as telecommunications, optical signal processing, and optical computing. The physical properties of Si such as its poor thermal conductivity and its low breakdown electric field limit its application in harsh conditions as has been demonstrated in electric fields. It is accomplished by a large thermo-optic coefficient of about $10^4 K^{-1}$ [13] limits its application in high-temperature conditions.

For these reasons, there is growing interest in exploring other novel optical materials for use in integrated photonics with the aim of overcoming the limitations of silicon. One of the most recent novel materials is Silicon Carbide (SiC).

Nowadays, SiC is considered one of the most representative third-generation semiconductors. Thanks to its excellent properties, SiC is replacing Si in a lot of applications. The escalating demand is due to address the wide array of requirements, including high-temperature levels, high-voltage tolerance, and low-power consumption. Specifically, SiC has become the best material choice for advanced power devices and sensing applications, therefore its market has increased considerably [14].

As shown in Fig. 1.2, according to the newly released 2023 edition of Yole Intelligence's Power SiC Report, the Silicon Carbide device market is estimated to reach 9$ billion by 2028, with a growing CAGR of 31% from 2022 to 2028 [12]. Here is clearly shown that automotive applications, which represent 70% of the power SiC market in 2022, dominate the SiC market alongside a variety of industrial applications, including transportation, energy, and telecommunications [12].

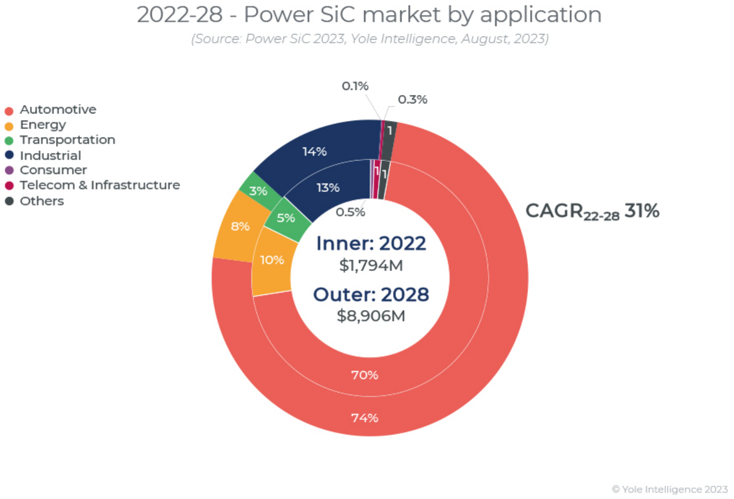

2022-28 - Power SiC market by application

(Source: Power SiC 2023, Yole Intelligence, August, 2023)

Fig. 1.2: Silicon Carbide market forecast to 2028, from Yole Intelligence's Power SiC Report [12], dated to August 2023.

Moreover, SiC boasts several advantages as a photonic platform, including a wide bandgap, a broad transparent window, and a substantial second-order (χ^2) susceptibility of 34 pm/V [15] and significant third-order non-linearity (χ^3) [16, 17]. These favorable properties, among others, render SiC an exceptionally promising candidate for photonics applications, wherein it has the potential to complement the leading silicon-based material platforms. Consequently, this thesis undertakes an extensive exploration of SiC's potential in the field of photonics.

1.2 Outline of this thesis

The main aim of this research activity is to explore the potential of the Silicon Carbide in the field of photonics. For this purpose, the initial phase of the study involves a comprehensive optical characterization of this material. Subsequently, the thesis deals with the design, fabrication, and characterization of active components including photosensors operating in ultraviolet, visible, and near-infrared spectra, as well as optical modulators based on Silicon Carbide-on-Insulator (SOI) platforms. This thesis is structured into six chapters and the content of each is defined as follows.

Chapter 2 introduces the theoretical background of integrated photonics. The study emphasizes the utilization of novel materials in this domain as promising candidates for the next generation of devices, specifically highlighting wide bandgap materials such as Silicon Carbide (SiC), Gallium Nitride (GaN), and Graphene. Although an overview of the three platforms is given, the main material used in this thesis is SiC. The chapter provides an outline of the main optical devices employed in this thesis, their operating principles, and the relative key figures of merit. Additionally, it provides a review of the relevant studies about the active devices based on SiC reported in literature and then it discusses the main aspect of the employed simulation tools.

Chapter 3 is dedicated to the characterization of the optical properties, primarily refractive indices, for wide bandgap semiconductor materials, including 4H-SiC, 3C-SiC, and GaN. The experimental measurements are derived from spectroscopic ellipsometry across a broad spectral range, spanning from ultraviolet to near-infrared. Furthermore, the temperature dependence of the thermo-optic coefficient, which quantifies refractive index variations with temperature, is investigated for 4H-SiC and GaN over a wide temperature range. Experimental measurements are conducted at two distinct wavelengths, one in the visible ($\lambda = 632nm$) and the other in the near-infrared ($\lambda = 1550nm$) range.

Chapter 4 focuses on the examination of the optical responses of photosensors based on 4H-SiC. It begins by presenting numerical results pertaining to an all-optical-controlled power MOSFET, wherein real-time optical junction temperature monitoring is accomplished with its optical driving. The chapter proceeds with a discussion of experimental and numerical results related to a high-performance p-i-n photodiode operating in the ultraviolet range. It concludes with a study on a Schottky photodetector based on graphene/4H-SiC, detailing its fabrication and electro-optic characterization in both the visible and near-infrared ranges.

Chapter 5 investigates the potential of the SiC-based modulators integrated on Silicon Carbide-on-Insulator (SiCOI) platforms. Firstly, it discusses the design, fabrication, and experimental characterization of a modulator based on Silicon Carbide-on-Insulator (SiCOI) platforms, which is a thermo-optic modulator based on amorphous-SiC (a-SiC). Then, the prospects of a waveguide based on 3C-SiC p-i-n structure epitaxially grown on an SOI wafer are investigated. Here, an optical waveguide single-mode and polarization-independent is demonstrated.

The final chapter (**Chapter 6**) concludes the thesis, summarising the main results and presenting the idea for future works.

2

Wide bandgap semiconductor integrated photonics: theoretical background, and associated materials and devices

This chapter introduces the theoretical background of integrated photonics, with a specific focus on wide bandgap semiconductor materials. First, it provides an overview of the structure and key physical properties of silicon carbide (SiC), highlighting its potential in the field of photonics. Subsequently, the chapter delves into the theory of light propagation within materials, leading to a more in-depth exploration of passive and active photonic components. Here, the essential working principle and the figures of merit (FOM) are reported. The discussion then shifts again towards SiC, featuring a comprehensive literature review on photonic devices fabricated using this material. Finally, the chapter concludes with an overview of simulation tools useful in the design of the devices discussed throughout this thesis.

2.1 Silicon Carbide as a new platform for photonics

In the exploration of novel platforms suitable for photonics applications, Silicon Carbide has gained significant attention due to its excellent properties. A comprehensive knowledge of the material's physical properties is essential for the proper design and fabrication of optical devices based on it. Consequently, this section will provide insight into the crystallographic structure and physical properties of SiC. Through a direct comparison of the fundamental electrical properties, this section delves into the advantages that SiC offers over Si.

2.1.1 SiC crystal structure and polytypes

Silicon Carbide (SiC) is a compound semiconductor characterized by a well-defined stoichiometry, in which silicon and carbon atoms, both IV group elements, are in a 1:1 ratio [18]. These atoms are tetrahedrally bonded through covalent bonds. The elemental cell of SiC consists of a tetrahedron in which a single carbon atom is surrounded by four Si atoms, connected through sp^3 bonds, as visually depicted in Fig. 2.1a.

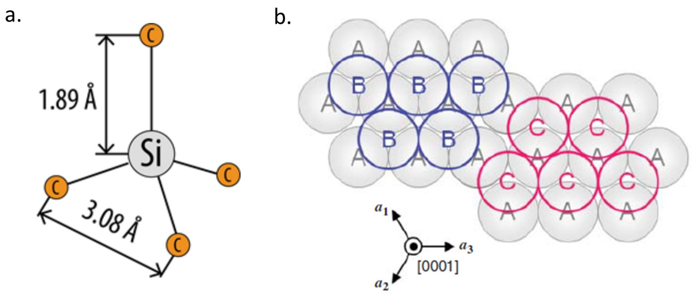

Fig. 2.1: SiC tetrahedral cell (a), and occupation sites (A, B, and C) in the hexagonal close-packed system (b) [18].

SiC exhibits a variety of crystal structures depending on the stacking sequence along the crystallographic axis direction. Specifically, the crystalline structure of SiC can be described as a hexagonal closed-packed stacking of double layers consisting of Si and C atoms. As illustrated in Fig.2.1b, each SiC bilayer falls into one of three stacking sequences: A, B or C. These distinct sequences give rise to variations in crystal structure, known as *polytypes*. To date, over 200 different SiC polytypes have been identified, each possessing unique optical, electrical, and mechanical properties.

Typically, to distinguish between polytypes, Ramsdell's notation is commonly employed. Each polytype is denoted by a number that indicates the quantity of Si-C bilayers in the unit cell, along with a letter that represents the lattice symmetry: cubic (C), hexagonal (H), or rhombohedral (R). So far, the main SiC polytypes are 3C-SiC, 4H-SiC and 6H-SiC. Their schematic structures are shown in Fig. 2.2.

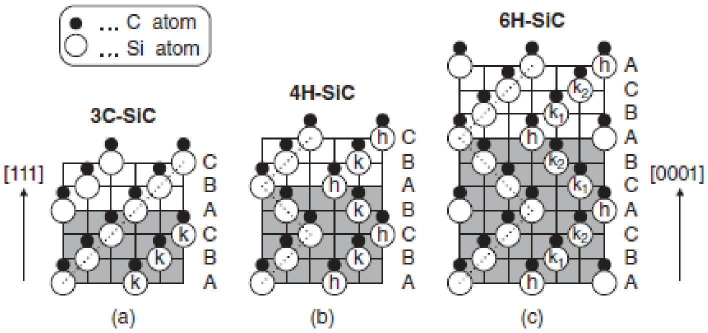

Fig. 2.2: Schematic structure of main SiC polytypes: 3C-SiC (a), 4H-SiC (b) and 6H-SiC (c) [18].

2.1.2 Physical properties

SiC has attracted considerable attention thanks to its excellent properties. Firstly, the robust binding energy of 4.6 eV between silicon and carbon atoms gives this material extraordinary hardness and chemical inertness [19]. Additionally, the strong covalent bonds lead to a wide bandgap of SiC with values ranging from 2.3 eV (3C-SiC) to 3.2 eV (4H-SiC). Table 2.1 provides a concise overview of the key physical properties of SiC polytypes in comparison to Si, the most commonly used semiconductor material in electronics and optics [20].

A direct comparison reveals that SiC possesses a critical electric field strength approximately five times higher than that of Si. Furthermore, its remarkable thermal conductivity and electron saturation speed make SiC exceptionally well-suited for high-temperature, high-voltage, and high-power applications. In detail, the high thermal conductivity of SiC enables efficient heat dissipation, this reduces the necessity for large and costly cooling systems, which sets it apart from other semiconductors like Si. Undoubtedly, this presents a significant advantage in terms of cost, size, and weight of the system. Moreover, another property that impacts the performance at higher temperatures is the intrinsic carrier concentration. SiC exhibits a much lower intrinsic carrier concentration (approximately 17 orders of magnitude lower in 4H-SiC) compared to Si. As temperature increases, material properties undergo alterations, including a reduction in the energy bandgap and an increase in carrier concentration, both of which impact device performance. SiC is characterized by a high saturation speed, which makes it suitable for high-speed applications [21]. Moreover, its exceptional breakdown electric field, at least one order of magnitude greater than Si, permits utilization in high-voltage and high-power conditions.

Nonetheless, while the majority of electronic properties of SiC have been extensively investigated, there is limited knowledge regarding its properties and advantages as a photonic material. The main optical properties of SiC are summarized in Table 2.2. Firstly, due to its wide bandgap, SiC is transparent in the visible and near-infrared range. Consequently, from the point of view of photodetection, the wide bandgap provides intrinsic visible blindness. This semiconductor is particularly suitable for ultraviolet (UV) photodetection, with a photoresponse peak spanning from 200 nm to 300 nm, depending on polytypes and device structure. SiC-based photodetectors are characterized by low leakage currents, under high reverse bias conditions, ensuring minimal noise. Moreover, SiC's robust chemical bonds contribute to its high radiation hardness. Therefore, this kind of photodetector suffers less from device aging due to radiation. It makes this semiconductor the best choice for UV detection in hostile environments [22].

Property	**Si**	**3C-SiC**	**4H-SiC**	**6H-SiC**
Bandgap(eV)	1.1	2.3	3.2	3
Relative dielectric costant	11.9	9.7	9.7	9.7
Breakdown field at $N_D = 10^7 cm^{-3}$ **(MV/cm)**	0.6	<1.5	3	3.2
Thermal conductivity $(Wcm^{-1}K^{-1})$	1.5	3-5	3-5	3-5
Electron mobility at $N_D = 10^6 cm^{-3}$ $(cm^2V^{-1}S^{-1})$	1200	750	800	60-400
Hole mobility at $N_D = 10^6 cm^{-3}$ $(cm^2V^{-1}S^{-1})$	420	40	115	90
Saturated electron drift velocity $(10^7 cms^{-1})$	1	2.5	2	2
Intrinsic carrier concentration (cm^{-3})	$1.0{\cdot}10^{10}$	$1.5{\cdot}10^{-1}$	$5{\cdot}10^{-9}$	$1.6{\cdot}10^{-6}$

Table 2.1: Main physical properties of SiC polytypes compared with Si.

In addition to its broad transparent window, SiC is also suitable for light guiding across the visible and near-infrared spectrum, as well as for longer wavelengths. It shows a high refractive index of about 2.73 at the wavelength of telecommunication interest around 1550 nm. Furthermore, being a non-centrosymmetric crystal, silicon carbide exhibits the Pockels effect, enabling rapid and linear variations in the refractive index proportional to an applied electric field. The Pockels effect holds the potential for achieving high data rates and microwave-conversion efficiencies. Finally, SiC has a strong second-[23] and third-order[24] nonlinearities, further expanding its photonic applications.

Property	Si	SiC
Refractive index at 1550 nm	3.5	2.5-2.7
Second-order non linearities, χ^2 (pm/V)	-	34 [15]
Electro-optic effect (pm/V)	Carrier plasma effect [25]	$r_{33} = 1.8$, Pockels effect [26]
Third-order non linearities, at 1.55 μm χ^3 $(\times 10^{-7} cm^2 W^{-1})$	450	60-80 [24]

Table 2.2: Main optical properties of SiC compared with Si.

2.2 An emerging semiconductor for photonics: Gallium Nitride

Gallium Nitride (GaN), a III–V semiconductor compound formed from gallium and nitrogen, exhibits a crystalline structure shown in Fig. 2.3, where each gallium atom is tetrahedrally bonded to four nitrogen atoms. GaN is a wide bandgap semiconductor and, as SiC, is one of the most representative third-generation semiconductors. It has drawn extensive attention in power electronics due to its exceptional electrical properties [27]. These properties encompass a wide bandgap of approximately 3.4 eV, an electron mobility of around ≈2000 cm^2/Vs, a saturated electron velocity of $2.5 \cdot 10^5 m/s$, high thermal conductivity of 253 W/mK, and a robust breakdown electric field of 5 MV/cm.

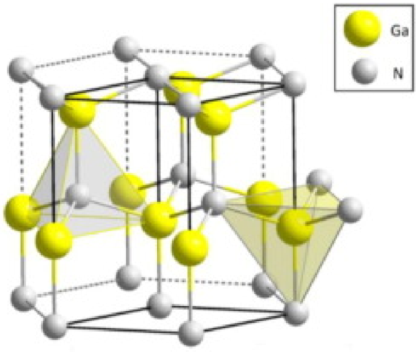

Fig. 2.3: Structure of Gallium Nitride (GaN) [28].

GaN has recently emerged as a viable candidate for photonics applications. Its superior properties (above described) with the high optical absorption coefficient and the lower sensitivity of GaN to ionization radiation effect make it an excellent candidate for light detention across various domains. Its applications range from civil and military industries, where it is used to detect missile plumes, flame sensors, engine control, solar UV monitoring, source calibration, UV astronomy, and secure space-to-space communications [29–31].

As GaN is a direct bandgap semiconductor, it has particular significance in the development of light-emitting diodes (LEDs) [32]. Recent research efforts have yielded substantial progress in the creation of green and blue LEDs [33, 34] which are essential for energy-efficient lighting and displays, data storage, and communications.

Regarding integrated nonlinear optics, GaN-based technology remains in a nascent stage [35]. Optical devices based on this material suffer from high losses due to poor growth quality and process technology when compared to other materials. However, promising avenues are emerging for further exploration in this domain. Notably, some research has demonstrated relatively high second-order nonlinearities, with a χ^2 coefficient of approximately 16 pm/V [36].

2.3 Graphene

Graphene is a carbon allotrope characterized by a single-atom-thick planar sheet of sp^2-bonded atoms. Each carbon atom forms a strong covalent σ bond with its three nearest neighbor carbon atoms, maintaining a fixed inter-atomic distance of 1.42 A. Furthermore, each carbon atom establishes an π-bond oriented out of the plane. This distinctive atomic structure gives rise to graphene's two-dimensional (2D) hexagonal honeycomb lattice [37], as shown in Fig 2.4.

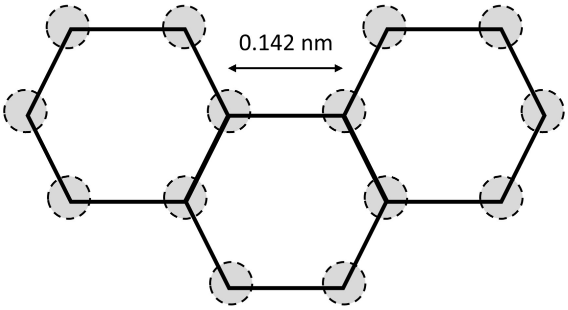

Fig. 2.4: Atomic structure of graphene.

Thanks to its outstanding electrical and optical properties, graphene has attracted considerable attention as a promising candidate for next-generation electronic and optoelectronics applications.

2.3.1 Physical properties

Graphene is a zero bandgap semimetal in which, as previously described, each carbon atom engages in three σ bonds and an out-of-plane π bond. This π state gives rise to two energy bands, namely the valence and conduction bands. These bands are cone-shaped and come in contact, without overlapping, at six points in the reciprocal lattice, which are commonly referred to as the K points, coinciding with the boundaries of the first Brillouin zone. The valence and conduction bands of graphene meet at the Dirac point, and the energy gap of undoped graphene is zero. The valence and conduction bands, π and π^*-bands, are symmetrical to each other and both satisfy a linear dispersion relation, known as Dirac's equation, expressed as:

$$E = \hbar v_F k \tag{2.1}$$

where $\hbar$ is the reduced Planck's constant, $v_F \approx 10^6 m/s$ is the Fermi velocity of graphene and k is the wave vector of the electron.

Thanks to its unique band structure, graphene exhibits an exceptionally high charge carrier mobility. Indeed, in suspended graphene at room temperature, the mobility can reach $\approx 2 \cdot 10^5 cm^2 V^{-1} s^{-1}$ [38]. The high mobility, 140 greater than that of Si, can be attributed to the sp2 hybridization that donates an extra electron to the π bond. These π electrons are delocalized at room temperature, resulting in high conductivity [39]. It should be noted that the Fermi level of graphene can be significantly stunned by applying external stimuli, owing to its two-dimensional nature and low density of states. Owing to the strong covalent bonds, graphene has an extraordinary mechanical strength [40, 41]

The thermal conductivity of graphene at room temperature is among the highest of any known material, about 2000-4000 $Wm^{-1}K^{-1}$ [42] for freely suspended samples. Due to its high thermal conductivity, graphene is considered an excellent candidate for thermal management applications.

Concerning the interaction between light and matter in graphene, the optical conductivity of graphene depends on the incident photon energy as well as temperature, carrier scattering rate, and the Fermi level. It should be decomposed into two contributions: intraband and interband carrier excitations.

The band structure of monolayer graphene, characterized by its absence of a band gap and the linear dispersion of Dirac electrons, gives graphene excellent optical properties. Indeed, when integrated into appropriately engineered materials, this enables ultra-broadband absorption spanning from the extreme ultraviolet (EUV) to the terahertz (THz) region [47, 77]. The absorption of the incident light at normal incidence is about $\approx 2.3\%$ in a wide wavelength range [43].

2.4 Propagation of light in matter

In 1849, Maxwell demonstrated that light exhibited the characteristics of an electromagnetic wave, aligning with the electromagnetic theory. The propagation of an electromagnetic wave, and so the propagation of light, within a medium can be derived from Maxwell's well-known equations:

$$\nabla \cdot \vec{E} = \frac{\rho}{\epsilon_0} \tag{2.2}$$

$$\nabla \times \vec{E} = -\frac{\partial \vec{B}}{\partial t} \tag{2.3}$$

$$\nabla \cdot \vec{B} = 0 \tag{2.4}$$

$$\nabla \times \vec{B} = \mu_0 \left(\epsilon_0 \frac{\partial \vec{E}}{\partial t} + \vec{J} \right) \tag{2.5}$$

where E is the electric field vector, B is the magnetic induction vector, J is the current density vector, ρ is the charge density, and ϵ_0 and μ_0 are the permittivity and permeability in free space, respectively. To explain how light propagates in matter, two additional vectors are introduced. These vectors are the displacement vector (D) and the magnetic field intensity (H), defined as:

$$\vec{D} = \epsilon_0 \epsilon_r \vec{E} \tag{2.6}$$

$$\vec{B} = \mu_0 \mu_r \vec{H} \tag{2.7}$$

where ϵ_r and μ_r are the relative dielectric permittivity and the relative magnetic permeability of matter in which light propagates.

By assuming an isotropic and homogeneous medium without external currents, the electric and magnetic fields are given by:

$$\nabla^2 \vec{E} = \frac{1}{c^2} \frac{\partial^2 \vec{E}}{\partial t^2} \tag{2.8}$$

$$\nabla^2 \vec{H} = \frac{1}{c^2} \frac{\partial^2 \vec{H}}{\partial t^2} \tag{2.9}$$

The solutions are:

$$\vec{E}(\vec{r}, t) = \vec{E_0} e^{i(\vec{k}\vec{r} - \omega t + \delta)} \tag{2.10}$$

$$\vec{H}(\vec{r}, t) = \vec{H_0} e^{i(\vec{k}\vec{r} - \omega t + \delta)} \tag{2.11}$$

where, $\vec{k}$ is the wave vector, ω is the angular frequency, δ is the initial phase.

The electromagnetic waves are described as *transverse waves* wherein the electric field (E) and magnetic field (H) vectors are perpendicular to the direction of wave propagation. In simpler terms, these vectors oscillate in planes that are both perpendicular to each other and to the direction of wave propagation. Consequently, these waves are referred to as ***transverse electromagnetic waves*** (***TEM***).

The way in which the field of an electromagnetic wave behaves in relation to space and time is defined as *polarization*. It is defined by the orientation and phase of the electric field vector.

Assuming the electromagnetic wave is propagating along the z-direction, as illustrated in Fig. 2.5, it can be represented as a composite of two waves oscillating along the x- and y-directions. These orthogonal planes, denoted as p-polarized and s-polarized, are parallel and perpendicular to the incident plane, respectively. More specifically, p-polarized light has an electric field vector parallel to the plane of incidence and it is called ***TM*** (*transverse magnetic*) polarized light, whereas s-polarized light has the electric field vector perpendicular to the incident plane, it is known as ***TE*** (*transverse electric*) polarized light. To provide further clarity, in the case of *TM mode*, $H_z = 0$ and $H_x = E_y = 0$ and the only non-vanishing field components are E_x, H_y and E_z. On the other hand, for *TE mode*, $E_z = 0$ and $E_x = H_y = 0$ and the only non-vanishing field components are H_x, E_y and H_z. Regarding the phase shift and amplitude between the p-polarized and s-polarized planes, three distinct polarization states can be achieved. In Fig. 2.5 linear, circular, and elliptical polarizations are visually represented. The most general polarization state, known as elliptical, features arbitrary phase differences and amplitudes between the two waves. Circular polarization, on the other hand, involves a phase shift of π and equal amplitudes, while linear polarization occurs when the two waves are in phase and possess identical amplitudes.

The interaction of light with a material is described in Fig. 2.6. When light, or more in general an electromagnetic wave, impinges upon an interface between two distinct optical media, a part is reflected, while another part is transmitted. The reflected wave is associated with the incident wave through the reflection coefficients of both polarizations, known as Fresnel complex amplitude reflection coefficients. These are expressed as:

$$r_p = \frac{E_p^{ref}}{E_p^{inc}} = \frac{n_1 \cos\Theta_i - n_2 \cos\Theta_t}{n_1 \cos\Theta_i + n_2 \cos\Theta_t} \tag{2.12}$$

$$r_s = \frac{E_s^{ref}}{E_s^{inc}} = \frac{n_2 \cos\Theta_i - n_1 \cos\Theta_t}{n_2 \cos\Theta_i + n_1 \cos\Theta_t} \tag{2.13}$$

where n_1 and n_2 are the refractive index of two materials. The angle between the incidental ray and sample normal, Θ_i, and the reflected angle, Θ_r, are equal. Instead, light that enters into a material is refracted with an angle of Θ_t.

It should be noted that the relationship between the refractive indices n_1 and n_2, and the angles of incidence (Θ_i) and refraction (Θ_r) is governed by *Snell's law* defined as:

$$n_1 \sin\Theta_i = n_2 \sin\Theta_r \tag{2.14}$$

If n_1 is higher than n_2, there is an angle Θ_i for which Θ_r is 90°. This angle is called *critical angle* and it is $\Theta_c = arcsin\left(\frac{n_2}{n_1}\right)$. As long as the angle of incidence of the optical beam reaches the critical angle, the beam is completely reflected at the surface, no light is transmitted.

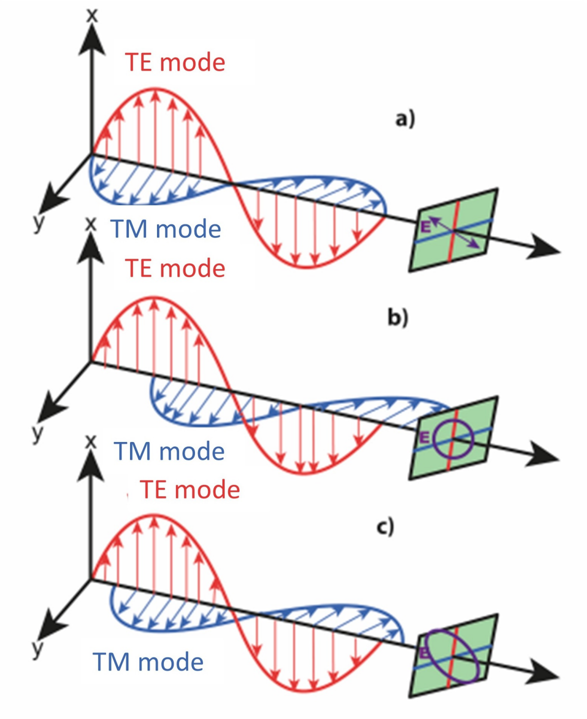

Fig. 2.5: Illustration of the propagation of the light in two components when the polarization is linear (a), circular (b), and elliptical (c).

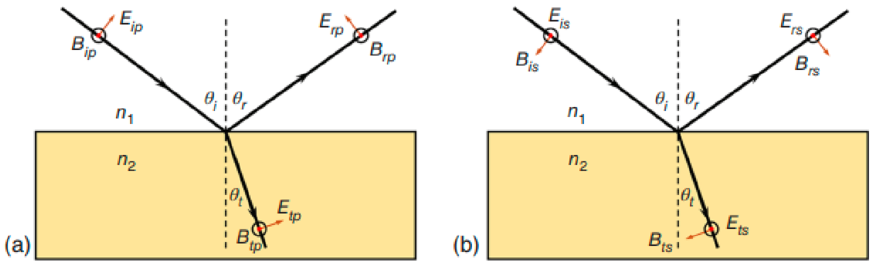

Fig. 2.6: Electric field for p-polarized (a) and s-polarized (b) plane [44]

2.5 Photonics devices: operating principle and figure of merit

Optical communication relies on the transmission of information via light signals, and it encompasses various optical devices for the manipulation and control of light. These devices can be broadly classified into two primary categories: *passive optical devices* and *active optical devices*. Each category serves a unique role in the operation of optical communication systems. Passive devices are employed to manage, control, and manipulate light without the need for an external energy source. Conversely, active photonic devices generate, amplify, or manipulate light signals through the utilization of external energy sources. The subsequent sections will describe the operating principles and key performance metrics of the principal passive and active photonic components.

2.5.1 Passive components

Some of the most popular passive photonic devices include waveguides, couplers, and cavities.

Waveguides

Optical waveguides are the basic elements designed to guide and control the propagation of light along a specific path minimizing losses. For this purpose, the optical waveguides exploit the effect of the *total internal reflection* (*TIR*). In order to understand this phenomenon, it is essential to further investigate how light propagates into a medium. Taking into account a light beam propagating through a medium (Fig. 2.7a) with a refractive index n_1 which impacts the interface with another medium with refractive index n_2, at an angle Θ_i from normal incidence, it is partially transmitted and reflected. As above described the relationship between the refractive indices n_1 and n_2, and the angles of incidence (Θ_i) and refraction (Θ_r) is governed by *Snell's law* 2.14. As shown in Fig. 2.7b, as long as the angle of incidence of the optical beam on the left wall reaches the critical angle, the beam is completely reflected at the surface, no light is transmitted, and the phenomenon of *total internal reflection* occurs. If another interface is considered below, where total internal reflection occurs once again, it is possible to define a waveguide. In this scenario, the light is confined to the area with a refractive index of n_1 and continues its propagation to the right.

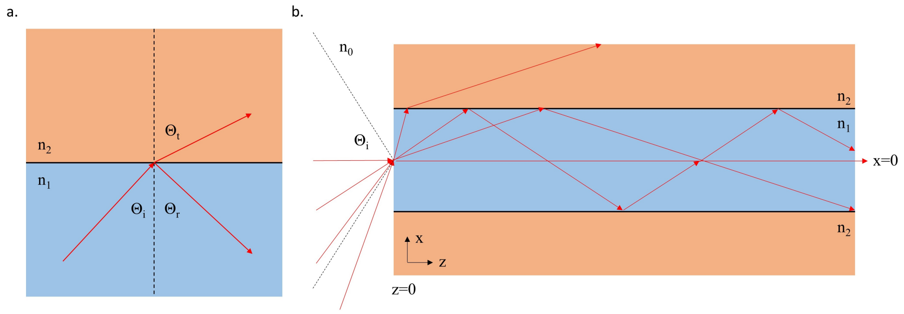

Fig. 2.7: A light beam incident on an interface between two media with different refractive index is partially reflected and transmitted (a), Total internal reflection of light beams propagated along a waveguide (b).

Then, in order to guarantee optimum light confinement, an optical waveguide is defined by a region with a high refractive index (n_2), called *core*, in which a light beam is injected, and it is surrounded by a lower refractive index (n_1), *cladding*. The main kinds of waveguides are shown in Fig. 2.8.

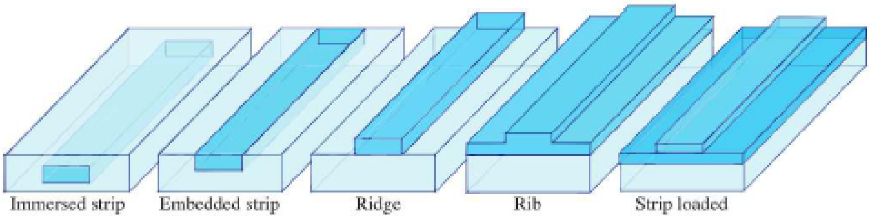

Fig. 2.8: Schematic cross-section of various optical waveguides.

An important parameter characterizing the propagation mode in a waveguide is the propagation constant. It is defined as:

$$\beta_m = k_0 n_{eff,m} \tag{2.15}$$

where, $n_2 < n_{eff,m} < n_1$ is the effective refractive index of the m-th mode propagated along the waveguide.

Couplers

Optical couplers are used to couple light to and from the waveguides. Two main solutions are usually adopted: *in-plane (butt) edge coupling* and *off-plane (vertical) grating coupling* [45–47]. In the first case, the light beam is coupled into or out of the waveguide through its lateral sides, ensuring continuous propagation within the same plane. In the grating couplers, instead, the light beam is launched on the top surface of the waveguide at a specific angle [48].

Grating couplers provide a flexible coupling in terms of arbitrary position on a chip, with a compact size, easy fabrication, and wafer-level testing capability. It is defined by a diffractive grating structure in which the waveguide refractive index profile is varied according to a periodic pattern (Fig. 2.9). This allows for phase-matching between the optical mode incident on the grating structure and the waveguides in the horizontal plane. The diffraction behavior for a grating coupler can be described using Bragg condition [8]:

$$\beta_m = k_0 \sin\Theta + m\frac{2\pi}{\Lambda} \tag{2.16}$$

It explains the relationship between the wave vector k_0 of the incident light and the propagation constant β of the corresponding light coupled into the waveguide. Moreover, Λ is the grating period, as illustrated in Fig. 2.9, Θ is the incident angle and m is the diffraction orders.

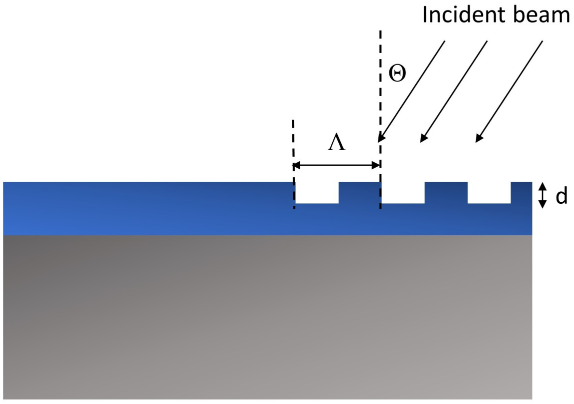

Fig. 2.9: Schematic structure of grating couplers.

Concerning ***edge coupling***, the light beam from an optical fiber is aligned to the waveguide horizontally. Nowadays, it is a standard to integrate a single inverse taper. It refers to a gradual widening of the waveguide along the direction of mode propagation. In this configuration, the narrow end of the taper is in proximity to the fiber, while the wider end is linked to photonic waveguides. It allows to increase the light confinement [49, 50]. A schematic of an inverse taper is shown in Fig. 2.10.

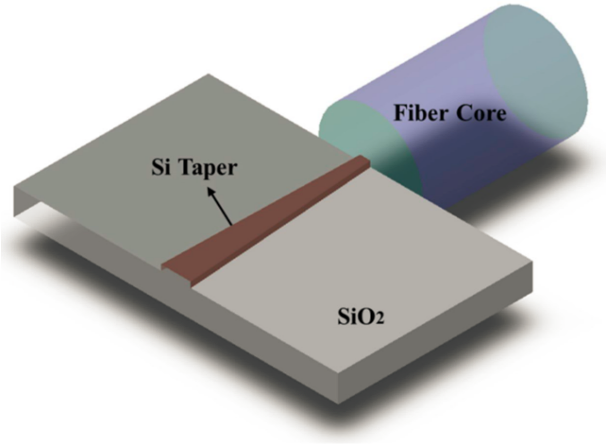

Fig. 2.10: Schematic structure of edge couplers [45].

Fabry-Perot cavity

A Fabry-Perot (FP) cavity is an optical device formed by two parallel mirrors partially reflected with high reflectivity. In the simplest way, both mirrors are constituted by two planes as illustrated in Fig. 2.11.

Fabry-Perot cavity exploits the **multiple-beam interference**. When light is incoming in the cavity through one semitransparent mirror, it undergoes multiple reflections between the mirrors, creating an interference pattern. The reflected rays

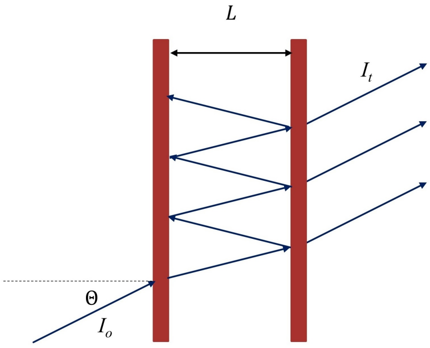

Fig. 2.11: Structure and schematically working principle of a Fabry-Perot cavity.

interfere with each other to produce sharp fringes in the transmitted field. Indeed, each time the light reflects off a mirror, it travels back and forth between the mirrors, creating an interference pattern. The multiple reflections result in a complex pattern of constructive and destructive interference. The interference pattern that forms within the cavity depends on the wavelength of the incident light, the angle at which the light enters, and the spacing between the mirrors. In Fig. 2.11 the working principle of a Fabry-Perot cavity is schematically illustrated. Here, the incident light at a wavelength λ and with an amplitude I_0 is injected into the first mirror with an angle Θ with the normal of its surface. Each time the optical beam reaches the second mirror it is partially transmitted. All such transmitted light rays interfere with each other to give rise to maxima or minima depending on the path difference between them. Let the refractive index and length of the cavity be n and L, respectively, the optical path difference between two consecutive rays is:

$$\Delta = nL\cos\Theta \tag{2.17}$$

and, when the optical beam is orthogonal to the surface, the difference phase is given by:

$$\Phi = \frac{2\pi\Delta}{\lambda} = \frac{2\pi nL}{\lambda} \tag{2.18}$$

Then, the transmitted signal I_t, as the result of multiple interferences taking place inside the FP cavity, is given by the Airy formula:

$$I_t = \frac{I_0}{1 + \frac{4F^2}{\pi^2}\sin^2\Phi} \tag{2.19}$$

where F=$\pi\sqrt{R}/(1-R)$ is the reflecting finesse of the interferometric cavity and R is the reflectance of the two mirrors.

2.5.2 Active components

This section delves into the working principles of three active components: photodetectors, ring resonators, and modulators.

Photodetectors

The photodetector converts an optical signal into an electrical one. More in general, the working principle is based on the *photoelectric effect*, in which the incident photons are absorbed by the semiconductor layer, leading to the generation of electron-hole pairs. There are different types of photodetectors based on device structure such as photoconductors, p-n junction photodiodes, p-i-n photodiodes, Schottky photodiode, Metal-Semiconductor-Metal (MSM) photodiodes. Among them, *p-i-n* and *Schottky photodetectors* have been widely studied and applied, so they will mainly be discussed in this thesis. Their working principle, all relevant terminology, and figures of merit are defined in the following.

p-n and p-i-n photodetector

The p-n photodiode represents one of the simplest kinds of semiconductor-based photodetector (Fig 2.12(a)). In this configuration, photons are absorbed within the depletion region at the interface between the heavily doped p- and n-type region when a reverse bias is applied. Briefly, photons, whose energy is higher than the semiconductor bandgap, are absorbed and an electron-hole pair is generated. These electron-hole pairs are then separated by the intrinsic or externally applied electric field within the space charge region contributing to electrical conduction [51]. In this way, a photocurrent is generated at contacts.

In contrast to p-n photodetectors, p-i-n photodetectors incorporate an intrinsic region between the heavily doped p- and n- regions (Fig. 2.12(b)). In this way, the depletion region is well-defined by the extension of the intrinsic region. The presence of this layer offers several advantages. It enhances response speed by reducing junction capacitance and, importantly, increases the absorption probability of incoming photons. This increase is significant because not all absorbed photons result in the generation of free electron-hole pairs that contribute to carrier transport. Some carriers may undergo recombination, and thus it is essential that the semiconductor layer responsible for the absorption process be larger than the penetration depth ($1/\alpha$, α is the absorption coefficient).

Schottky photodetector

Schottky photodetectors employ a metal-semiconductor junction to separate and collect the photogerated carriers. When a metal is brought in contact with a semiconductor, the Fermi levels of both materials tend to align at thermal equilibrium. This alignment establishes a potential barrier, known as the Schottky barrier Φ_B, which plays a pivotal role in electron transport across the interface. Significantly, the Schottky barrier is independent of the metal's work function and is determined

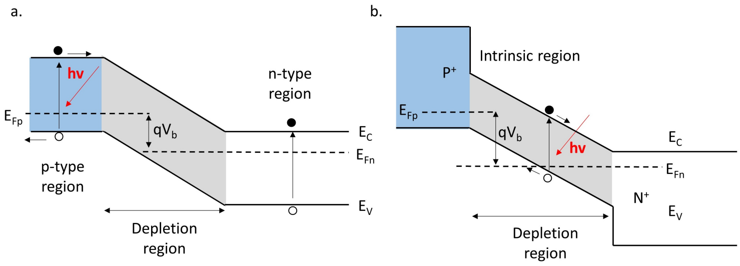

Fig. 2.12: Schematic energy diagram of a p-n photodiode (a) and p-i-n photodiode (b).

by the semiconductor's characteristics, including its doping level and surface properties, such as the density of surface states. The main mechanism of current transport in Schottky barriers is well-described by the thermionic theory. According to this theory, the electrical transport that occurs in a Schottky diode can be described as follows:

$$I = I_s\left(e^{\frac{q(V-R_sI)}{\eta k_B T}} - 1\right) \tag{2.20}$$

$$I_s = AA^*T^2 e^{-\frac{q\Phi_B}{k_B T}} \tag{2.21}$$

where A is the active area, A^* is the Richardson constant, q is the electron charge, k_B is the Boltzmann constant, T is temperature, V is the applied voltage, R_s is the series resistance, η is the ideality factor, and $\Phi_B = \Phi_{B0} + \Delta\Phi_B(V)$, Φ_{B0} is the Schottky barrier height (SBH) at zero voltage, and $\Delta\Phi_B(V)$ is the SBH change due to applied voltage.

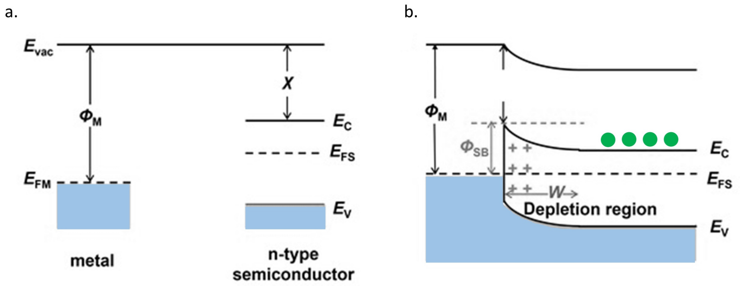

Fig. 2.13: Schematic energy diagram of a Schottky photodiode before (a) and after (b) contact.

It should be noted that the photodetection mechanism that occurs in a Schottky junction is the same as that previously described for p-n and p-i-n photodetectors. It enables the detection of photons with energy higher than the semiconductor's bandgap. Photons flux into a semi-transparent metallic layer and get absorbed within the semiconductor, generating electron-hole pairs within the depletion region of the semiconductor. Under enough built-in electric field, the photogenerated carriers are swept out, contributing to the photogenerated current.

Figure of merit

The key parameters used to evaluate the performance of a photodetector are introduced below. *Responsivity* describes how efficiently a photodetector converts incident light into an electrical signal, typically measured as a photocurrent. It is defined as the ratio between the photogenerated current and the incident optical power:

$$R = \frac{I_{ph}}{P_{inc}} \tag{2.22}$$

where I_{ph} is the photo generated current, P_{inc} is the incident optical power. Another important parameter is the external quantum efficiency (EQE) which quantifies the number of electron-hole pairs generated by each incident photon and is typically expressed as a fraction or percentage, representing the proportion of incident photons that contribute to the photocurrent. It can be defined as follows:

$$\eta_{ext} = \frac{I_{ph}/q}{P_{inc}/h\nu} = R\frac{hc}{q\lambda} = R\frac{E_{ph}}{\lambda} \tag{2.23}$$

where E_{ph} is the photon energy and λ is the wavelength of the optical beam.

Graphene/semiconductor Schottky junction: Internal photoemission effect

The **internal photoemission effect** (IPE) allows a sub-bandgap photodetection by exploiting the photon-assisted transmission of hot carriers across the Schottky junction. In this process, photons incident on the active area of the photodetector are absorbed by the metal, generating hot carriers within it. The photo-excited carriers with enough energy to overcome the Schottky barrier can be collected by the semiconductor, thereby contributing to the photocurrent. Consequently, the IPE enables the detection of photons with energy lower than the semiconductor bandgap but higher than the Schottky barrier ($\Phi_B < E_{ph} < E_g$). The main drawback of the IPE-based Schottky photodetectors is their limited efficiency. To address this limitation, IPE theory suggests thinning down the metal layer [52]. An intriguing approach to enhance efficiency involves replacing the metal with two-dimensional material such as **graphene** [53, 54].

Extensive investigations have been carried out on the theory of the graphene-semiconductor Schottky junction [55]. It has been empirically established that graphene forms a Schottky junction when interfaced with specific semiconductors such as Si, SiC, and GaN [56–58]. The physical principle of a Schottky junction based on graphene/semiconductor could be explained by the internal photoemission (IPE) theory. Here, the main relationship within the IPE theory concerning the graphene/semiconductor interface is reported.

The internal quantum efficiency of a Schottky photodetector based on graphene, which is defined as the number of carriers emitted to the semiconductor per absorbed photon, can be expressed as follows [59]:

$$\eta_{int} = P\frac{(h\nu)^2 - (q\phi_B)^2}{(h\nu)^3} \tag{2.24}$$

where $h\nu$ is the energy of the incident photon, ϕ_B is the Schottky barrier height and P is the emission probability. With regard to the internal responsivity, assuming A represents the optical absorption of the active material, by replacing the total incident power with the optical power absorbed by the metal layer ($P_{abs} = AP_{inc}$), the expression of the internal responsivity is:

$$R_{int} = \frac{I_{ph}}{P_{abs}} \tag{2.25}$$

where I_{ph} is the photogenerated current. According to the Eq. 2.24, the internal responsivity becomes:

$$R_{int} = \frac{I_{ph}}{P_{abs}} = \frac{q}{h\nu} \cdot \eta_{int} = P \cdot \frac{(h\nu)^2 - (q\phi_B)^2}{(h\nu)^3} \tag{2.26}$$

It's worth noting that in a Schottky junction based on graphene/semiconductor, the Fermi level of graphene is sensitive to the applied voltage across it. Without an applied bias, the Fermi level aligns with the Dirac point. When a forward bias is applied, a slight downshift of the Fermi level of graphene is shown. On the other hand, when a reverse bias is applied, the depletion region expands, resulting in an increase in charges within graphene [56]. This phenomenon is expressed by the following equations in which the SBH Φ_B is expressed as a function of reverse applied voltage (V_R). These expressions are distinctly defined for two different types of semiconductors: n-type and p-type, as outlined below:

$$q\Phi_B^n(V_R) = q\Phi_{SLG} - q\chi_{sm} - \Delta E_F(V_R) \tag{2.27}$$

$$q\Phi_B^p(V_R) = E_g - (q\Phi_{SLG} - q\chi_{sm} - \Delta E_F(V_R)) \tag{2.28}$$

where $q\Phi_{SLG}$ is the work function of graphene, χ_{sm} and E_g are the electron affinity and the bandgap energy of the semiconductor, respectively. $\Delta E_F(V_R) = E_F - E_F^0$ can be expressed as:

$$\Delta E_F = -sgn(n)\hbar v_F \sqrt{\pi|n|} \tag{2.29}$$

where $v_F = 1.1 \cdot 10^8 cm/s$, $\bar{h}$ is the reduced Planck constant. n is the carrier density in graphene, and it is defined by two contributions. The first is the extrinsic doping n_0

of graphene, the second is the charge induced by the application of a bias across the Schottky junction. It is expressed as follows [60]:

$$n = n_0 \mp \sqrt{\frac{2\epsilon_{sm}}{q} N \left(V_{bi} + V_r\right)} \tag{2.30}$$

where the signs minus and plus refer to an n- and p-type semiconductor, respectively. V_{bi} is the built-in potential, while ϵ_{sm} and N are the dielectric permittivity and the doping density of the semiconductor, respectively.

In this thesis, the fabrication and the electro-optic characterization of a Schottky photodetector based on Graphene/4H-SiC is reported.

Ring Resonators

The optical micro-ring resonator (MRR) is a basic building block for many applications [61–66]. Its function is to confine light within a circular waveguide, producing interference effects that result in specific resonances at specific wavelengths. Generally, the MRR is comprised of a looped optical waveguide and a coupling mechanism to enable access to the loop. Resonance along the cavity occurs when the waves completing one round-trip in the loop accumulate a phase shift equal to a multiple of 2π, which leads to constructive interference.

The fundamental structure of an MRR, as depicted in Fig. 2.14, consists of a ring waveguide coupled to a single bus waveguide for both input and output. In this configuration, E_{i1} and E_{o1} are the optical power entering into the ring cavity and the output optical power, respectively. Instead, E_{i2} is the incoming power in the ring, and E_{o2} is the power inside the ring cavity after one round trip.

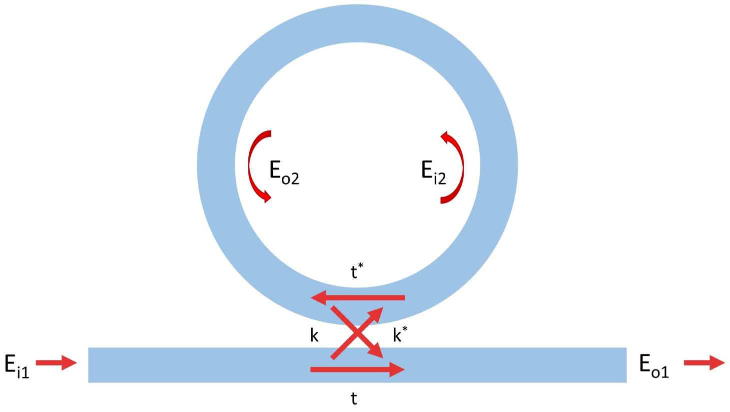

Fig. 2.14: Structure of an optical MRR in all pass filter configurations.

In the typical configuration where a single bus waveguide is connected to the ring cavity, the bidirectional power coupling between the waveguide and the cavity is often represented using matrix formalism. This coupling can be expressed as follows:

$$\begin{pmatrix} E_{o1} \\ E_{o2} \end{pmatrix} = \begin{pmatrix} t & k \\ k^* & t^* \end{pmatrix} \begin{pmatrix} E_{i1} \\ E_{i2} \end{pmatrix} \tag{2.31}$$

here, t is the transmission coefficient through the coupler and K is the coupling coefficient from the ring waveguide to the bus waveguide after one round trip. The $*$ denotes the conjugated complex value of t and k, respectively. In order to have a lossless coupling, the following expression must be satisfied:

$$|t|^2 + |k|^2 = 1 \tag{2.32}$$

The transfer function is expressed as:

$$T = \frac{E_{01}}{E_{i1}} = \frac{(t^*)^2 - 2t^* t \cos\Phi + t^2}{1 - 2t^* t \cos\Phi + (t^* t)^2} \tag{2.33}$$

where $\Phi = \beta L$ is the phase shift after a single round trip and $\beta = \frac{2\pi}{\lambda}$ is the propagation constant of the mode propagating along the cavity. Resonance within the ring occurs when the phase Φ is a multiple of 2π aligning the wavelength of light perfectly within an integer number of times along the optical length of the ring. The optical power confined within the cavity can be related to the optical attenuation coefficient α [1/cm] through the power transmission coefficient t^*, $(t^*)^2 = e^{-\alpha L}$, and L represents the entire physical circumference of the cavity, with $L = 2\pi r$.

A typical transmission spectrum obtained from a microring resonator is illustrated in Figure 2.15, in which its characteristic parameters are highlighted. These parameters can be directly extracted using the Eq. 2.33. First, the full width at half maximum (FWHM) of the resonance spectrum, which is the width of the resonance at half transmission power, is obtained as:

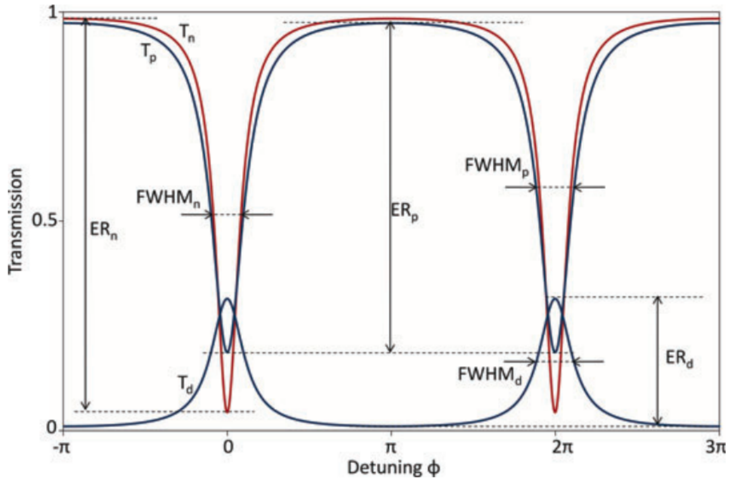

Fig. 2.15: Example of transmission spectrum of a ring resonator [63].

$$FWHM = \frac{(1-tt^*)\lambda_{res}^2}{\pi n_g L\sqrt{tt^*}} \tag{2.34}$$

The distance in terms of wavelength between two consecutive resonance peaks is the free spectral range (FSR) and it is expressed as:

$$FSR = \frac{\lambda^2}{n_g L} = \frac{2\pi c}{n_g L} \tag{2.35}$$

where λ is the wavelength, c is the speed of light in vacuum, and n_g is the group index of the propagating mode:

$$n_g = n_{eff} - \lambda\frac{dn_e}{d\lambda} \tag{2.36}$$

here, n_{eff} is the effective refractive index. Another parameter that can be directly calculated from the previously defined parameters is the finesse (F) of the ring resonator filter. It is defined as the ratio of the free spectral range (FSR) to the full width at half maximum (FWHM) of the resonance at a specific wavelength:

$$F = \frac{FSR}{FWHM} = \pi\frac{t}{1-t^2} \tag{2.37}$$

A distinction between *intrinsic* (Q_I) and *loaded* (Q_L) quality factor must be made. The intrinsic quality factor is determined when the ring resonator is not coupled to the waveguide, representing its inherent quality. When coupled to the bus waveguide, additional losses occur, affecting the loaded quality factor (Q_L). Q_L can be directly derived from the full width at half maximum (FWHM) as follows:

$$Q_L = \frac{\lambda_R}{FWHM} \tag{2.38}$$

where λ_R is the resonant wavelength. On the other hand, Q_I is expressed as function of Q_L:

$$Q_I = \frac{2Q_L}{1 \pm \sqrt{T}} \tag{2.39}$$

where T is the transmitted signal collected in the output of the MRR by waveguide at resonance wavelength.

The resonance of microring resonators can be tuned by altering the effective index of the waveguide. This tuning can be achieved through either electro-optic or thermo-optic effects, resulting in optical modulation within the device.

Modulators

An optical modulator is a device used to control or manipulate the characteristics of a light beam that propagates either in free space or in an optical waveguide. The variation of the light characteristics, such as its phase, amplitude, or polarization is achieved by altering the refractive index and the extinction coefficient of the optical modulator's material. These optical properties can be modified by applying external stimuli, including changes in temperature, electric field, and optical field. Depending on the specific property that changes during light modulation, optical modulators can be classified as either *refractive modulator* or *absorptive modulator* where changes in refractive index Δn or extinction coefficient Δk occur, respectively.

Micro-ring resonator (MRR) modulators, characterized by their compact device footprint and low energy consumption, present a trade-off with their inherently narrow optical bandwidth owing to their resonant behavior. In contrast, Mach-Zehnder interferometer (MZI) modulators provide high-speed operation and a broader optical bandwidth compared to MRR modulators. However, their drawbacks include increased power consumption and a larger physical footprint. In this section, the working principle of the thermo-optic modulator and electro-optic modulator is reported.

Regarding a *thermo-optic modulator*, it is generally composed of a waveguide and a resistive heater, which could be a heavily-doped semiconductor region or a metal, placed above (or near) and along the waveguide. When an electric current flows through the heater, it generates heat due to the Joule effect. This heat influences the surrounding area, which includes the waveguide, and this results in a temperature-induced change in the refractive index of the waveguide material. This alteration in refractive index, caused by the thermo-optical effect, impacts the phase of the light at the end of the waveguide. The relationship between the refractive index variation and temperature is expressed as follows:

$$n(T) = n_0(T_0) + \frac{dn}{dT}\Delta T \tag{2.40}$$

where, n_0 is the refractive at temperature T_0, dn/dT is the thermo-optic coefficient and ΔT is the variation of temperature. The amount of the light phase shift $\Delta\phi$ due to the temperature variation is:

$$\Delta\phi = \frac{2\pi L}{\lambda}\Delta n = \frac{2\pi L}{\lambda}\frac{dn}{dT}\Delta T \tag{2.41}$$

where λ is the wavelength and L is the length of the modulator.

In a **electro-optic modulator** changes in the optical properties of a waveguide are induced by the application of an external electric field. Commonly utilized electric field effects include the Pockels effect, the Kerr effect, and the Franz-Keldysh effect [67]. The Pockels effect, also known as the linear electro-optic effect, results in a linear change in optical properties concerning the externally applied electric field [68]. This effect is observed only in non-centrosymmetric crystalline materials, such as lithium niobate ($LiNbO_3$)[69], barium titanate ($BaTiO_3$) [70] and silicon carbide (SiC) [26]. The variation in refractive index of a material under the influence of electric field (E) can be expressed as:

$$n(E) = n_0 - \frac{1}{2} r n_0^3 E \tag{2.42}$$

where n_0 is the refractive index without electric field, and r is the Pockels coefficient.

The Kerr effect, also known as the quadratic electro-optic effect, introduces a nonlinear effect in the refractive index as a quadratic function of the applied electric field. The variation of the refractive index as a function of the applied electric field became:

$$n(E) = n_0 - \frac{1}{2} r n_0^3 E^2 \tag{2.43}$$

Finally, the Franz-Keldysh effect brings about alterations in the energy band edges of the material, which affect the electron energy as an electric field is applied. It results in changes in the crystal's absorption properties.

It's worth noting that silicon, being a centrosymmetric semiconductor, does not exhibit the Pockels effect, and both the Kerr and Franz-Keldysh effects are exceedingly small. Consequently, electro-optic modulation based on these effects is not permitted. To address this limitation, a solution was proposed by Soref and Bennett, which involves leveraging the plasma dispersion effect [25]. In this scenario, the concentration of charge carriers in the semiconductor is changed, allowing for a variation in its absorption coefficient and refractive index. This effect becomes the dominant method of modulation in silicon-based modulators.

2.6 Silicon Carbide photonic devices: Literature review

In this section, a literature review in integrated photonics based on SiC is reported, with a specific focus on photosensors and modulators.

2.6.1 Silicon Carbide photosensors

In recent years, SiC has been demonstrated to be a suitable semiconductor for ultraviolet detection. The ultraviolet (UV) spectrum range includes electromagnetic wavelengths shorter than those of visible light, spanning from 10 nm to 400 nm, corresponding to photon energies ranging from 3 eV to 124 eV. The detection of UV radiation allows a wide range of civil and military applications including optical communication [71], flame detection [72, 73], combustion monitoring [29], chemical analysis [74], astronomy [75].

Although the Si-based UV photodiode has been extensively investigated, this material shows a lot of limitations. Due to its narrow bandgap, Si-based photodetectors suffer from device aging which results from exposure to radiation with significantly higher energy levels than the semiconductor's bandgap. An additional limitation is their sensitivity to low-energy radiation, so the use of filters to eliminate visible and infrared photons is required. To overcome these limits, a wide bandgap semiconductor such as SiC, supported by its superior physical properties above described, is considered an intriguing choice.

Despite SiC is an indirect bandgap semiconductor that is characterized by a small optical absorption coefficient, SiC offers several advantages. SiC's strong bonding enhances device radiation hardness [76], making it less susceptible to radiation damage and increasing its longevity in high-energy radiation applications [22]. Additionally, the band gap of 4H-SiC lies at the upper edge of the visible range. It is naturally transparent to visible and infrared light. Then, SiC guarantees the development of UV photodetector without visible filters and provides outstanding long-term durability and reliability [77, 78], even when operated under high-intensity radiation (up to 1000 W/m^2) and high-temperature conditions [79, 80].

Over the past decade, high-performing UV photodetectors based on SiC have been more widely studied [81]. Extensive research effort on SiC-based UV photodetector is made due to their exceptional performance in the visible-blind UV range. Various device structures have been explored, including Schottky, p-i-n, avalanche, and metal-semiconductor-metal(MSM). The main results are summarized following. Although earlier research has explored photodiodes constructed from 6H-SiC [82, 83], 4H-SiC has gained interest in various application domains due to its enhanced electronic characteristics. 4H-SiC UV photodetectors typically exhibit a responsivity in the spectrum range of 220–380 nm, with peak responsivity occurring at approximately 290 nm [84]. Regarding the 4H-SiC-based Schottky photodiode, an experimental characterization of a device based on interdigit structure by Ni_2Si stripes [85] is reported. It shows a low peak responsivity at 280 nm of about 37mA/W at zero bias and an external quantum efficiency just above 10 %. Xu et al. [86] demonstrated a vertical Schottky photodetector based on 4H-SiC a semitransparent Ni contact. It reaches good thermal stability up to 200° C with a responsivity peak of 0.115 A/W at zero bias.

Schottky-based devices exhibit a higher sensitivity to visible light compared to a p–n junction [87] and show an increased dark current at higher temperatures. Consequently, their practical use may be confined to moderate temperature conditions. In contrast, *p-i-n* SiC photodiodes characterized by low-noise, high-speed responses, and high responsivity at low reverse bias, have shown great potential. Cheng et al. [88] report a p-i-n 4H-SiC photodiode with a peak spectral responsivity of 0.13 A/W at 270 nm wavelength at -5V, resulting in a maximum external quantum efficiency of 61%. In [89] the investigation of the spectral responsivity as a function of temperature up to 450K is reported. Here, at room temperature, the peak responsivity is

0.13 A/W at 266 nm, showing a slight rise to 0.15 A/W at 268 nm as the temperature reaches 450 K.

Avalanche photodiodes (APDs) based on 4H-SiC have also been explored, with one demonstrating an extremely low dark current [90]. At 280 nm, it achieved a maximum responsivity of 93 mA/W, corresponding to an external quantum efficiency of 41%. SiC detectors can serve as photon-counting detectors in applications requiring ultra-low-level UV detection, sometimes even at a single photon level. These detectors are well-suited for situations where a weak signal must be distinguished from a relatively low background, such as in bio-aerosol detection, lidar, communication, and low-light imaging [91, 92]. The first 4H-SiC single-photon counting avalanche photodiodes (SPAPD) were reported in previous studies, representing a significant advancement in the field [93, 94].

2.6.2 Silicon Carbide optical modulators

As mentioned in Section 2.5, in order to achieve excellent light confinement in optical waveguides it is necessary a significant refractive index contrast between the core and cladding materials. For this purpose, during the last two decades, various approaches have been proposed to create stable platforms with high refractive index contrast, wherein high refractive index silicon carbide (SiC) is enveloped by a low refractive index material. One intriguing proposed solution to address this issue involves the use of SiC thin film on an insulating substrate, commonly known as SiC-on-insulator (SiCOI). Similar to the principle of SOI, SiCOI provides a substantial refractive index contrast in the vertical direction.

SiCOI platforms

Initially, 3C-SiC has been considered the best choice due to its ease of epitaxial growth on Si substrate [95, 96]. This method leads to large-scale fabrication with high efficiency and low cost. Due to the high refractive index of Si a good light confinement was obtained by undercutting the below substrate. Despite several results reported in literature [17, 96, 97], these suspended devices faced challenges related to low yield and reliability, primarily due to their delicate mechanical structure, leading them unsuitable for the creation of large-scale integrated photonic devices. A promised alternative is the fabrication of a SiC-on-insulator (SiCOI) platform. Two distinct approaches for creating SiCOI platforms on 4H-SiC have been proposed, as illustrated in Fig. 2.16.

The first method is the ***smart/ion-cut method*** which has already been widely used for Silicon-on-Insulator (SOI) stacks by replacing Si with SiC. In the past

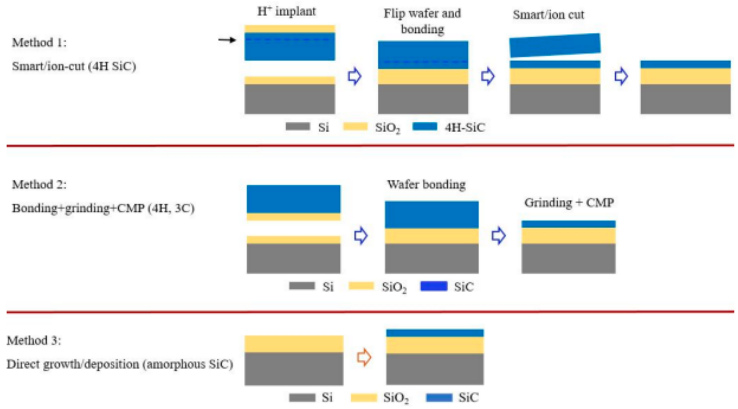

Fig. 2.16: Three distinct approaches for SiCOI platforms [98].

decade, significant efforts have been devoted to the optimization of ion-cutting technique [99–103]. The fabrication process is briefly presented as follows. Firstly, a high-purity semi-insulating 4H-SiC wafer is processed by a H^+ implantation. The H^+ implantation caused the formation of a damaged layer at a distance from the implantation surface adjusted by varying the implantation energy. Both SiC and Si wafers are thermally oxidized and treated by the standard chemical cleaning procedure with RCA solution. Then, SiC and Si wafers are bonded together at ambient temperature. Finally, the bonded wafer was annealed removing the excess SiC layer at the depth of the implanted H^+ ions. Despite the ion-cutting method provides an easy fabrication process at the wafer scale, it suffers from relatively high losses in the initial state [16, 102].

An alternative approach is based on ***thinning and polishing technique***[104]. This method starts with the treatment of <0001> 4H-SiC and Si wafers using RCA cleaning. A SiO_2 layer is deposited on both wafers through thermal wet oxidization. The wafers are then bonded together at room temperature, followed by annealing to enhance the bonding strength. The SiC layer's thickness is successively reduced first by a grinding process and then by reactive ion etching (RIE) to achieve the desired thickness. This method has also been applied to create a 3C-SiCOI substrate [105]. In this case, two Si substrates are initially prepared, followed by epitaxially growing a 3C-SiC thin film on one Si wafer. After the bonding process, as the last step, The top Si substrate is then removed resulting in the formation of a 3C-SiCOI substrate.

Another alternative method for SiCOI is the direct deposition of amorphous Silicon Carbide (a-SiC) on the top of a SiO_2 layer thermally growth on a Si wafer. The deposition is by means of plasma-enhanced chemical vapor deposition (PECVD) [106].

A comparison in terms of the quality factors extracted from the resonator structure reported in literature employing the above-described fabrication methods is reported following. So far, the highest reported Q-factor for a micro-ring resonator based on the 3C-SiCOI platform is $2.42 \cdot 10^5$ at 1550 nm [105]. The quality factor of $1.6 \cdot 10^5$ is achieved on an a-SiC microring resonator [106]. Compared to 3C-SiC and a-SiC, 4H-SiC has recently demonstrated a higher value of quality factors. In contrast to both materials, hexagonal 4H-SiCOI exhibits significantly reduced inherent losses. Indeed, to date, a well-developed technique for growing wafer-scale crystals with well-controlled crystalline quality has been reached. Recently, several results have been obtained on 4H-SiCOI platforms using ion-cutting, and thinning-polishing methods. Concerning the ion-cutting method, Zheng et al. [102] reported a Q-factor of $7.3 \cdot 10^4$. So far, the thinning and polishing method based on 4H-SiC shows the best performance. In this context, the results of a microring with a Q-factor of $1.1 \cdot 10^6$ [107] and a micro-disk with a Q-factor of $7.1 \cdot 10^6$ [108] are reported. Despite the thinning and polishing method allows for low-power operation, the fabrication process is very expensive compared to other methods. However, one challenge in using SiC in quantum photonics is the need for SiCOI fabrication methods, the best performance is obtained from *thinning and bonding* method involves expensive and time-consuming processes together with issues regarding precise thickness control. On the other hand, the performance of the device based on *ion-cutting* is limited by the intrinsic absorption loss. It is suitable for large-scale integrated systems in which ultra-low power is not required.

Optical modulators

The employment of silicon carbide as a substrate for integrated photonics is still an emerging technology, and the existing literature provides limited examples of optical modulators. In the case of electro-optic modulators, they have been demonstrated on various platforms, including silicon, indium phosphide, and so on. Nevertheless, these modulators have exhibited several drawbacks and have not fully addressed the requirements of electro-optic systems. For instance, Si modulators rely on the free carrier dispersion effect, which inherently introduces absorption and nonlinearity, leading to degradation and distortion of optical modulation amplitudes. On the other hand, non-centrosymmetric materials, which exhibit the electro-optic (EO) effect, like the Pockels effect, offer a more promising solution. These materials allow for a linear change in refractive index in response to an applied electric field. In this context, lithium niobate (LN) has demonstrated a platform for high-performance electro-optic (EO) modulators with a significant electro-optic coefficient of $r_{33} = 27pmV^{-1}$. However, LN is not compatible with the complementary metal-oxide-semiconductor (CMOS) fabrication process, which limits its use in photonic applications. In contrast, SiC exhibits processing that is complementary metal-oxide-silicon (CMOS) compatible and has a good electro-optic coefficient, making it suitable for fast electro-optic modulators based on SiC. Although the Pockels effect in 3C-SiC was studied over three decades ago, the development of electro-optic modulators in SiC is relatively recent. Recently, a CMOS-driven electro-optic 3C-SiC modulator based on microring resonators has been demonstrated [26]. This modulator exhibits an electro-optic coefficient of approximately 1.5 pmV^{-1} supporting a maximum bit rate of up to 10 Gb/s and an extinction ratio of 3 dB.

Despite the presence of second- and third-order nonlinearities in silicon carbide, no modulator based on these effects has been experimentally realized thus far. While SiC exhibits strong Kerr nonlinearity, such modulators remain an unexplored area of research.

Moreover, an electro-optical modulation effect, due to free carrier depletion in a 4H-SiC slab, which was part of a commercial power Schottky diode was demostrated [109]. Here, modulation effects were observed in dynamic conditions, extending up to 500 kHz. This was achieved by applying reverse square pulses with an amplitude of 180 V and a 50% duty cycle.

Additionally, there are no reported instances in the existing literature of thermo-optic modulators implemented in silicon carbide. Recently, there have been promising developments in the field of thermo-optic phase shifters using amorphous silicon carbide (a-SiC) [110], providing a potential avenue for further exploration and experimentation in SiC-based thermo-optic modulation.

2.7 Simulation Tools

2.7.1 Physics-based numerical simulator

The numerical simulations reported in this thesis were conducted using Atlas simulation software developed by Silvaco. Atlas is a physics-based device simulator designed to predict the electrical characteristics of semiconductor devices and provide a comprehensive understanding of the physical mechanisms governing their operation. Unlike empirical modeling, which relies on analytical formulas to approximate existing data with good accuracy, physics-based simulation offers a deeper insight into the fundamental principles underlying device behavior.

To perform the numerical results, the simulator employs a grid in two- or three-dimensions, known as mesh. This mesh is composed of numerous grid points, called nodes, and the simulator solves a system of differential equations derived from Maxwell's laws at each of these nodes. This approach allows it to simulate and predict the movement of transport of charge carriers within the device structure.

ATLAS operates based on two types of input files that contain all the necessary information for proper execution, and it generates three main types of output files. The input files consist of the *command file*, which contains execution commands, and the *structure files* that define the device's physics. The output files include the *run-time file* which comprises progress, error, and warning messages, the *log files* storing voltage and current values, and the *solution file*, containing values of solution variables at specific bias points.

For the import and export of these files, the simulator software integrates various programs that interact with each other. Typically, the key programs include Deckbuild, Devedit, Athena, and Tonyplot.

Mesh specification plays a fundamental role in determining the accuracy and numerical efficiency of simulations. It involves user-defined horizontal and vertical lines that define the spatial domain of the simulation. The appropriate configuration of the mesh is crucial for obtaining reliable and meaningful results from the simulations.

Physical Model

As previously mentioned, ATLAS is a physic-based device simulator designed to predict the electrical behavior of a device. In the following sections, the equations derived from Maxwell's laws that govern the physics of semiconductor devices will be presented. To ensure a reliable prediction of the working principles of electronic devices, it is essential not only to accurately define the device structure but also to establish an appropriate system of physical models. Additionally, the simulation results are carried out by solving the fundamental semiconductor equations, i.e. Poisson's equation, the continuity equations, and the drift and diffusion current equations. By solving these equations, it becomes possible to derive the electrical characteristics and current-voltage (I-V) relationships of electronic devices by applying various stimuli in the form of voltages, photons, or thermal energy.

ATLAS solves the equations on a discrete mesh within a predetermined device region, employing the Newton/Gummel/Block iterative method and applying relevant boundary conditions. This process provides the potential distribution, as well as the distributions of electrons and holes. Once a numerical solution for the equations is obtained, the simulated electrical characteristics can be visualized and analyzed using *tonyplot* tool, enabling comparisons with experimental data.

In the following sections, the basic equations of the carrier transports and the physical models consist of *bandgap narrowing*, *incomplete ionization*, *Chaughey-Thomas*, *Schokley-Read-Hall* (*SRH*) and *Auger recombination* implemented in Atlas are detailed presented.

Basic semiconductor equations

In order to investigate the behaviors of an electronic device, the physics-based device simulator employs a model consisting of a set of fundamental equations that correlates the electrostatic potential and carrier densities within a defined simulation domain. These equations, derived from Maxwell's law, consist of Poisson's equation, the continuity equations, and the transport equations.

The **Poisson's equation** relates the electrostatic potential to the space charge density. It's defined as follows:

$$div(\epsilon_s, \nabla\Psi) = -\rho \tag{2.44}$$

where, ϵ_s is the dielectric constant of the semiconductor, Ψ is the electrostatic potential, and ρ is the local space charge density that comprises both mobile and fixed charges, including electrons, holes, and ionized impurities. From the potential gradient, it is possible to deduce the electric field as indicated below:

$$\vec{E} = \nabla\Psi \tag{2.45}$$

The continuity equation for electrons and holes is:

$$\frac{\partial n}{\partial t} = \frac{1}{q} div\vec{J_n} + G_n - R_n \tag{2.46}$$

$$\frac{\partial p}{\partial t} = \frac{1}{q} div\vec{J_p} + G_p - R_p \tag{2.47}$$

where, n and p are the electron and hole concentration, J_n, G_n, and R_n are the current density, the generation and recombination rate of the electron, respectively. J_p, G_p and R_p are the same quantities for hole.

The current density is derived by applying approximations and simplifications to the Boltzmann transport theory. Among the different transport models, the drift-diffusion model is the simplest, as it doesn't introduce any independent variables in addition to Ψ, n, and p. The more conventional formulation of drift-diffusion equations is:

$$\vec{J_n} = qn\mu_n\vec{E_n} + qD_n\nabla n \tag{2.48}$$

$$\vec{J_p} = qn\mu_p\vec{E_p} + qD_p\nabla p \tag{2.49}$$

where, E is the electric field, μ_n and μ_p are the electron and hole mobilities, and D_n and D_p are the electron and hole diffusion coefficients. According to Einstein's relation, the diffusivity can be expressed in the following form:

$$D_n = \frac{kT_L}{q}\mu_n \tag{2.50}$$

$$D_p = \frac{kT_L}{q}\mu_p \tag{2.51}$$

Energy Bandgap

As temperature increases, the lattice constant increases leading to a reduction of the band-gap. The following formula describes this phenomenon:

$$E_g(T) = E_g(0) + \alpha_{E_g}\left[\frac{300^2}{300+\beta_{E_g}} - \frac{T_L^2}{T_L^2-\beta_{E_g}}\right] \tag{2.52}$$

Incomplete ionization

The process of ionizing doping is a crucial phenomenon within semiconductors, as it has a substantial impact on the concentration of free-carriers and, therefore, the semiconductor's properties. The degree of ionization can vary, being either complete or incomplete at a fixed temperature, depending on whether the impurity atoms have released (n-type doping) or accepted (p-type doping) electrons completely. Unlike Si, which exhibits complete ionization at room temperature, SiC, even at room temperature, shows an incomplete ionization due to the higher ionization energy of its dopants atoms [18]. As a result, a fraction of the dopant atoms are not thermally activated but remain trapped within the band gap without ionization. This phenomenon is referred to as *freeze-out* and is significant at low temperatures in traditional semiconductors. The principal p-type dopant in 4H-SiC is Aluminum and can occupy either a hexagonal or a cubic silicon site, with ionization energies of 197.9 and 201.3 meV, respectively [111]. Meanwhile, the main n-type dopants are nitrogen and phosphorus. Nitrogen replaces carbon and, when located on a hexagonal C-site, has an ionization energy of 61.4 meV. Phosphorus substitutes for silicon and, when found on a cubic Si-site, possesses an ionization energy of 60.7 meV [111]. The density of effective ionized acceptors and donors are represented as N_A^- and N_D^+), expressed as following [112]:

$$N_A^- = \frac{N_A}{1 + g_V e^{\frac{E_V + E_A - E_{F_p}}{kT}}} \tag{2.53}$$

$$N_D^+ = \frac{N_D}{1 + g_C e^{\frac{E_C + E_D - E_{F_n}}{kT}}} \tag{2.54}$$

where, N_A and N_D are the acceptor and donor concentrations, E_A and E_D are the acceptor and donor energy levels, E_{F_n} and E_{F_p} are the quasi-Fermi energy levels for electrons and holes, whereas g_V and g_C are the appropriate degeneracy factors for the valence and conduction band.

Bandgap narrowing

In the presence of a high impurity concentration, the electron and hole-related energy bands are attracted toward each other, causing a shrinkage of the bandgap. This effect, known as *bandgap narrowing*, is described by the *Lindefelt's model* for 4H-SiC [113]:

$$\Delta E_{g_A} = A_A \left(\frac{N_A^-}{10^{18}} \right)^{\frac{1}{2}} + B_A \left(\frac{N_A^-}{10^{18}} \right)^{\frac{1}{3}} + C_A \left(\frac{N_A^-}{10^{18}} \right)^{\frac{1}{4}} \tag{2.55}$$

$$\Delta E_{g_D} = A_D \left(\frac{N_D^+}{10^{18}} \right)^{\frac{1}{2}} + B_D \left(\frac{N_D^+}{10^{18}} \right)^{\frac{1}{3}} + C_D \left(\frac{N_D^+}{10^{18}} \right)^{\frac{1}{4}} \tag{2.56}$$

where $A_{A,D}$, $B_{A,D}$ and $C_{A,D}$ are constants for 4H-SiC.

Analytic mobility model: Caughey-Thomas Model

An accurate description of the carrier mobility is essential for estimating the performance of semiconductor devices. This parameter takes into account all the microscopic phenomena that limit the motion of charge carriers, including lattice vibrations (phonons), impurity ions, other carriers, surfaces, and other material imperfections. For this purpose, the mobility equations are therefore functions of the local electric field, lattice temperature, and doping concentration. It is necessary to differentiate between two cases related to the strength of the electric field: high-field and low-field mobility. Both of the cases presented below refer to the *Caughey-Thomas model*.

For low field, the carrier mobility is commonly denoted by μ_{n0} and μ_{p0} and relies on phonon and impurity scattering. The following analytic functions are used:

$$\mu_{0n,p} = \mu_{0n,p}^{min} \left(\frac{T}{300K} \right)^{\alpha_{n,p}} + \frac{\mu_{0n,p}^{max} \left(\frac{T}{300K} \right)^{\beta_{n,p}} - \mu_{0n,p}^{min} \left(\frac{T}{300K} \right)^{\alpha_{n,p}}}{1 + \left(\frac{T}{300K} \right)^{\gamma n,p} \left(\frac{N}{N_{n,p}^{crit}} \right)^{\delta_{n,p}}} \tag{2.57}$$

where, N is the local (total) concentration of the ionized impurities, $\mu_{0n,p}^{min}$ and $\mu_{0n,p}^{max}$ are two reference parameters for the maximum and minimum mobility, $N_{n,p}^{crit}$ is the doping concentration at which the mobility is halfway between the mobility in highly doped and undoped material, and $\alpha_{n,p}$, $\beta_{n,p}$, $\gamma n,p$, and $\delta_{n,p}$ are fitting parameters.

Regarding high electric field mobility, the carrier mobility decreases as the electric field increases because carriers that gain energy become more extensively involved in scattering processes. The carrier mobilities are:

$$\mu_{n,p}(E) = \mu_{0n,p}\left[\frac{1}{1+\left(\frac{\mu_{0n,p}E}{v_{satn,p}}\right)^{\beta_{n,p}}}\right]^{\frac{1}{\beta_{n,p}}} \tag{2.58}$$

where, μ_{n0} and μ_{p0} are the carrier mobility obtained from the previous model, β_n and β_p are constant coefficients, and $v_{sat,n}$ and $c_{sat,p}$ are the saturation velocity for electron and hole.

Recombination Model: Shockley-Read-Hall and Auger

Carrier generation-recombination is a peculiar process through which the semiconductor returns to its equilibrium state (np=n_i^2) after being disturbed from it. In this section, the recombination process is presented. These processes are critical in determining the behavior of semiconductor devices and can vary depending on whether the material has a direct or indirect bandgap. In direct bandgap semiconductors, such as Gallium Arsenide (GaAs), recombination is predominantly dominated by band-to-band recombination, which results in the emission of photons. On the other hand, in indirect band-gap semiconductors, such as SiC, recombination is primarily characterized by indirect transitions through energy states localized within the bandgap. In this context, the processes responsible for the recombination are Shockley-Read-Hall and Auger. These mechanisms lead to a non-radiative recombination, meaning that no photons are emitted. In this section, these models are examined.

The ***Shockley-Read-Hall recombination***, also called *trap-assisted recombination*, occurs via energy levels, traps, or defects, located inside the bandgap of the semiconductors. Four possible carrier transitions can occur during this process: the capture of electrons from the conduction band by a defect, the thermal emission of captured electrons from the defect to the conduction band, and equivalent transitions of holes between defects and the valence band. The SHR recombination rate can be estimated using the equation proposed by [114]:

$$R_{SRH} = \frac{pn - n_i^2}{\tau_p\left(n + n_i^2 e^{\frac{E_T-E_i}{k_B T}}\right) + \tau_n\left(p + n_i^2 e^{\frac{E_T-E_i}{k_B T}}\right)} \tag{2.59}$$

where, n_i is the effective intrinsic carrier concentration, E_T is the energy level of the trap, and E_i is the intrinsic Fermi level. τ_n and τ_p are electron and hole recombination lifetime, respectively, and could be calculated using the following formula:

$$\tau_{n,p} = \frac{\tau_{0n,p}}{1+\left(\frac{N}{N_{n,p}^{SRH}}\right)} \tag{2.60}$$

begin, $\tau_{0n,p}$ and $N_{n,p}^{SRH}$ are process-dependent fitting parameters, and N is the total doping density.

Auger recombination involves three carriers and occurs when the excess energy generated during electron-hole recombination is transferred to another electron in the conduction band or a hole in the valence band. This process has a significant impact on regions with high doping levels. The Auger recombination rate can be estimated using the formula [115]:

$$R_{aug} = C_n\left(pn^2 - nn_i^2\right) + C_p\left(np^2 - pn_i^2\right) \tag{2.61}$$

where C_n and C_p are the Auger coefficients for electrons and holes, respectively.

Impact ionization

In the presence of a sufficiently high reverse bias, the resulting electric field within the space charge region will be enough to accelerate free carriers acquiring high energy. Indeed, this process involves the generation of electron-hole pairs through the collision of high-energy electrons with atoms or other electrons within the semiconductor material. In order to acquire sufficient energy, two conditions must be respected: the electric field must reach a sufficiently high level, and the distance between collisions of the free carriers must be adequate to allow for effective acceleration. The impact ionization can cause breakdown or destructive electrical discharge in semiconductor devices when excessive reverse voltage is applied.

The general impact ionization process can be described by the following equation:

$$G = \alpha_n|\vec{J}|_n + \alpha_p|\vec{J}|_p \tag{2.62}$$

here, G is the local generation rate of electron-hole pairs, and $J_{n,p}$ is the current density for electrons and holes. The coefficients $\alpha_{n,p}$ are the ionization coefficients, representing the number of electron-hole pairs generated by a carrier per unit distance traveled. These coefficients can be determined using a model proposed by Selberherr [116], as expressed by the equation:

$$\alpha_{n,p} = A_{n,p}e^{-\left(\frac{B_{n,p}}{E}\right)^{\beta_{n,p}}} \tag{2.63}$$

where, E is the electric field in the local current flow direction, $A_{n,p}$, $B_{n,p}$, and $\beta_{n,p}$ are material-dependent physical parameters.

2.7.2 Beam Propagation Method (BPM)

To design and simulate the behavior of the Fabry-Perot cavity described in Section 4.1.2, the commercial photonic simulation package BEAMProp inside the RSoft environment is employed [117]. BeamProp is based on the finite-difference beam propagation method (BPM).

The BPM method uses finite difference methods to solve the well-known parabolic or paraxial approximation of the Helmholtz equation to find field distributions in a waveguiding structure. It is given as follows:

$$\left(\nabla^2 + k^2\right)\Phi = \frac{\partial^2\Phi}{\partial x^2} + \frac{\partial^2\Phi}{\partial y^2} + \frac{\partial^2\Phi}{\partial z^2} + k^2\Phi = 0 \tag{2.64}$$

where spatially dependent wavenumber is $k(x,y,z) = \frac{2\pi}{\lambda_0} n(x,y,z)$ and n(x,y,z) is the refractive index space distribution. Φ is defined in terms of the optical field distribution and phase as:

$$\Phi(x,y,z) = u(x,y,z)e^{j\bar{k}z} \tag{2.65}$$

where $\bar{k}$ is a constant describing the average phase change of Φ in z-direction. The basic BPM equation in three dimensions became:

$$\frac{\partial u}{\partial z} = \frac{i}{2\bar{k}}\left(\frac{\partial^2 u}{\partial x^2} + \frac{\partial^2 u}{\partial y^2} + \left(k^2 - \bar{k}^2\right)u\right) \tag{2.66}$$

Simplification to two dimensions is obtained by neglecting any dependence on y. Given an input field, u(x,y,z=0), the above equation determines the evolution of the field in the space z>0.

2.7.3 Optical simulation in Lumerical

The simulation and theoretical analysis of the modulator, which is based on the thermo-optic effect, were carried out using Lumerical simulation software [118]. Developed by Ansys, Lumerical is a comprehensive software solution for photonics simulations, which enables the design of various photonic components, circuits, and systems.

Lumerical integrates four distinct tools: Lumerical DEVICE, Lumerical MODE, Lumerical Interconnect, and Lumerical FDTD.

In the subsequent section, an exploration of the operational principles of Lumerical DEVICE and Lumerical MODE will be undertaken. These tools were employed in this research to conduct the simulation and theoretical analysis of the thermo-optic modulator, providing valuable insights into the realm of integrated photonics.

Lumerical DEVICE [119] is an advanced, finite element multiphysics simulation environment that is equipped with solvers, including DGDT, FEEM, CHARGE, and HEAT. DGDT and FEEM conduct optical simulations using different methods, Discontinuous Galerkin Time-Domain, and Finite Element Eigenmode, respectively. On the other hand, CHARGE and HEAT are specialized in addressing charge and heat transport-related issues. In the simulations conducted in this thesis, the HEAT [120] solver from Lumerical DEVICE was employed. This particular solver calculates the thermal response to Joule heating in electrically driven systems. It achieves this by solving the heat transport equation:

$$\rho c_p \frac{\partial T}{\partial t} - \nabla \cdot (k \nabla T) = Q \tag{2.67}$$

where ρ is the mass density, c_p is the specific heat, k is the thermal conductivity and Q is the applied heat energy transfer rate.

Regarding the electrical part, the electric current equation is considered:

$$J = \sigma E = -\sigma \nabla V \tag{2.68}$$

where σ is the electrical conductivity, E is the electric field, and V is the applied bias. It is combined with the auxiliary continuity equation:

$$\frac{\partial \rho}{\partial t} = -\nabla \cdot J \tag{2.69}$$

where ρ is the charge density. In steady-state, $\partial\rho/\partial t = 0$, and the combination of the electric current equation with the continuity equation results in:

$$\nabla \cdot (\sigma E) = 0 \tag{2.70}$$

and the electrical power dissipated by the Ohmic effect is:

$$P = J \cdot E = \sigma E^2 \tag{2.71}$$

This approach is applied to address heat transport questions, considering the heat energy transfer rate Q=P, which accounts for the Joule effect. The utilization of the HEAT solver plays a pivotal role in understanding the thermal aspects of electrically driven systems.

Lumerical MODE [121] is a comprehensive optical waveguide design environment. It comprises three solvers: Finite Difference Eigenmode (FDE), variational FDTD, and Bidirectional Eigenmode Expandion (EME) solver.

The Finite-Difference Eigenmode (FDE) is a mode calculator solver that calculates the spatial profile and the modes by solving Maxwell's equations on a cross-sectional mesh waveguide. Particularly, the solver calculates the mode field profiles, effective index, and loss. The method is based on the work proposed by Zhu and Brown in [122] in which Maxwell's equations are formulated into a matrix eigenvalue problem and solved using sparse matrix techniques to obtain the effective index and mode profiles of the waveguide modes.

3

Material characterization

This chapter focuses on the analysis of the optical properties of two wide bandgap semiconductor materials, Silicon Carbide (SiC) and Gallium Nitride (GaN). The experimental results are of significant relevance for exploring the potential of these materials in photonics applications. In order to characterize the optical properties in terms of the complex refractive index, a spectroscopic ellipsometry method in a wide spectrum range has been employed. Especially, the studied samples include 4H-SiC, and 3C-SiC with varying doping levels (lightly and heavily doped) and semi-insulating GaN. Additionally, this study investigates the temperature dependence of the thermo-optic coefficient, which measures the variation of the refractive index as a function of temperature, in two samples of 4H-SiC and GaN. The experimental measurements have been conducted in a wide temperature range, reaching approximately 500K, in visible (λ=632nm) and near-infrared (λ=1550 nm) spectrum.

3.1 Spectroscopic Ellipsometry

3.1.1 Theory of spectroscopic ellipsometry

Spectroscopic ellipsometry is a non-invasive and non-destructive optical technique employed for the determination of thin film properties, including thickness, complex refractive index, and dielectric constant. It relies on the changes in the polarization state of the light beam reflected from the surface of the sample.

The ellipsometer used in this experiment is a phase-modulated one, UVSEL manufactured by HORIBA Jobin Yvon. It exploits a photoelastic modulator to perform polarization modulation at a frequency of 50kHz without mechanical movement [123]. Compared with the conventional ellipsometers, this phase modulation-based approach enables rapid optical characterization of optical and geometric properties of thin films, allowing a high level of sensitivity across a broad spectral range. Concerning its working principle, a schematic diagram of a UVISEL phase-modulated ellipsometer is depicted in Fig. 3.1.

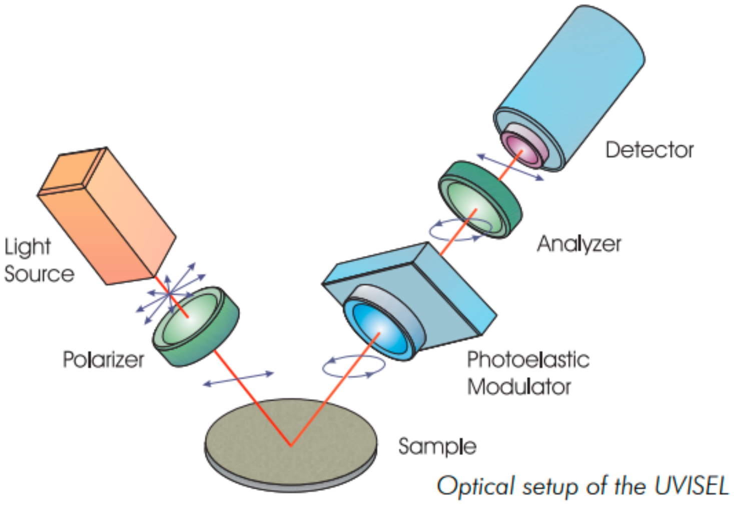

Fig. 3.1: Schematic representation of the experimental setup [123].

It consists of two optical arms, with a sample holder placed between them. The first arm, at the entry, comprises a light source, whose optical beam passes through a polarizer to establish its incident polarization state, typically linear polarization. The light source used is a Xenon lamp that covers a broad spectral range spanning from 190 to 2100 nm. This optical beam is directed onto the sample at an incident angle of approximately 70°, resulting in a change in the polarization state upon reflection at a specific angle. The second arm, the exit arm, consists of a photoelastic modulator, an analyzing polarizer, and a photodetector that resolves the polarization state of the reflected beam. The reflected light from the sample exhibits an elliptical polarization state, containing information regarding the geometric and optical parameters of the sample. Both the incident and reflected optical radiation can be categorized as p- and s-polarized light.

The polarization state of the reflected optical beam can be expressed in terms of two angles, Ψ and Δ, representing the amplitude ratio and the phase difference, respectively. Ellipsometric measurements provide data in the form of a complex reflection ratio (ρ) defined as follows:

$$\rho = \frac{r_p}{r_s} \tag{3.1}$$

where r_p and r_s are the complex Fresnel coefficients of the polarized light parallel and perpendicular to the incident plane, respectively. As previously described in Section 2.4, these coefficients are related to the amplitude and phase of the reflected wave in the p-plane and s-plane to those of the incident polarized waves in the p-plane and s-plane, respectively. The reflection coefficients r_p and r_s for p- and s-polarized light waves are related to the amplitude and phase differences in their electric field components. Their expressions are defined as follows:

$$r_p = \frac{|E_p^{ref}|}{|E_p^{inc}|} e^{i(\delta_p^{ref} - \delta_p^{inc})} \tag{3.2}$$

$$r_s = \frac{|E_s^{ref}|}{|E_s^{inc}|} e^{i(\delta_s^{ref} - \delta_s^{inc})} \tag{3.3}$$

where $|E_p^{ref}|$ and $|E_p^{inc}|$ are the amplitude of the electric field of the reflected and incident radiation in the p-component. Instead, $|E_s^{ref}|$ and $|E_s^{inc}|$ relate to the s-component. δ represents the phase of these electric fields. According to the previous expressions, it is possible to rewrite the Eq. 3.1 with:

$$\rho = \frac{r_p}{r_s} = \frac{|r_p|}{|r_s|} e^{i(\delta_p - \delta_s)} = tan\Psi e^{i\Delta} \tag{3.4}$$

where

$$\frac{|r_p|}{|r_s|} = tan\Psi \tag{3.5}$$

$$\delta_p - \delta_s = \Delta \tag{3.6}$$

The Eq. 3.4 is known as the *fundamental equation of ellipsometry*. As shown in Eq. 3.1, ρ is expressed as a function of Ψ and Δ which are analytically related to the real (ϵ_1) and imaginary (ϵ_2) part of the dielectric function ϵ of the matter, and so to the refractive index of the material. In ellipsometric measurements, the reflected polarization state is converted into an electronic signal by the photodetector, expressed in terms of I_c and I_s. The measured data are used to describe a model that exploits mathematical relations, known as *dispersion formula*, to evaluate the geometric and optical properties of the material by adjusting specific fit parameters.

Spectroscopic ellipsometry was employed to investigate the optical properties of Gallium Nitride and Silicon Carbide (4H-SiC and 3C-SiC) with varying doping concentrations. The results from these ellipsometry measurements are integral to the research studies presented in the next sections.

3.1.2 Experimental results: 4H-SiC and 3C-SiC

The optical properties, specifically refractive index (n) and extinction coefficient (k), of 4H-SiC and 3C-SiC were characterized. In the case of 4H-SiC, the samples under investigation exhibit three distinct doping levels. All these samples are <0001> oriented and comprise a 2 mm-thick semi-insulating bulk with a resistivity $\rho > 10^5 \Omega cm$, and two heavily-doped n-type substrates, each with a thickness of 250 μm and doping levels of $10^{18} cm^{-3}$ and $10^{19} cm^{-3}$ [124]. On the other hand, the studied sample based on 3C-SiC is a three-layer p-i-n structure epitaxially grown, whose growing was performed by Advanced Epi [125], on a commercial 6-inch SOI wafer [126]. Specifically, the first one is a 50 nm-thick heavily doped p-type ($N_A = 10^{19} cm^{-3}$) layer, the next one is a 100 nm-thick intrinsic layer, and the last one is a 50 nm-thick highly doped n-type ($N_D = 10^{19} cm^{-3}$) layer. The details are summarized in Table 3.1.

Parameters	4H-SiC			3C-SiC p-i-n		
Doping (cm^{-3})	10^{15}	10^{18}	10^{19}	*n-type* 10^{19}	10^{15}	*p-type* 10^{19}
Thickness	2mm	250 μm	250 μm	50 nm	100 nm	50 nm

Table 3.1: Doping and thickness of the samples based on 4H-SiC and 3C-SiC employed for the ellipsometry characterization.

Spectroscopic ellipsometry data were recorded in a wavelength scanning range from 300 to 1600 nm, with a step of 5 nm, with an incident angle of 70°. The acquired data from the ellipsometry were fitted by the classical dispersion model. It is based on the sum of the single and double Lorentz, and Drude oscillators [127]:

$$\bar{\epsilon}(\omega) = \epsilon_\infty + \frac{(\epsilon_s - \epsilon_\infty) \cdot \omega_t^2}{\omega_t^2 - \omega^2 + j\Gamma_0 \cdot \omega} + \frac{\omega_p^2}{-\omega^2 + j\Gamma_d \cdot \omega} + \sum_{i=1}^{2} \frac{f_i \cdot \omega_{0i}^2}{\omega_{0i}^2 - \omega^2 + j \cdot \gamma_i \cdot \omega} \tag{3.7}$$

Fitting of experimental data leads to the evaluation of the dielectric function $\bar{\epsilon} = \epsilon_1 - j\epsilon_2$. Assuming that $\bar{\epsilon} = n^2 = (n - jk)^2$ the complex refractive index is extracted.

Concerning the characterization of 4H-SiC, the measured dispersion curves of 4H-SiC optical constants led to the refractive index and extinction coefficient which are shown in Fig. 3.2a and in Fig. 3.2b, respectively.

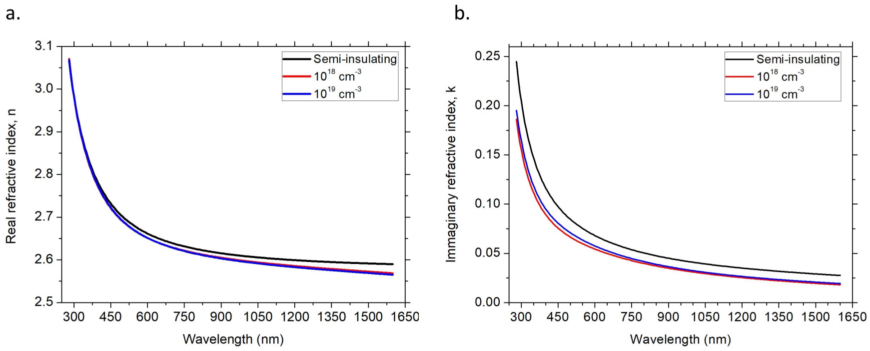

Fig. 3.2: Refractive index (a) and extinction coefficient (b) of 4H-SiC substrate.

On the other hand, the ellipsometry characterizations of the *p-i-n* structure based on 3C-SiC above-described are depicted in Fig. 3.3.

The experimental data presented here are in good agreement with previously available literature results [128, 129].

The experimental results for both materials reveal a decrease in the refractive index of SiC with an increasing doping concentration. This effect is relatively moderate

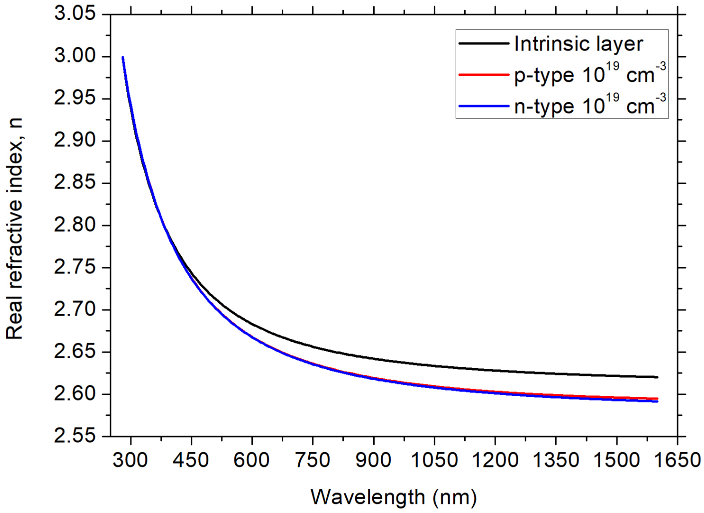

Fig. 3.3: Real part of the refractive index of *p-i-n* structure based on 3C-SiC.

at shorter wavelengths and becomes progressively more pronounced upon increasing wavelength into the infrared range. Regarding the extinction coefficient, which is directly related to the absorption through the equation $\alpha = \frac{4\pi k}{\lambda}$, it exhibits a rapid increase at wavelengths corresponding to energies which are higher than the energy bandgap (around $\lambda = 380nm$ for 4H-SiC). As the wavelength increases, resulting in lower energies, the extinction coefficient tends toward zero, corresponding to minimal light absorption in the medium.

3.1.3 Experimental results: GaN

In this case, the sample under investigation is a semi-insulating GaN substrate with a resistivity $\rho > 10^6\ \Omega cm$. The substrate is oriented along the <0001> crystallographic direction and has a thickness of 0.35 mm. The data acquisition process involving ellipsometry follows the same methodology as previously described for SiC. However, there is a variation in the dispersion model employed for GaN, which is the Adachi-New Forouhi model. This model allows for a more accurate representation of the optical properties and behavior specific to GaN. It is described as follows:

$$\epsilon(E) = \epsilon_0(E) + \epsilon_1(E) \tag{3.8}$$

where

$$\epsilon_0 = A_0 \left\{ \frac{f(X_0)}{E_g^{3/2}} + \frac{f(X_{S0})}{2(E_g + \Delta_0)^{3/2}} \right\} \tag{3.9}$$

$$\epsilon_1(E) = (n_1(E) + ik_1(E))^2 \tag{3.10}$$

more detail about the expressions is reported in [130].

The experimental results of the refractive index and extinction coefficient are reported in Fig 3.4. These results are in good agreement with others presented in literature [131].

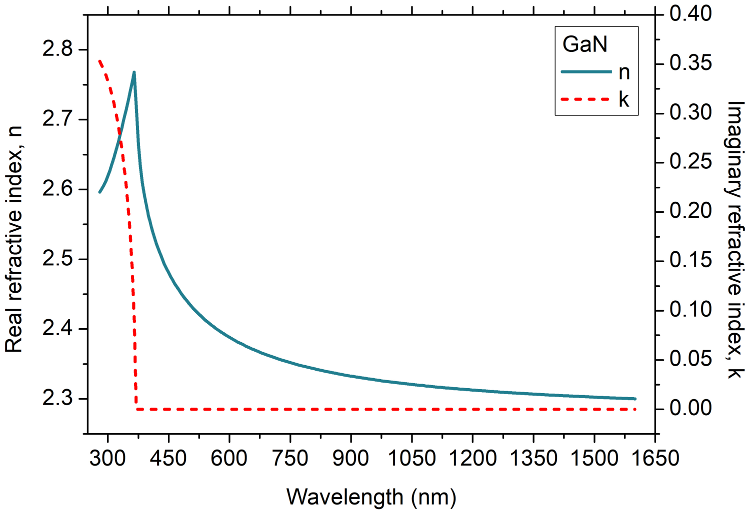

Fig. 3.4: Real and imaginary part of the refractive index of GaN substrate.

3.2 Thermo-optic effect in Silicon Carbide and Gallium Nitride

The knowledge of the optical properties of the materials employed in photonics, and in particular their temperature dependence, is essential for the precise design of future optical devices. Especially, the evaluation of the thermo-optic effect, which characterizes how the refractive index changes with temperature, plays a key role. However, experimental results for wide band-gap semiconductors, such as Silicon Carbide and Gallium Nitride, are currently limited. In this section, the experimental data for semi-insulating 4H-SiC and GaN in the visible (λ=632 nm) and near-infrared (λ=1550 nm) ranges are reported [132–134]

3.2.1 Theory of thermo-optic effect and its state of art

To ensure a proper design of optoelectronic devices, the evaluation of the temperature dependence of the optical properties, particularly the refractive index, of the materials is required. The temperature has a significant impact on the refractive index, through a phenomenon known as *thermo-optic effect* (TOE). Neglecting the TOE in the device design may lead to adverse effects on its performance. In fact, the temperature-induced variation in the refractive index could cause an incorrect functioning of optical devices when their resonance wavelength depends on the refractive index. These devices include distributed feedback lasers, optical couplers, interferometers, and waveguides. Even a slight thermally induced resonance drift may cause wavelength detuning or phase mismatch, degrading the nonlinear processes, and completely changing the device behavior.

On the other hand, understanding the temperature dependence of the refractive index could be exploited to design and develop thermally activated devices. A variety of optical devices, such as switches, modulators [135], tunable lasers, wavelength demultiplexers, and filters employ the thermo-optic effect in order to obtain a resonance wavelength shift.

Few studies are reported in literature regards the experimental evaluation of the thermo-optic coefficient, $\frac{\partial n}{\partial T}$, for wide bandgap semiconductors. These include methods such as interferometry [136], z-scan [137], thermal lens [138], and light-induced transient thermal grating techniques, which is also called a time-resolved four-wave mixing [139, 140]. Recently, the temperature dependence of the refractive index of 4H-SiC and GaN was demonstrated across a wavelength spectrum spanning from their respective near band edge (λ=392 nm for 4H-SiC, λ=367 nm for GaN) to infrared (λ=1700 nm). These measurements, performed in a temperature range from RT to T=500 K, were conducted employing an optical interference method[128]. At a specific wavelength of λ=450 nm, the TOCs of 4H-SiC and GaN were $7.8 \cdot 10^{-5} K^{-1}$ and $1.6 \cdot 10^{-4} K^{-1}$, respectively. Moreover, employing the method of minimum deviation, the temperature-dependent refractive index of 4H-SiC and 6H-SiC was investigated within a temperature range extending from 293 K to 493 K. This investigation is defined in a spectral range from λ=404.7 nm to λ=2325.4 nm [141]. For 4H-SiC, at the wavelength of λ=450 nm, at T=493 K, a TOC of $8.18 \cdot 10^{-5} K^{-1}$ was measured, closely aligned with the value reported in Ref [128]. At the same temperature, the TOC of 6H-SiC at the wavelength of λ=1523 nm was evaluated as $5.94 \cdot 10^{-5} K^{-1}$, which is in agreement with the value of $5.54 \cdot 10^{-5} K^{-1}$ reported in Ref [142].

Despite these reported methods have been implemented across various wavelength ranges, there is a lack of studies related to the direct dependence on the temperature of TOC for these semiconductors. So far, the knowledge of the temperature dependence of the thermo optic coefficient of 4H-SiC and GaN in the visible and near-infrared range, over a wide temperature range, is still lacking.

3.2.2 Experimental setup

An experimental setup has been assembled to evaluate the temperature dependence of the thermo-optic coefficient of two samples of 4H-SiC and GaN. Both of them are commercially available <0001> oriented semi-insulating thick substrates [124]. The main geometrical and physical properties of both samples are reported in Table 3.2.

Parameter	**4H-SiC**	**GaN**
Substrate	Semi-insulating <0001>	
Resistivity ($\Omega \cdot cm$)	$> 10^5$	$> 10^6$
Roughness (nm)	<0.5	<0.5
Energy gap (eV) (T=300K)	3.2	3.43
Thickness, L (mm)	2	0.35
Thermal expansion coefficient, α ($10^{-6} K^{-1}$)	$-1.0971 \cdot 10^{-5} T^2$ $+1.8967 \cdot 10^{-2} T - 1.9755$ [143]	$3.92 \cdot 10^{-3} T + 2.42$ [144]
Refractive index, n (T=300 K, λ=632.8 nm)	2.6526 (see Fig. 3.2)	2.3780 (see Fig. 3.4)
Refractive index, n (T=300 K, λ=1550 nm)	2.5908 (see Fig. 3.2)	2.3780 (see Fig. 3.4)

Table 3.2: Main features of the 4H-SiC and GaN samples.

The analysis is carried out in a temperature range from RT to about 500 K at two wavelengths. Specifically, at the principal optical communication wavelength of λ=1550 nm and at a wavelength in the visible range of λ=632.8 nm.

In order to characterize the thermo-optic coefficient, an interferometric method [13, 142] based on a Fabry-Perot cavity is exploited. As explained in Section 2.5.1, a Fabry-Perot cavity consists of two partially reflecting mirrors which are planar and separated by a distance of L. When an optical beam is launched in one of these mirrors, the optical beam within the cavity is reflected many times between the two surfaces and a multiple-beam reflection interference occurs. Because both samples are double-side polished at an optical grade, they effectively behave as Fabry–Perot (FP) cavities.

Fig. 3.5 shows a schematic representation of the experimental setup employed in this study, with individual components detailed in this section. The sample is contained in a fiber-to-fiber U-bench (Thorlabs, FBC-1550-FC) with a 3 cm spacing. Fig. 3.6 is a labeled photograph showing the U-bench system. Through an optical fiber system, firstly the optical beam is launched into the sample, and then the transmitted optical beam is collected. In order to ensure uniform heating at the desired temperature, the sample is placed on a ceramic-resistive heater. By applying a voltage across the resistor via a source-meter, the temperature increases due to Joule heating. The generated heat is transferred to the sample, causing it to heat up, consequently. The experimental measurements are started after an alignment procedure to ensure

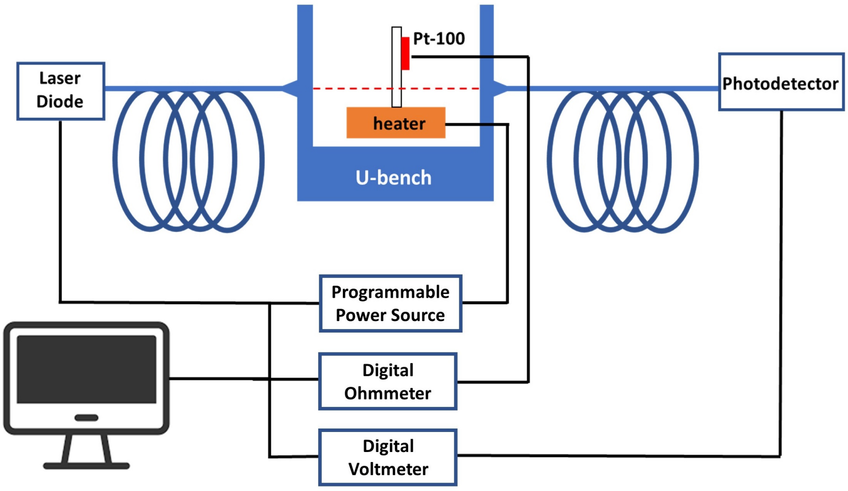

Fig. 3.5: Schematic diagram of the experimental setup used for characterization of TOC as a function of temperature.

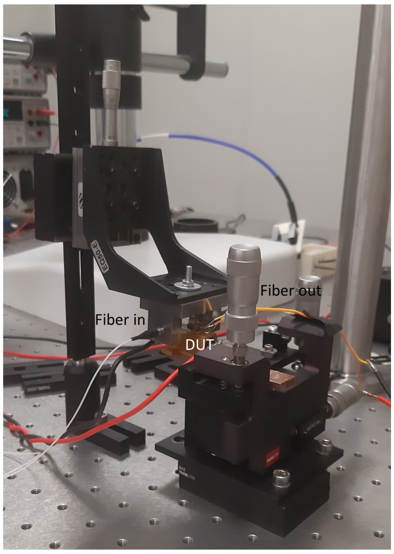

Fig. 3.6: Picture of the experimental setup.

that the optical beam is launched orthogonal to the surface. The actual temperature of the sample is monitored by a high-sensitive PT-100 sensor glued onto its surface close to the monochromatic light spot. Its measured resistance value is evaluated by a digital Ohmmeter. Concerning the optical beam, it is launched into the fiber by a remotely controlled tunable laser diode. Finally, the transmitted optical beam is collected at the output by a high-speed Si photodetector (Thorlabs, DET210/M)[145] investigations in the visible range, and for near-infrared range, it is collected using a switchable gain amplified InGaAs photodetector (Thorlabs, PDA10CS-EC)[146].

The experimental equipment is fully remotely controlled by a computer-based system and data is collected with a specifically designed data acquisition program by Labview.

3.2.3 Experimental method

To evaluate the thermo-optic coefficient as a function of the temperature, a continuous optical beam at a specific wavelength was launched on the surface of the sample. The transmitted radiation intensity was monitored and recorded while the temperature of the sample slowly increased from room temperature (RT) to a temperature of about T=500K.

The transmitted signal I_t, as explained in Section 2.5.1, is the result of multiple interferences taking place inside the FP cavity, and it is given by the Airy formula:

$$I_t = \frac{I_0}{1 + \frac{4F^2}{\pi^2} \sin^2 \Phi} \tag{3.11}$$

Temperature fluctuations induce variations in both the refractive index and length of the cavity (thermal expansion coefficient). As a result, the phase of the transmitted signal exhibits a periodic trend. It is mathematically described by the formula:

$$\frac{\delta \Phi}{\delta T} = \frac{2\pi L}{\lambda} \left(\frac{\delta n}{\delta T} + \alpha(T) n(T) \right) \tag{3.12}$$

where α is the thermal expansion coefficient, λ is the wavelength, $\frac{\partial n}{\partial T}$ is the thermo-optic coefficient, n and L are the refractive index and length of the cavity, respectively.

The TOC is evaluated by monitoring the pattern of the transmitted radiation intensity during the application of the temperature ramps. Firstly, the pattern of the transmitted signal as a function of temperature is obtained by combining the collected data from the photodetector with the temperature from the PT-100 sensor. Here, the distance in temperature between two consecutive maxima (or minima) peaks, ΔT_π, which corresponds to a phase shift of the optical propagated field of $\Phi=\pi$, was extracted. According to Eq. 3.12, it was possible to evaluate the thermo-optic coefficient $\frac{\delta n}{\delta T}$.

It's worth noting that both $\alpha(T)$ and *n(T)*, which represent the thermal expansion coefficient and the refractive index, respectively, are temperature-dependent. Therefore, their values need to be updated at each temperature step. In this study, expressions from the literature are employed for the thermal expansion coefficient $\alpha(T)$, according to the relevant equations in Table 3.2. In particular, the $\alpha(T)$ dependence for GaN is the linear interpolation of the experimental data provided in Ref. [144], from 300 to 500 K. On the other hand, *n(T)* is calculated according to Eq 3.12 with the value obtained from the previous temperature step. The evaluation of the thermo-optic coefficient starts at room temperature and the value of the refractive index n(RT), as reported in Table 3.2, is extracted from the experimental data of spectroscopic ellipsometry, as described in Section 3.1.2 and Section 3.1.3.

To ensure a more accurate evaluation of the thermo-optic coefficient, once each operating temperature was reached, the system has been maintained in a stable state for approximately ten minutes before starting the measurement of transmitted optical intensity. Five consecutive and independent acquisitions of the photodetector output signal, along with the corresponding precise temperature data from the PT-100 sensor, were then averaged to obtain a single pair of measurement points (Transmitted signal, Temperature). Finally, each DUT underwent several temperature ramps, from RT to maximum temperature and, again, from maximum temperature down to RT.

3.2.4 Experimental results: 4H-SiC and GaN

The temperature dependence of the thermo-optic coefficient was evaluated for two samples of 4H-SiC and GaN. These experimental measurements were carried out at two distinct wavelengths, specifically in the visible (λ=632.8 nm) and near-infrared (λ=1550 nm) range. The temperature range extended from room temperature (RT) up to approximately T=500K. The following section shows the experimental results obtained in this study.

$\frac{\delta n}{\delta T}$ at near-infrared wavelength (λ=1550 nm)

In this section, the experimental results obtained at a wavelength λ=1550 nm are reported. It is the most common wavelength used in ***optical communications*** due to the exceptionally low absorption losses shown by silica optical fibers. Knowledge of the thermo-optic effect in this spectrum range is fundamental for telecommunication applications. The experimental results are included in a journal paper [133].

Firstly, the transmission radiation signal is collected when a temperature ramp from RT to about 500K is applied to the sample. The collected data for the 4H-SiC sample are reported in Fig 3.7. According to the above-detailed procedure, the measurement of the distance, in terms of temperature, between two consecutive maxima (or minima) of the transmitted signal, which corresponds to a phase shift of the optical propagation field of $\phi=\pi$, was estimated. It is worthwhile specifying that the amplitude drop around 400 K is due to a submicrometric shift that occurred in the mechanical assembly during the several hours-long automated acquisition. However, these events do not affect the $\partial n/\partial T$ extraction, as it only depends on the distance in temperature between two consecutive maxima or minima.

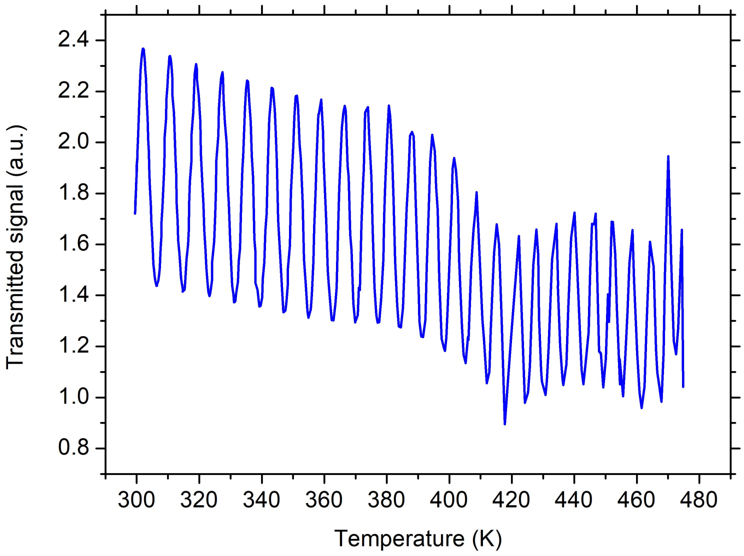

Fig. 3.7: Transmitted signal as a function of temperature for the 4H-SiC sample (λ=1550 nm).

According to the Eq. 3.12 and taking into account the recursive method for calculating of $\alpha(T)$ and $n(T)$, the $\frac{\delta n}{\delta T}$ is evaluated as a function of temperature. The experimental data for the 4H-SiC sample are depicted in Fig. 3.8 and they can be suitably described by a linear curve in the given temperature range, described by the following equation:

$$\frac{\delta n}{\delta T}(T) = 1.03 \cdot 10^{-7} T + 5.77 \cdot 10^{-6} \tag{3.13}$$

In order to evaluate the agreement grade of the experimental data $\frac{\delta n}{\delta T}$ *vs* T with the linear fitting curve $f_L(T)$, the coefficient of determination, R^2 was measured. In statistics, R^2, known as *R-square*, is a number between 0 and 1 that measures how well a statistical model predicts a result. R^2 is expressed as follows:

$$R^2 = 1 - \frac{SS_{res}}{SS_{tot}} = 1 - \frac{\sum_{i=1}^{n}(y_i - f_i)^2}{\sum_{i=1}^{n}(y_i - \bar{y}_i)^2} \tag{3.14}$$

where SS_{res} is the residual sum of squares, SS_{tot} is the total sum of squares, n is the number of the points, y_i is the observed data, f_i is the fitted data, and $\bar{y}_i$ is the mean of the observed data. In this case, the high R^2=0.9894 demonstrates the good agreement.

Another important parameter that characterizes the goodness of the polynomial approximation of the TOCs *vs* T is the root-mean-square error (*rmse*) of all of the experimental points and fL(T). It is an estimation of the accuracy of the model used to describe a data set and it is expressed as follows:

$$rmse = \sqrt{\frac{SS_{res}}{n}} = \sqrt{\frac{\sum_{i=1}^{n}(y_i - f_i)^2}{n}} \tag{3.15}$$

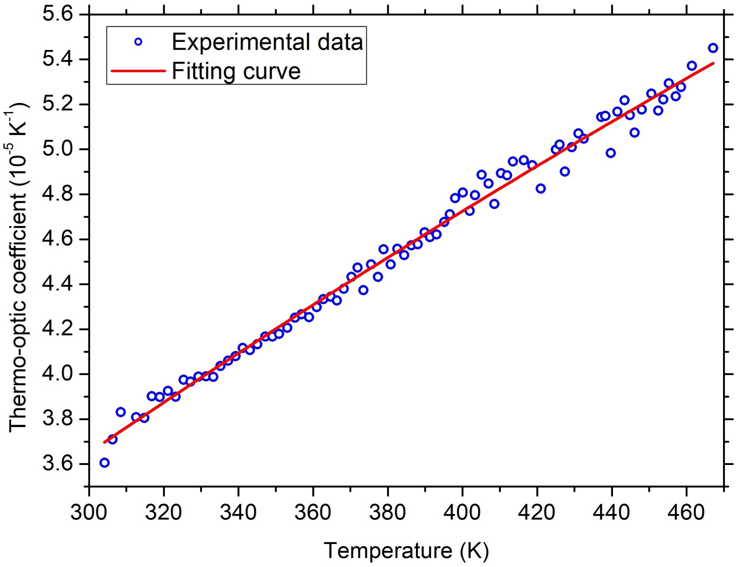

Fig. 3.8: Thermo-optic coefficient as a function of temperature for 4H-SiC sample at (λ=1550 nm).

The corresponding *rmse* value of 4H-SiC TOC, in the investigated temperature ranges, is $4.74 \cdot 10^{-7} K^{-1}$.

The same procedure was employed to evaluate the temperature-dependence of the thermo-optic coefficient for the GaN sample. As shown in Fig. 3.9, the distance in temperature between two consecutive transmission maxima (or minima) is larger than the 4H-SiC substrate due to the reduced thickness of the FP cavity (L = 0.35 mm), therefore the number of the experimental points of TOC as a function of temperature is limited to only a few values.

The experimental data, shown in Fig. 3.10, were modelled with the 2nd-order polynomial best-fits, $f_L(T)$, described by the following equations:

$$\frac{\delta n}{\delta T}(T) = -3.81 \cdot 10^{-10} T^2 + 3.45 \cdot 10^{-7} T - 2.07 \cdot 10^{-5} \tag{3.16}$$

Also in this case the high $R^2 = 0.9699$ demonstrates a good agreement between the experimental points and the polynomial fit. The corresponding *rmse* value for GaN TOCs is $3.78 \cdot 10^{-7} K^{-1}$. As observed in the case of 4H-SiC, the *rmse* value is approximately two orders of magnitude lower than the corresponding TOC values calculated using Eq. 3.13 and Eq. 3.16.

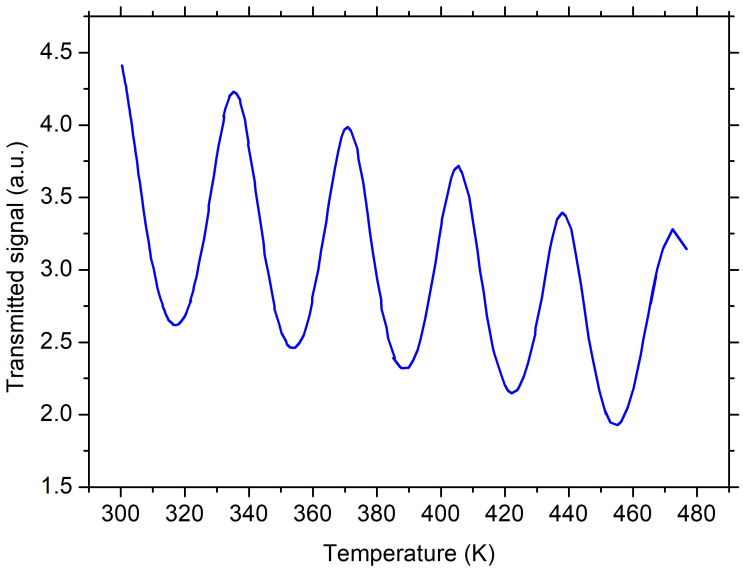

Fig. 3.9: Transmitted signal as a function of temperature for the GaN sample (λ=1550 nm).

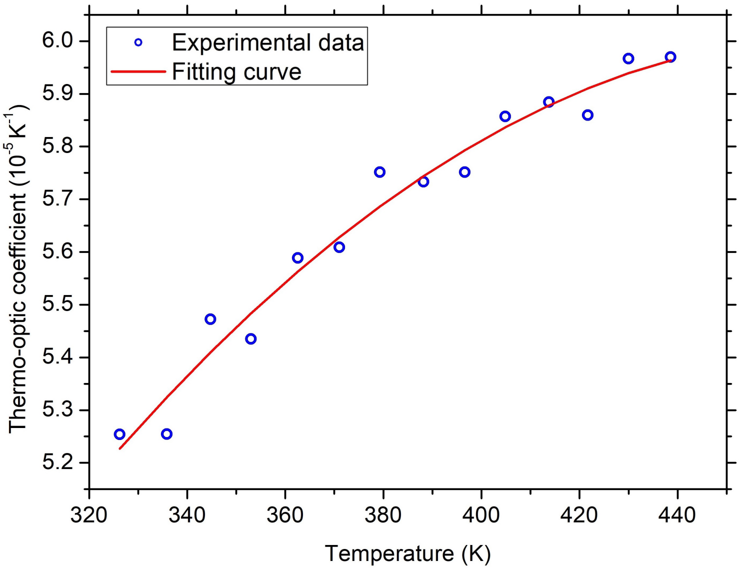

Fig. 3.10: Thermo-optic coefficient as a function of temperature for GaN sample at (λ=1550 nm).

$\frac{\delta n}{\delta T}$ at visible wavelength (λ=632.8 nm)

In the ***visible spectrum***, both 4H-SiC and GaN, as wide band-gap semiconductors, exhibit transparency. This characteristic could promote the development of novel communication or sensory applications utilizing these materials, such as biosensing, nonlinear optics, and quantum photonics. For this reason, the same analysis procedure was applied to evaluate the temperature dependence of the thermo-optic coefficient at a wavelength of $\lambda = 632.8nm$ for 4H-SiC and GaN. The experimental results are reported in two research papers [132, 134]. The temperature-dependent transmitted signal for 4H-SiC and GaN samples are shown in Fig. 3.11 and 3.12, respectively.

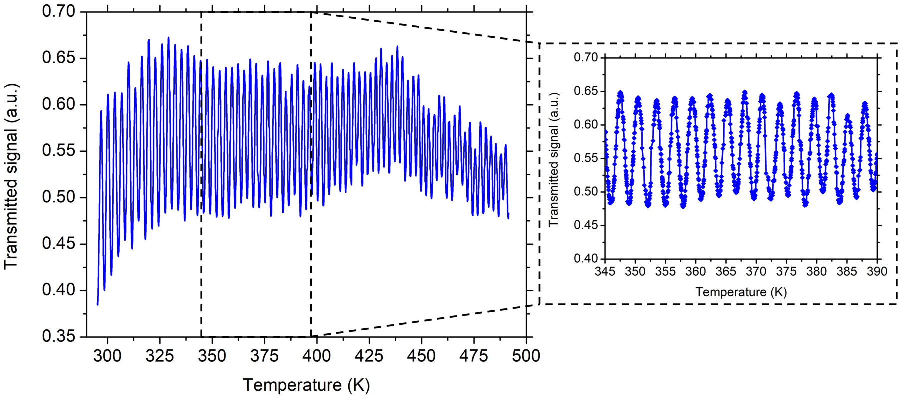

Fig. 3.11: Transmitted signal as a function of temperature for the 4H-SiC sample (λ=632.8 nm).

It is worth noting that due to the shorter wavelength of the incidental optical beam, according to the Eq. 3.12, the transmitted signal contains more periods than those obtained at λ=1550 nm within the same temperature range.

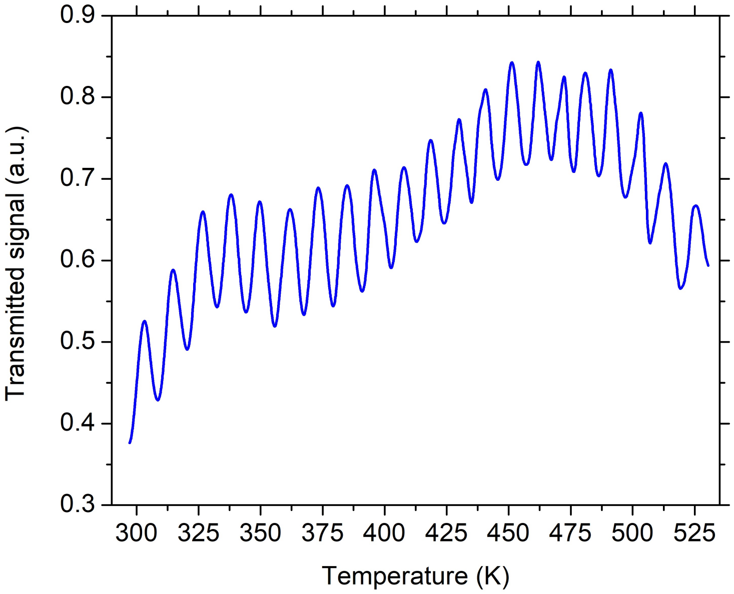

Fig. 3.12: Transmitted signal as a function of temperature for the GaN sample (λ=632.8 nm).

Similar to the analysis at λ=1550 nm, the experimental data of the $\frac{\delta n}{\delta T}$ as a function of the temperature were fitted with the first-order polynomial, $f_L(T)$ using the following equation:

$$\frac{\delta n}{\delta T}(T) = 7.68 \cdot 10^{-8} T + 1.72 \cdot 10^{-5} \quad for \quad 4H\text{-}SiC \tag{3.17}$$

$$\frac{\delta n}{\delta T}(T) = 7.21 \cdot 10^{-8} T + 4.28 \cdot 10^{-5} \quad for \quad GaN \tag{3.18}$$

The coefficient of determination, R^2, was calculated in order to assess the agreement between the experimental data $\partial n/\partial T$ vs T and the best linear fit, $f_L(T)$. Both 4H-SiC and GaN samples exhibited a high degree of linearity, with R^2 values of 0.9934 and 0.9802, respectively, as shown in Fig. 3.13 and Fig. 3.14. In addition, the *rmse* value was extracted to characterize the goodness of the linear approximation. The calculated rmse values for 4H-SiC and GaN are $2.954 \cdot 10^{-7} K^{-1}$ and $5.974 \cdot 10^{-7} K^{-1}$, respectively. These values are two orders of magnitude lower compared to the TOC values extracted from Eq. 3.17 and Eq. 3.18.

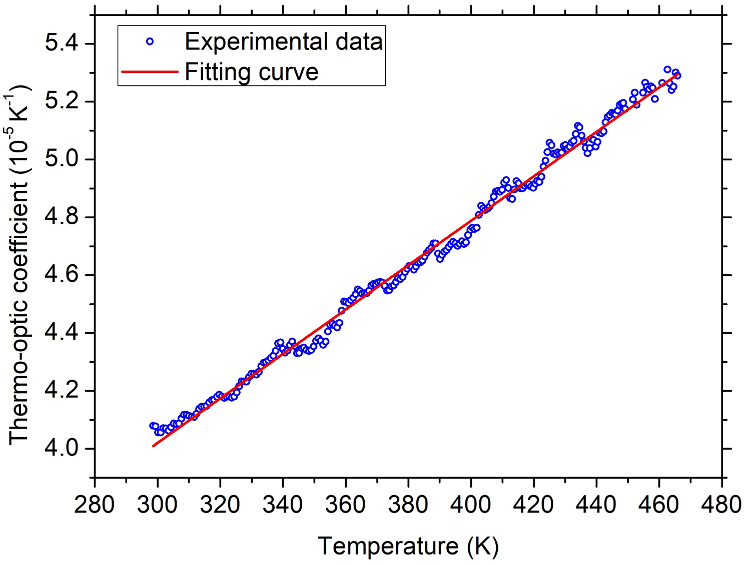

Fig. 3.13: Thermo-optic coefficient as a function of temperature for 4H-SiC sample (λ=632.8 nm).

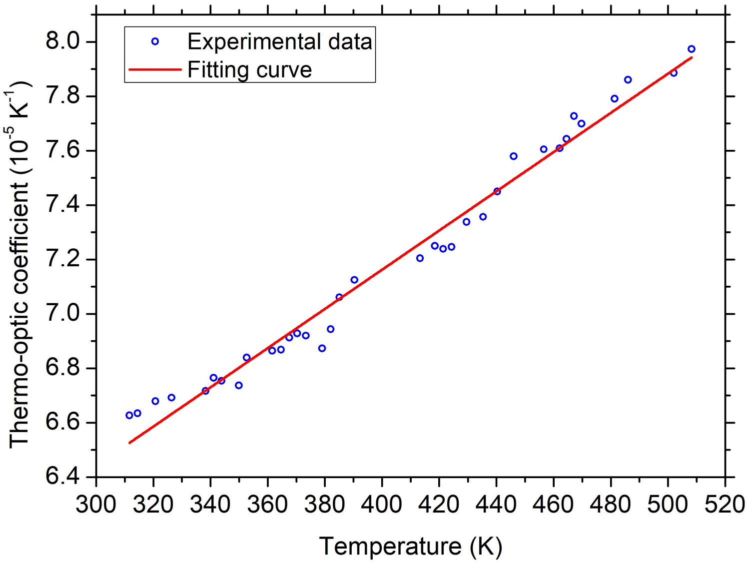

Fig. 3.14: Thermo-optic coefficient as a function of temperature for GaN sample (λ=632.8 nm).

Discussions

Table 3.3 summarizes the calculated thermo-optic coefficients for 4H-SiC and GaN at room temperature, focusing on the two wavelengths considered in this work: 632.8 nm and 1550 nm. At RT, the TOC values at 632.8 nm are slightly higher than those measured at 1550 nm for both semiconductors. However, the increase is more pronounced for the GaN sample compared to 4H-SiC.

This observation is consistent with the results reported in Ref [128] where the thermo-optic coefficients of 4H-SiC and GaN at RT across a broad spectrum of wavelengths are reported. Wherein, the experimental data clearly depicts a gradual variation in the TOC of 4H-SiC. On the contrary, $\partial n/\partial T$ for GaN exhibits a rapid increase as the wavelength decreases. This discrepancy has been attributed to the different kind of semiconductor bandgap which is direct for GaN and indirect for 4H-SiC.

λ (nm)	4H-SiC TOC ($10^{-5}K^{-1}$)	GaN TOC ($10^{-5}K^{-1}$)
632.8	4.10	6.60
1550	3.60	5.15

Table 3.3: Room Temperature thermo-optic coefficient of 4H-SiC and GaN at 632.8 nm and 1550 nm.

4

Silicon Carbide photosensors in ultraviolet, visible and near-infrared range

In this chapter a formal investigation is conducted on the optical response of photosensors based on 4H-SiC. This includes a numerical study of an optically controlled power MOSFET, where a real-time optical sensing of the junction temperature and an optical driving have been demonstrated. The experimental and numerical results of a high-performance p-i-n photodiode operated in the ultraviolet range are also reported. Additionally, photodetection in the visible and near-infrared range has been experimentally demonstrated through the fabrication and electro-optic characterization of a Schottky photodetector based on Graphene/4H-SiC.

4.1 Theoretical simulation of an optically monitored 4H-SiC Power MOSFET

Monitoring the junction temperature of power semiconductor devices is essential to evaluate their performance, reliability, and durability. Temperature has a significant impact on critical electrical parameters, and adequate thermal management is of paramount importance to prevent system failure.

In this section, a novel real-time method for the direct monitoring of the junction temperature of a SiC-based power MOSFET is introduced. As seen in Chapter 3, temperature affects the optical properties of semiconductor materials, such as SiC. Additionally, electro-optical simulations are performed to demonstrate the optical drive of the same power MOSFET. The theoretical results are included in two research papers [147, 148].

4.1.1 Optical monitoring of the junction temperature

Nowadays, wide bandgap semiconductors, such as SiC, have replaced Si counterparts in power applications, especially in power MOSFET. SiC power MOSFETs offer several advantages, including high-frequency operation and minimized switching losses, making them well-suited to meet the performance demands and frequencies of the new generation of electronic switching converters. However, during power and thermal cycling, the cumulative impact of thermal stress on these power-switching semiconductor devices, which arises from fluctuations in their junction temperature, remains one of the most common factors leading to device failure. Measuring the junction temperature of power semiconductor devices is a challenging task that has become increasingly critical as the need for higher power density in power MOSFETs continues to grow.

Consequently, a lot of examples have been successfully demonstrated in the literature regarding the development of techniques and methodologies aimed at accurately determining the junction temperature of these critical power-switching semiconductor devices. Currently, three primary approaches stand out as the most prominent for evaluating the junction temperature of power semiconductor devices. These include optical methods, physical contact methods, and electrical methods [149].

The electrical-based technique involves using electrical devices or electrical parameters to measure temperature. Examples of electrical devices include thermal-sensitive electrical devices (TSED), which require additional electronic components like resistors, diodes, and external electrical circuits for accurate temperature measurement. Electrical methods also rely on detecting thermo-sensitive electrical parameters (TSEP), including on-state resistance, on-state voltage, and turn-on delay of pulse signals [150–152], which are used for online junction temperature monitoring. However, power loss is introduced to the system, making these methods less suitable for temperature measurement during device operation. Although these methods provide excellent spatial resolution, they require high costs and add to the system's complexity [149]. Recently, a study explored the linear relationship between the body-drain voltage of power MOSFETs and junction temperature across a wide range of bias currents, from 22 $°C$ to 150 $°C$ [153].

Instead, physical contact methods involve placing a die directly in contact with a thermo-sensitive material, using thermistors and thermocouples to measure temperature variations. These methods are limited by their need for mechanical access to the die and have limited accuracy and dynamic response [154].

Recently, optical-based sensing techniques have emerged as a non-invasive and prominent solution of junction temperature monitoring, immune to electromagnetic interference [149]. These techniques rely on detecting the optical properties of the semiconductor, which exhibit temperature-dependent behaviors, or on acquiring a thermal image of the semiconductor die via an infrared camera. These techniques can achieve high accuracy and generate a thermal map of the semiconductor die, facilitating the identification of temperature maxima and the temperature gradient across the die. Various indirect approaches for measuring T_J using optical solutions have been proposed, including those based on electroluminescence, light spectrum, Raman spectroscopy, and liquid crystal thermography [155–158].

In the following section, a novel real-time optical junction temperature monitoring, relying on the evaluation of the optical response of a Fabry-Perot cavity integrated into a power MOSFET, is presented.

4.1.2 Device concept

The structure of an optically-controlled power MOSFET is in many aspects comparable to a traditional MOSFET. The proposed device structure is a vertical diffusion MOSFET (VDMOS) and its cross-section is shown in Fig. 4.1. It illustrates the vertical configuration of the device: notably, the source electrode is positioned above the drain, which directs the current predominantly in a vertical direction when the transistor is in the on-state. The structure consists of several distinct regions as described below.

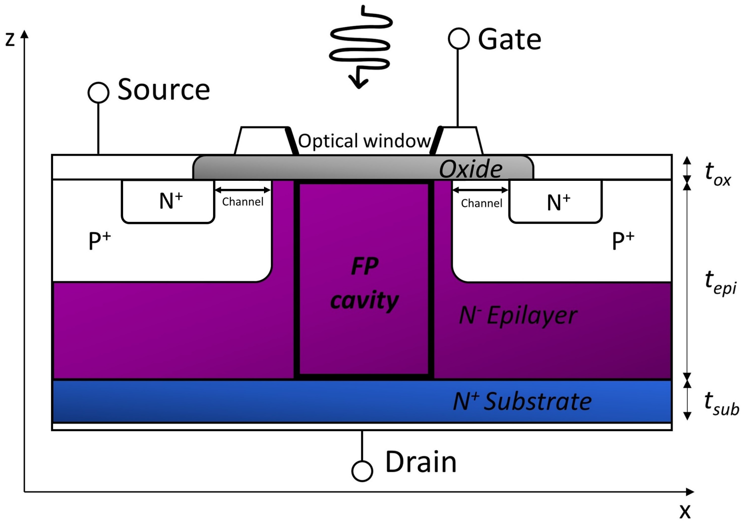

Fig. 4.1: Schematic cross-section of an optically-driven 4H-SiC Power Mosfet. The MOSFET-integrated FP cavity consists of the 4H-SiC epilayer between the SiO_2 gate-oxide and the 4H-SiC heavily-doped substrate.

There is an n-type region heavily doped with nitrogen ($10^{19} cm^{-3}$) that forms the drain of the MOSFET, with a drain contact defined below it. Above this region, a lightly doped n-type layer, typically with a doping concentration in the range of 10^{15} cm^{-3}, is epitaxially grown. Subsequently, two aluminum-doped p-type regions are established, containing the actual MOS structure, including the device channel with a length of 1 μm. The final SiC regions are the phosphorus-doped n-type regions, defining the source regions, with metal contacts placed on top to serve as the source contacts. An 80 nm thick SiO_2 layer forms the insulating layer of the MOSFET, and subsequently, a metal contact is placed above it, which forms the gate contact. The key geometric and physical properties are detailed in Table 4.1.

Parameters	Value
Silicon oxide thickness, t_{ox} (μm)	0.08
Source thickness, t_{N^+} (μm)	0.50
Substrate thickness, t_{sub} (μm)	100.00
Channel length, L_{ch} (μm)	1.00
Base junction depth, t_{base} (μm)	1.30
Base-to-base distance, W_j (μm)	10
Epilayer thickness, t_{epi} (μm)	10
Base-to-substrate distance, $t_{epi'}$ (μm)	0.5
N^+-source doping (cm^{-3})	10^{18}
P-base doping (cm^{-3})	10^{17}
N^--epilayer doping (cm^{-3})	10^{16}
N^+-substrate doping (cm^{-3})	10^{19}

Table 4.1: Geometric and physical parameters of power MOSFET based on 4H-SiC.

Based on this device structure, optical driving power MOSFET has been demonstrated. This was enabled by integrating an optical window within the gate electrode. Through this optical window, an optical beam, composed of two wavelengths, one in the transparency and one in the absorption region of the semiconductor, is launched into the upper surface of the device. This configuration allows, at the same time, the real-time optical monitoring of the junction temperature and the optical driving of the same device.

Regarding the junction temperature monitoring, the transmitted signal from a Fabry-Perot cavity, which is integrated into the MOSFET, is evaluated. It consists of the lightly-doped epilayer sandwiched between the silicon oxide and the heavily doped 4H-SiC substrate. The simulation results on the interferometric output of the MOSFET-integrated Fabry-Perot cavity show that the variations of the junction temperature can be determined by monitoring the fringe patterns. The latter are caused by the temperature-induced variations in the refractive index of the 4H-SiC lightly-doped n-type epilayer region. On the other hand, the optical-driving is achieved by employing an optical beam with a wavelength in the absorption region which enables the electron channel formation.

4.1.3 Optical simulation: junction temperature monitoring

The optical simulations were performed using the RSoft BeamPROP simulation software package. As explained in Section 2.7.2, BeamPROP relies on the finite difference beam propagation method (BPM), a widely employed and well-established technique for modeling field propagation in integrated photonic devices. The simulations took into account the structure of the MOSFET-integrated Fabry Perot cavity. As shown in Fig. 4.1, the device is defined in the <x,z> plane where <z> is the optical propagation direction. Then, the structure implemented in RSoft was simplified to the vertical structure composed of a silicon oxide layer, a lightly-doped 4H-SiC epilayer, and a heavily-doped 4H-SiC substrate.

The optical beam at a wavelength of $\lambda = 450nm$ was launched on the top of the gate-oxide layer. Within the structure, multiple beam interferences occurred due to reflections at the interfaces of the epilayer/substrate and oxide/epilayer. These interferences arose from slight differences in refractive index between the layers. In the case of epilayer/substrate, the primary reason for this refractive index contrast is the significant difference in their doping concentrations. The 4H-SiC epilayer typically has a doping concentration of $N_D \approx 10^{16}\ cm^{-3}$, while the 4H-SiC substrate exhibits a nitrogen doping concentration ranging from $10^{18}\ cm^{-3}$ to $10^{19}\ cm^{-3}$.

It's worth noting that at the considered wavelength, $\lambda = 450nm$, 4H-SiC exhibits transparency. Consequently, no excess carriers are generated, which means that the electrical conductivity and the drain current remain unaffected by the probing optical signal employed for temperature monitoring.

The transmitted optical signal was monitored and collected at the input of the FP cavity, specifically at the surface of the SiO_2 layer. Firstly, a parametric simulation spanning a wavelength of around 450 nm was performed.

Fig. 4.2 illustrates the simulated FP reflected spectrum centered around the wavelength of interest. The corresponding calculated Free Spectral Range (FSR), which represents the optical wavelength spacing between two consecutive maxima or minima of optical intensity reflected by the FP interferometer, is FSR=3.62 nm. It is consistent with the theoretical value that can be derived from the following equation:

$$FSR = \frac{\lambda^2}{2nL} = 3.70nm \tag{4.1}$$

As explained in Section 3.2.1, temperature variations, resulting from environmental and/or operating conditions, have a notable impact on a Fabry-Perot cavity. These temperature variations induce a change both in the refractive index of the cavity and its physical length. As a result, a shift in the phase of the transmitted signal is induced.

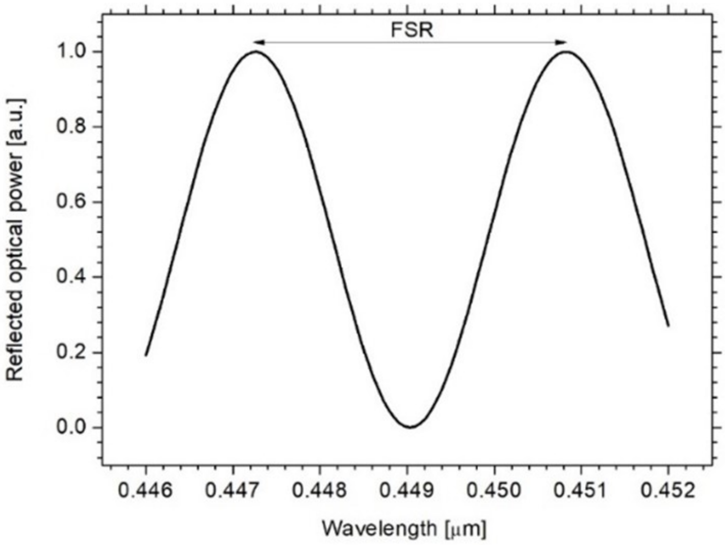

Fig. 4.2: The normalized reflected output power as a function of wavelength.

To investigate this phenomenon, a parametric simulation was performed by varying the refractive index of the epilayer over a range that allowed for the gradual and complete detuning of the cavity. To evaluate the impact of these variations, a monitor was placed at the gate-oxide output, enabling the assessment of the reflected optical power. Fig. 4.3 shows the normalized reflected optical power as a function of the epilayer refractive index highlighting the transition from the maximum to the minimum of the reflected signal.

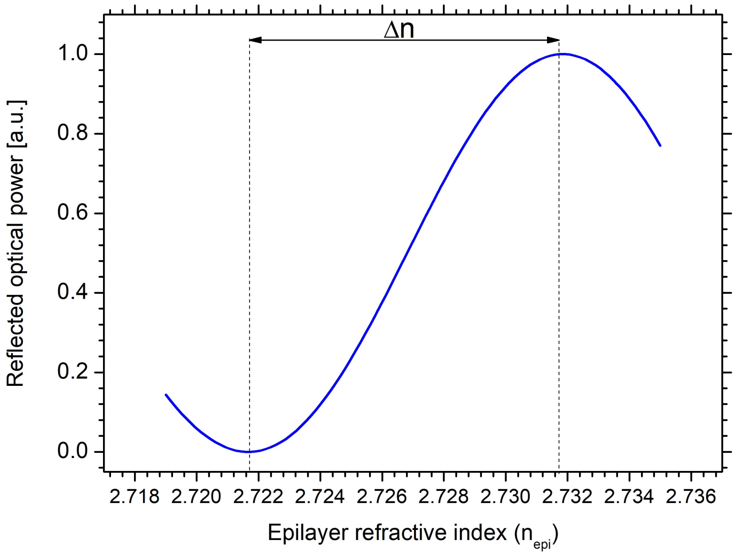

Fig. 4.3: Reflected output power *vs* epilayer refractive index.

A complete detuning of the FP cavity occurs in the 10-μm-thick 4H-SiC epitaxial layer when the refractive index change reaches $9.65 \cdot 10^{-5}$. Assuming a thermo-optic coefficient of $7.8 \cdot 10^{-5} K^{-1}$ for 4H-SiC at 450 nm [128], in turn, it is necessary a temperature variation of $\Delta T_{\pi/2} = 123.7°C$ to achieve a thermally-induced refractive index change of $9.65 \cdot 10^{-5}$. Therefore, the results show that, by monitoring the fringe pattern of the MOSFET-integrated Fabry Perot cavity, it is possible to detect a temperature variation of $\Delta T_{\pi/2} = 123.7°C$, value that can provide information on the status of the device[148].

In addition, the impact of the gate oxide thickness on the optical output of the cavity was investigated through a parametric simulation. The study involved monitoring temperature variations while varying the gate-oxide thickness from 50 nm to 500 nm. The results, depicted in Figure 4.4, demonstrate that the temperature variation is independent of the gate-oxide thickness. The selected value of 100 nm aligns with the typical thickness of commercial power MOSFET.

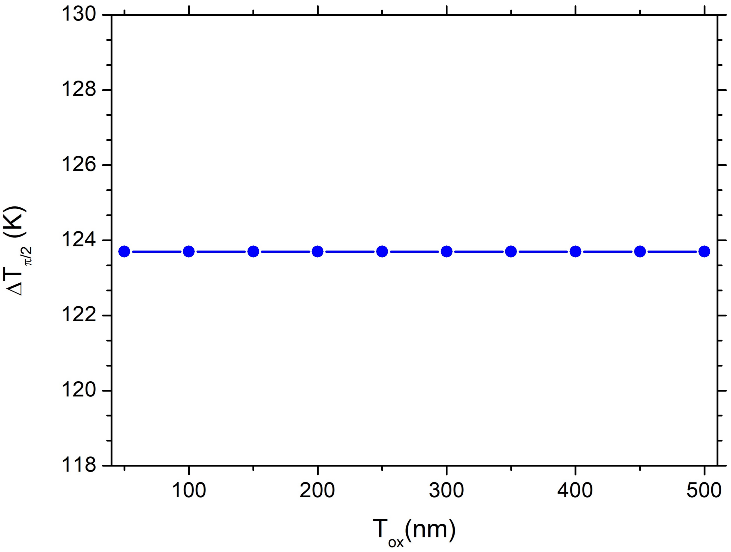

Fig. 4.4: Temperature variation induced by a complete detuning of the MOSFET-integrated Fabry Perot cavity as a function of the gate-oxide thickness.

4.1.4 Electro-Optic simulation: activation of power Mosfet

Numerical simulations were conducted to demonstrate the optical driving of the 4H-SiC-based power MOSFET. The electro-optic simulations were carried out using Atlas, a physics-based numerical simulator produced by Silvaco. The simulation process began with the design of a 2D cross-section of the 4H-SiC MOSFET elementary half-cell, as shown in Fig. 4.5. Its modeling was performed using DevEdit, a tool integrated into Atlas. The device structure was fine-meshed wherever appropriate and in particular where a high gradient of doping levels was observed [159]. It was especially around the p-n junctions and within the channel region, just below the 4H-SiC/SiO2 interface. The mesh density is of crucial significance since an insufficient density can lead to convergence issues in simulations. Notably, the vertical spacing towards the substrate was relatively less dense.

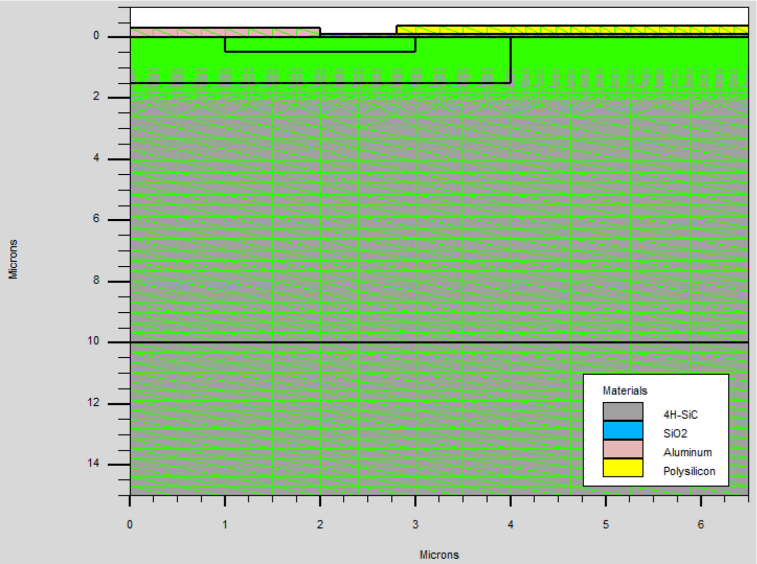

Fig. 4.5: A cross-section of the simulated 4H-SiC power MOSFET half-cell showcasing the finite element mesh where the equations are solved at each node. Note the high mesh density near the junctions.

The elementary half-cell structure consists of seven regions, each defined as previously described. The key parameters associated with these regions are concisely presented in Table 4.1. The device has a length (x-direction) of 6.5 μm and a width (z-direction) of $1 \mu m$ by default. Therefore, the drain contact area is 6.5 μm^2, the source contact area is 1.8 μm^2 and the gate contact area is 3.4 μm^2.

The key physical models taken into account include the mobility and carrier lifetimes depending on doping concentration and temperature. Additionally, the models include incomplete doping ionization, apparent bandgap narrowing, impact ionization, Shockley-Read-Hall, and Auger recombination. Detailed descriptions of these models were previously provided in Section 2.7.1, while the comprehensive model parameters are thoughtfully summarized in Table 4.2.

The numerical simulations were conducted by integrating the LUMINOUS optoelectronic tool to investigate the carrier photogeneration phenomenon in the MOSFET channel. Particularly, optoelectronic simulations involve the evaluation of the photogeneration rate at each mesh point through two correlated calculations per-

Parameters	**Value**
$\mu_{0_{p,n}}^{max}(cm^2/Vs)$	950,125
$\mu_{0_{p,n}}^{min}(cm^2/Vs)$	40,15.9
$N^{crit}(cm^{-3})$	$2\cdot10^{17}$,$1.76\cdot10^{19}$
$\alpha_{n,p}$	-0.5
$\beta_{n,p}$	-2.4,-2.15
$\delta_{n,p}$=-$\gamma_{n,p}$	0.76,0.34
E_A (meV)	200
E_D (meV)	100
$\tau 0_{n,p}$ (ns)	15
$N^{SRH}(cm^{-3})$	$5\cdot10^{16}$
$C_{n,p}$	$5\cdot10^{-31}$,$2\cdot10^{-31}$

Table 4.2: Model parameters used in the electro-optic simulation of 4H-SiC optically-driven power Mosfet.

formed simultaneously. The initial calculation relies on the real part of the refractive index to compute optical intensity at each grid point along the optical path. In parallel, the second calculation employs the imaginary refractive index to analyze absorption and photogeneration phenomena occurring at these same points. This coordinated approach allows for a comprehensive assessment of the device's optoelectronic behavior.

The aim is to drive the 4H-SiC power MOSFET by generating an electron channel through photogenerated carriers. For this purpose, an optical beam in the ultraviolet range, in which 4H-SiC exhibits the maximum optical absorption, was injected into the gate electrode which includes an optically transparent window placed above the MOSFET channel. In the case of a fully optically-driven power MOSFET, a significant quantity of optical power is required. To address this limitation and, consequently, to facilitate the turn-on process, a sub-threshold gate voltage was continuously applied. The value of the threshold gate voltage, previously determined for these devices, has been evaluated at $V_T = 8V$ according to Ref. [159]. In order to maintain the device in a cutoff state during simulations, a subthreshold gate voltage of $V_G = 5V$ was chosen. Under these conditions, no electron channel is formed, and consequently, no current flows between the drain and source contacts even with an applied drain-source voltage (V_{DS}).

The investigation of power MOSFET activation under a UV optical beam involved the extraction of the MOSFET characteristics, specifically the drain current density vs. drain-source voltage ($J_D - V_{DS}$). Firstly, the $J_D - V_{DS}$ MOSFET characteristics were compared under different wavelengths within the UV range. This analysis aimed to determine the most effective optical beam wavelength for inducing photogeneration phenomena with the 4H-SiC MOSFET channel. This analysis revealed that $\lambda = 285nm$ is the optimal wavelength. This value maximizes the optical response of 4H-SiC and enables the efficient generation of high currents at low optical power densities.

The $J_D - V_{DS}$ characteristics were examined under dark conditions and under an optical beam at wavelength $\lambda = 285nm$. The optical power was varied across a range up to $10kW/cm^2$ while a sub-threshold gate voltage was fixed at $V_G = 5V$. These characteristics are graphically depicted in Fig. 4.6. Additionally, within the same figure, the $J_D - V_{DS}$ characteristics in dark conditions with gate bias of $V_{GS} = 5V$ and $V_{GS} = V_T = 8V$ are presented. Here, it's shown that MOSFET remains in the off-state for $V_{GS} = 5V$ while it begins conducting at $V_{GS} = 8V$ which represents its threshold voltage. It's worth noting that these values of optical power are consistent with those that can be reached in an optical fiber. Specifically, the power density of 10kW/cm^2 is obtained in a single-mode optical fiber, whose diameter is typically 8 μm, in which an optical power of 5mW propagates.

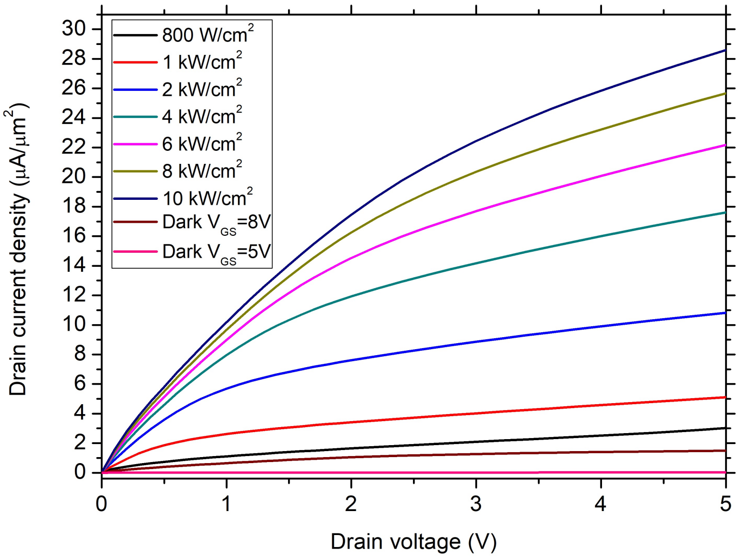

Fig. 4.6: Forward $J_{DS} - V_{DS}$ output characteristics at dark condition with $V_{GS} = 5V$ and $V_{GS} = 8V$ and under UV beam at 285 nm with seven different values of optical power density when a sub-threshold gate voltage $V_{GS} = 5V$ is applied.

At a specific working point within the saturation region, specifically with a drain-source voltage (V_{DS}) of 4 V and an incident optical power density of 4 kW/cm^2, the resulting drain current density amounts to approximately 16 $\mu A/\mu m^2$. This, in turn, leads to an ON-state resistance of 250 $k\Omega\mu m^2$. This value closely aligns with the typical characteristics of commercial power devices.

4.2 Ultraviolet 4H-SiC *p-i-n* Photodiode: Experimental Characterization and Simulation-based Interpretation

4.2.1 Device structure

The ultraviolet *p-i-n* 4H-SiC photodiode was processed by the Institute of Microelectronics and Microsystems (CNR-IMM) of Bologna (Italy). A schematic cross-section is shown in Fig. 4.7.

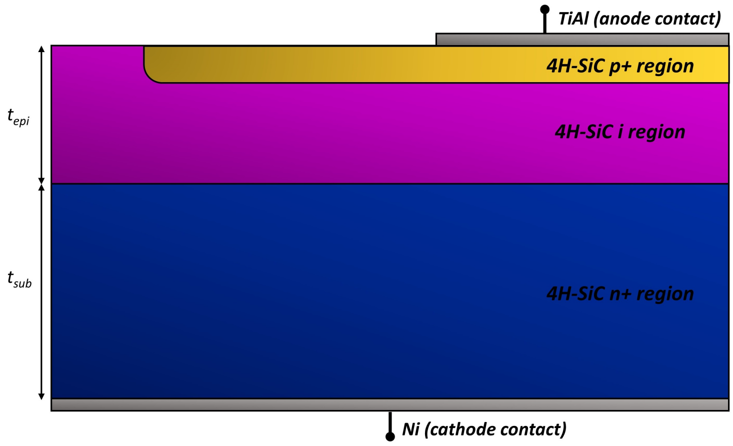

Fig. 4.7: Schematic cross-section of a half cell of 4H-SiC *p-i-n* photodiode.

The device was manufactured on a commercially available <0001> 8° off-axis, 300 μm-thick, highly-doped n-type 4H-SiC wafer. The substrate has a doping concentration of N_D=5·$10^{19}cm^{-3}$ and it is the starting layer of the proposed *p-i-n* structure. On this substrate, an epitaxial layer of 16.5 μm-thick slightly doped (n-type, $N_D = 10^{15}cm^{-3}$) 4H-SiC was grown. To realize the top p^+ region, that is the anode region with a circular area of 9.62·$10^{-4}cm^2$ (diameter of 350 μm), an ionic implantation of aluminum (Al) was performed. The Al-implanted doping concentration profile was measured by the Secondary Ion Mass Spectroscopy (SIMS) and the results are shown in Fig. 4.8. At the surface, the Al-implanted concentration is $7 \cdot 10^{19}cm^{-3}$ with a profile edge located at 2 μm. The concentration gradually decreases and reaches the constant epilayer doping (*i*-region) at about 1.35 μm from the surface of the anode contact. Finally, the upper concentric Ti/Al anode contact, with a circular area of 2.41 ·$10^{-4}cm^2$ was formed, along with the Ni cathode contact. These contact regions were defined by photolithography and lift-off processes on the p^+ implanted region and the n^+ back surface of the wafer, respectively. The main geometric and physical parameters are summarized in Table 4.3.

	p^+	n^-	n^+
Doping (cm^{-3})	$7 \cdot 10^{19}$ (peak)	$3 \cdot 10^{15}$	$5 \cdot 10^{19}$
Thickness (μm)	See profile in Fig. 4.8	16.5	300.0

Table 4.3: Physical parameters of 4H-SiC *p*-*i*-*n* layers.

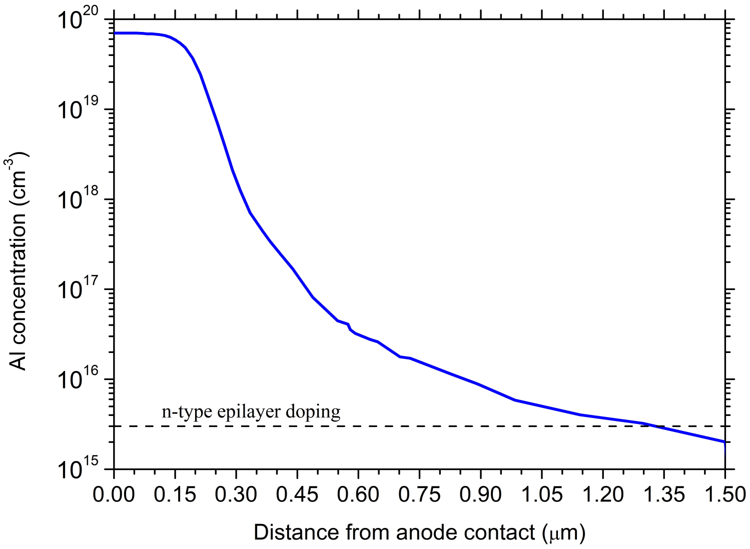

Fig. 4.8: Secondary ion mass spectrometry (SIMS) profile of the Al-implanted doping concentration in p^+ layer of *p*-*i*-*n* photodiode.

4.2.2 Experimental results

In order to investigate the electro-optical performance of the *p*-*i*-*n* photodetector the experimental setup, shown in Fig. 4.9, was employed. This setup consists of a probe station (MPS150) equipped with a semiconductor parameter analyzer (AGILENT 4155C), used to trace the device's experimental characteristics, and a UV monochromator that applies the radiation to DUT.

By considering an active area of $7.21 \cdot 10^{-4} cm^{-2}$, the current density-voltage (J-V) characteristics at room temperature and under dark conditions were evaluated [160]. The experimental results in forward voltage bias, ranging from 0 V to 3 V, and in reverse bias up to 30V are reported in Fig. 4.10 and in Fig. 4.11, respectively. Both plots show a typical trend compared to those reported in the literature for

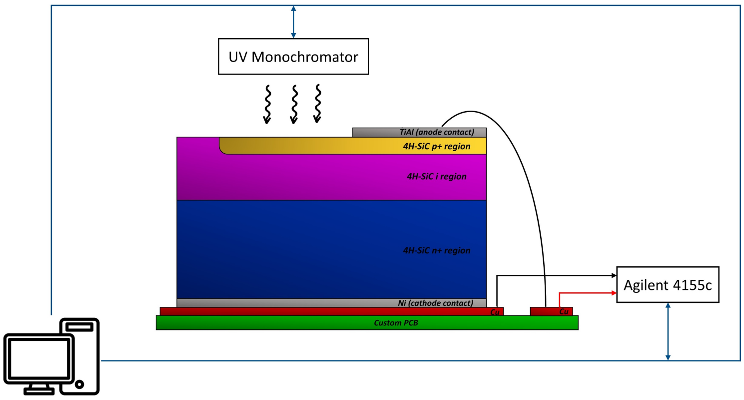

Fig. 4.9: Schematic experimental setup and fabricated microchip bonded on a custom PCB for a stable remotely controlled measurement.

similar devices. Regarding the forward bias analysis, it was possible to extract the electrical parameters, specifically the series resistance (R_S) and ideality factor (η). By fitting the analytic diode equation, the extracted values of R_S and η are 489 Ω and 1.8, respectively. While, under reverse bias conditions, the current density gradually increases with increasing voltage bias, ranging from -5 V to -30 V. Notably, at -5 V and -30 V, the current densities reach 22.3 and 78.6 nA/cm^2, respectively.

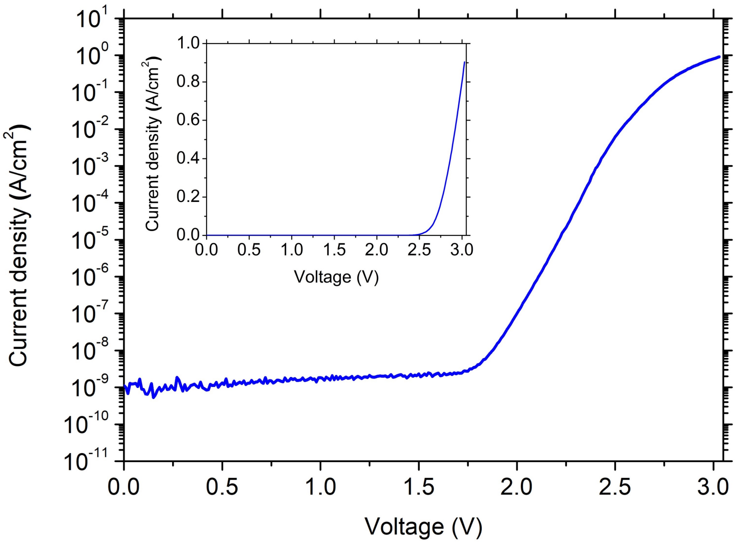

Fig. 4.10: Current density as a function of the forward voltage from 0 to 3V at RT in dark conditions in semilogarithmic scale. The insert reports the experimental data in linear scale.

In order to evaluate the optical response of the *p-i-n* photodiode in the ultraviolet range, an optical beam from a Xenon lamp was dispersed through a remotely controlled UV monochromator and focused onto the photoactive area of the device.

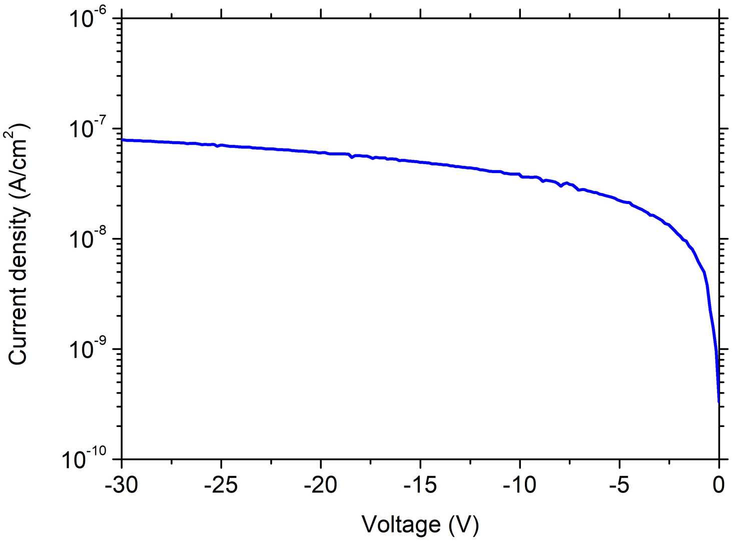

Fig. 4.11: Current density as a function of the reverse voltage up to -30V at RT and under the dark condition in semilogarithmic scale.

The J-V characteristics were monitored at room temperature under UV incident light with wavelength in the range from 210 nm to 380 nm, by step of 5 nm. The obtained J-V characteristics in reverse bias at different wavelengths are depicted in Fig. 4.12. It is observed that the current density increases with longer wavelengths, and the diode characteristic shifts upwards. It should be noted that the photogenerated current density increases until the wavelength reaches 315 nm. As shown in the zoomed view in Fig. 4.12, for wavelengths longer than 315 nm, the current density decreases. So, the maximum photo-generated current is obtained at λ=315 nm.

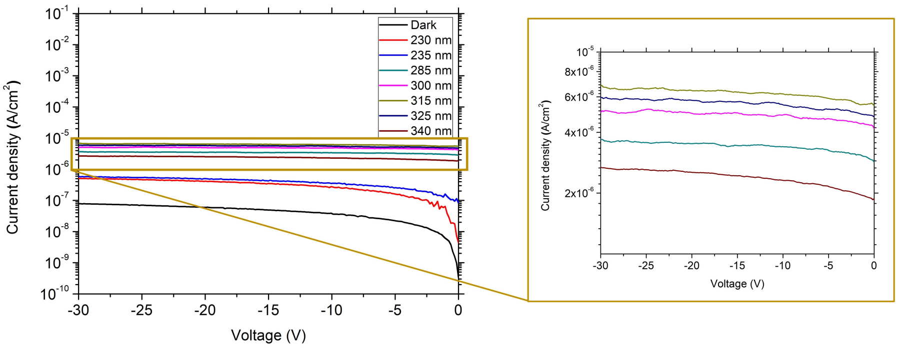

Fig. 4.12: Current density as a function of the reverse voltage up to -30V at RT for different UV wavelengths.

This trend is confirmed in Fig. 4.13 in which the photogenerated current as a function of the UV radiation wavelength at zero-bias and 30V-reverse bias is depicted. As anticipated, in both cases, the photogenerated current density exhibits a peak at λ=315 nm. It should be noted that this wavelength doesn't correspond to the peak response wavelength of the photodetector. In fact, it also relies on wavelength-dependent incident optical power. For this reason, a full characterization of the monochromator was performed in order to calculate the optical power spectrum in the same range. The incidental optical power was monitored by replacing the DUT with a commercial photodiode (DET 210) with a known active area and fully characterized responsivity, R(λ), at all wavelengths. The measured optical incident optical power density is reported in Fig. 4.14.

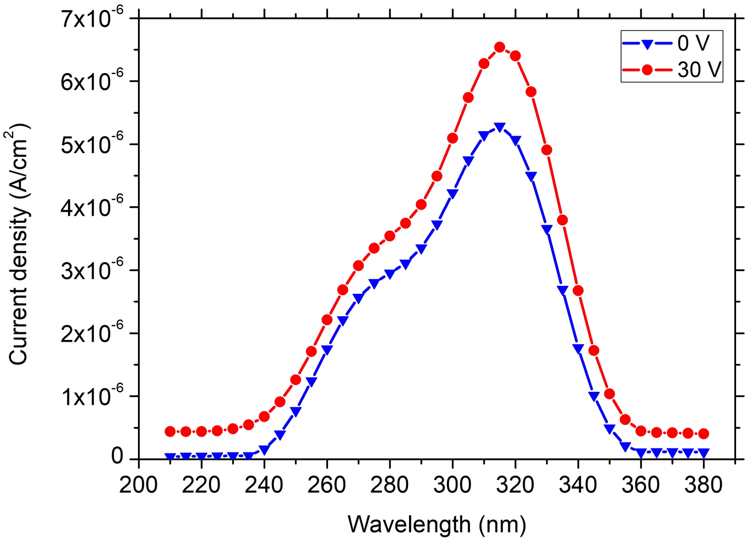

Fig. 4.13: Photo-generated current density *vs.* ultraviolet wavelength without bias (blue line) and at reverse voltage V=-30 V (red line).

As previously explained in Section 2.5.2, a related figure of merit of photodetectors is the spectral responsivity, defined as the ratio between the photogenerated current (I_{ph}) and the incidental optical power (P_{inc}):

$$R = \frac{I_{ph}}{P_{inc}} \tag{4.2}$$

Moreover, the spectral responsivity is related to the external quantum efficiency (EQE), the number of charge carriers collected per incident photon, by the following expression:

$$\eta = R\frac{h\nu}{e} \tag{4.3}$$

where $h\nu$ is the photon energy and e is the elementary charge.

The spectral responsivity curve at zero-bias in the UV range (from 210 nm to 380 nm) is reported in Fig. 4.15. In the same plot, the relative quantum efficiency is

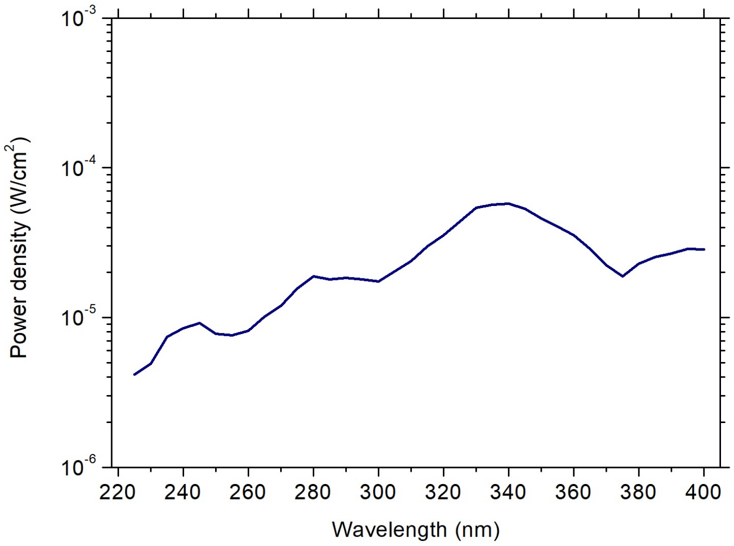

Fig. 4.14: Incident optical power density as a function of wavelength.

evaluated. The measured responsivity is 0.168 A/W at a wavelength λ=285 nm and the relative external quantum efficiency is 72.7%.

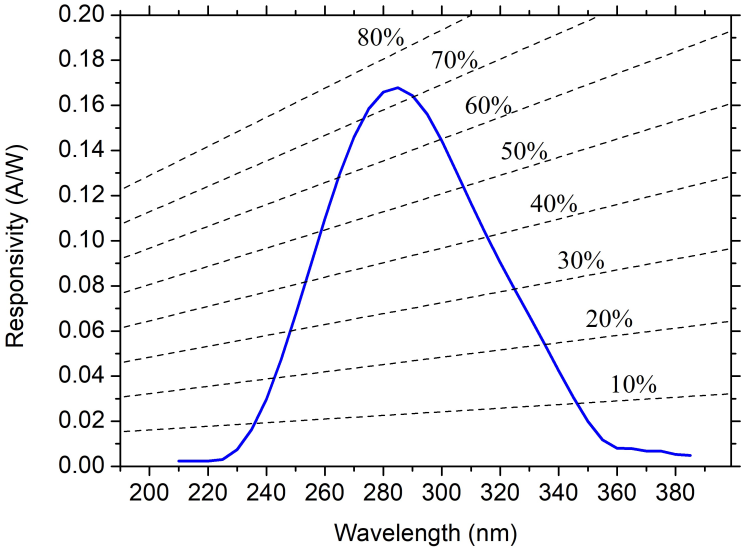

Fig. 4.15: Responsivity and quantum efficiency at zero-bias of the 4H-SiC *p*-*i*-*n* photodetector as a function of wavelength.

Fig. 4.16 shows how the responsivity and the quantum efficiency, evaluated at peak wavelength, change with the applied reverse voltage. A slight increment is observed as the reverse voltage increases. This phenomenon is attributed to the widening of the depletion region which enhances the collection efficiency and the separation mechanism of photogenerated carriers, consequently [161].

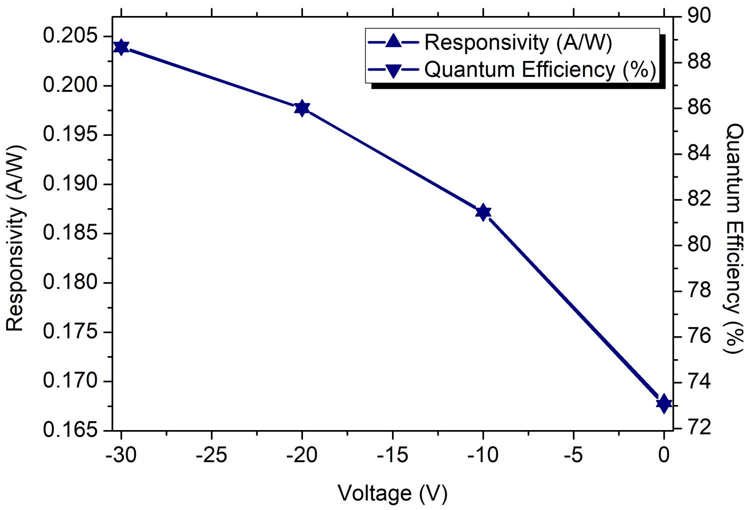

Fig. 4.16: Responsivity and corresponding quantum efficiency at peak response wavelength as a function of the reverse bias voltage.

Additionally, the electro-optic performance of the 4H-SiC *p*-*i*-*n* photodetector was investigated at different incidence angles of light. The photo-generated current was monitored when the photodiode was illuminated with UV radiation at a wavelength of λ=285 nm without bias. The results, depicted in Fig. 4.17, show the measurement obtained as the viewing angle of the incident light changes in a range between -45° to +45°, in the steps of 5°.

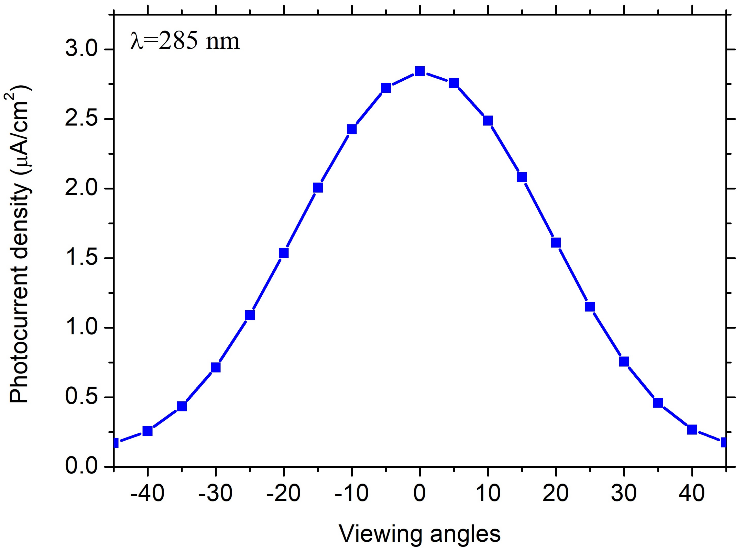

Fig. 4.17: Photogenerated current density at varying viewing angles between -45° to +45°.

It's evident that the optical response is at its peak when the incident radiation is normal to the photodiode surface. Conversely, as the viewing angle deviates from normal, whether increased or decreased, the photogenerated current exhibits a notable reduction.

To our knowledge, the calculated responsivity peak of 0.168 A/W at the wavelength of 285 nm, is the best value reported in the literature for UV photodiodes. A comparison between different structures, such as Schottky, p-i-n, and avalanches UV photodiodes, reported in the literature to date, is shown in Table 4.4

4.2.3 Electro-optic simulation

The above-described *p-i-n* photodiode, complete with its geometric parameters and doping levels, was imported into a physic-based device simulator, Atlas by Silvaco. The working principle of Silvaco Atlas is described in Section 2.7.1.

The initial step involved the construction of the device structure using the Devedit tool within Atlas. Here, the photodiode's geometry and doping profiles, as outlined earlier, were imported into the simulation environment. These key parameters are summarized in Table 4.5.

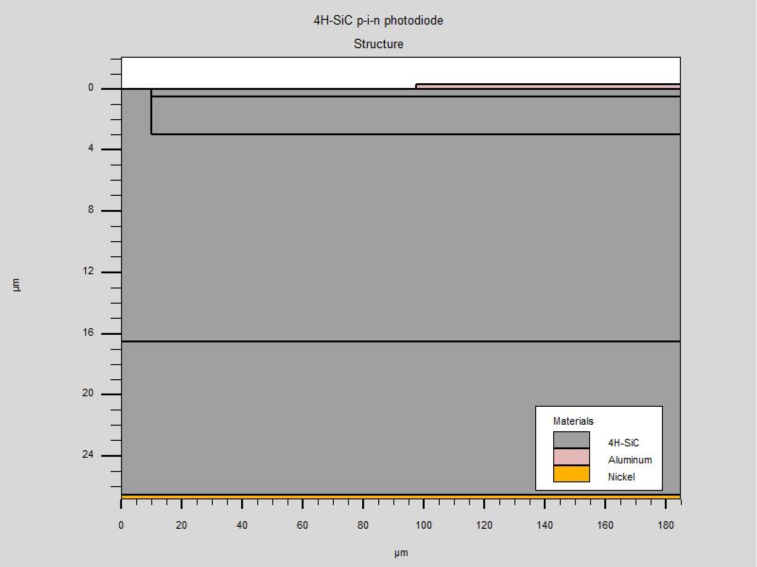

Fig. 4.18: Structure of 4H-SiC p-i-n photodiode in Silvato Atlas.

The resulting structure, shown in Fig. 4.18, consists of three regions and two metal contacts.

- a heavily n-doped region, characterized by an arsenic impurity concentration of $10^{10} cm^{-3}$ which corresponds to the cathode region. As reported in Table 4.5, its thickness could be 300 μm, however in this simulation it was significantly

Material	4H-SiC (*our*)	6H-SiC[162]	4H-SiC[88]	4H-SiC[163]	4H-SiC [164]	4H-SiC [165]	4H-SiC [89]	4H-SiC[166]
Structure	p-i-n	p-i-n	p-i-n	Schottky	Schottky	APD gain=1	p-i-n	APD gain=1
Peak responsivity (A/W)	0.168	0.175	0.13	0.16	0.0852	0.144	0.13	0.099
Wavelength at peak (nm)	285	260	270	255	290	265	266	278
Maximum EQE(%)	72.7%	80%	61%	78%	37%	67%	60%	44%
Reverse polarization	0V	0V	5V	20V	10V	-	0V	-

Table 4.4: Responsivity and Q.E. comparison for Schottky, p-i-n, and avalanche UV photodiodes reported in the literature to date.

	p^+	n^-	n^+
Doping (cm^{-3})	$7 \cdot 10^{19}$ (peak)	$3 \cdot 10^{15}$	$5 \cdot 10^{19}$
Thickness (μm)	See profile in Fig. 4.8	16.5	300.0
Bandgap energy (eV)	3.26	3.26	3.26
Saturated velocity (cm^2/s)	$2 \cdot 10^7$	$2 \cdot 10^7$	$2 \cdot 10^7$
Dielectric constant	9.66	9.66	9.66

Table 4.5: 4H-SiC *p*-*i*-*n* layers' physical parameters.

reduced to $10\mu m$. This allowed to obtain significant computational advantages by reducing the number of nodes in the simulation mesh without compromising result accuracy;

- a lightly n-doped region that defines the intrinsic layer;
- a heavily p-doped region with boron impurities which corresponds to the anode region.

Finally, two metallic contacts are defined, an anode contact based on Titanium with an area of 175 μm^2 and a back contact, a cathode contact, in Nickel with an area of 370 μm^2. The 3D simulation of the half cell as shown in Fig. 4.7 was performed. Regarding the dimension of the cell, a length of 185 μm (x-direction) and a 1 μm width (z-direction) were set up. In order to obtain the right numerical results, the mesh is denser near a junction.

The above-described structure was simulated by three-dimensional modeling and simulation processes taking into account the charge transport and generation recombination mechanism. For this purpose, the standard drift-diffusion transport equations are coupled with Shockley-Read-Hall, Auger, and optical generation-recombination models. In addition, the physical models take into account the mobility and the carrier lifetime as a function of the doping concentration and temperature, apparent bandgap narrowing, incomplete ionization of dopants, and impact ionization. These models were employed as described in Section 2.7.

The simulation involved a careful tuning of the physical properties of the materials in the numerical model for the purpose of improving agreement between experimental and simulated results. The fundamental 4H-SiC parameters, assumed at room temperature, were extracted from the good agreement between theoretical and experimental results, and they are summarized in Table 4.6. It should be noted that these values are consistent with other values reported in the literature [167–170].

In order to investigate the spectral response of the p-i-n photodiode, the optical properties of 4H-SiC were defined. Especially, the complex refractive index, $\hat{n} = n + ik$, is responsible for the photodiode spectral response. The value in the ultraviolet

Parameter	Electron	Hole
$E_g(eV)$	3.26	3.26
v(cm^2/s)	$2 \cdot 10^7$	$2 \cdot 10^7$
μ_0^{max} (cm^2/Vs)	950	125
μ_0^{min} (cm^2/Vs)	40	15.9
N^{crit} (cm^{-3})	$2 \cdot 10^{17}$	$2 \cdot 10^{17}$
α	-0.5	-0.5
β	-2.15	-2.15
$\delta = -\gamma$	0.76	0.76
τ_0 (ns)	15	15
N^{SRH} (cm^{-3})	$7 \cdot 10^{16}$	$7 \cdot 10^{16}$
C	$5 \cdot 10^{-31}$	$3 \cdot 10^{-31}$

Table 4.6: Simulation model parameters assumed at room temperature.

spectrum range is monitored. Regarding the real refractive index, an ellipsometric analysis was performed in samples of 4H-SiC with a doping concentration similar to our intrinsic (i) p-i-n epilayer. The experimental data illustrate the wavelength-dependent real part of the refractive index (n), as presented in Fig. 4.19, which was incorporated into our numerical model for wavelengths up to 410 nm.

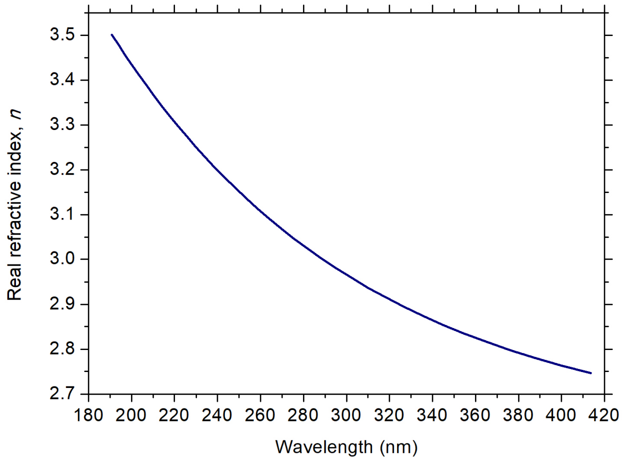

Fig. 4.19: Real refractive index as a function of the wavelength in ultraviolet spectrum range up to 420 nm of an intrinsic 4H-SiC sample.

On the other hand, the imaginary part of the refractive index, which directly impacts light absorption within the medium, was determined by exploiting a model developed through the experimental data of the dielectric function by Zollner in

[171]. The latter was evaluated in a wide spectrum of wavelengths, as depicted in Fig. 4.20. To evaluate the accuracy of the developed model, the data were compared with the imaginary refractive index suggested by Sridhara in [172] obtaining a good agreement.

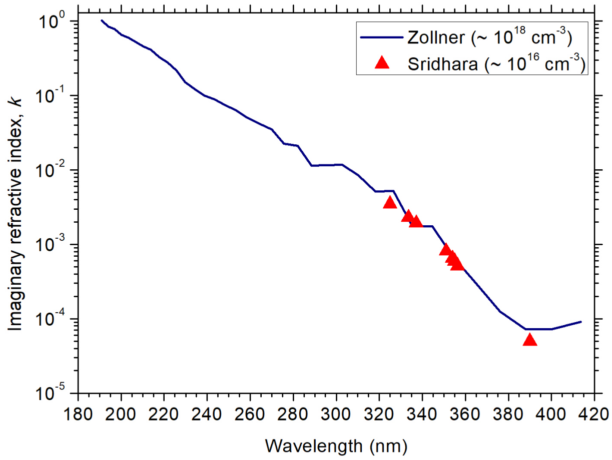

Fig. 4.20: Intrinsic 4H-SiC imaginary refractive index as a function of the wavelength up to 420 nm.

Simulations results

The simulated spectral responsivity of the 4H-SiC p-i-n photodiode was evaluated across a voltage range from 0V to 60V, with increments of 10 V, in a wavelength range from 190 to 400 nm [173]. As depicted in Fig. 4.21, the responsivity peak exhibits a significant increase with the applied reverse voltage. Particularly, it is observed that the resposivity increases significantly up to 20V, and tends to saturate as biases exceed 30V. This trend is due to the increment of the depletion region width, in full agreement with the expected trend. To validate these numerical results, they were compared with the experimental data extended up to 60V, as reported in Table 4.7.

It is worth noting that the responsivity curves exhibit a widening on the right side. This is attributed to the increased penetration depth of photons with longer wavelengths in SiC. This implies a more pronounced impact of the reverse bias on the responsivity at longer wavelengths [83, 174]. In addition, a slight shift of the responsivity peak towards longer wavelengths (red-shift) occurs as the reverse bias increases. This phenomenon should be attributed to a progressive expansion of the depletion region. The same behaviors were observed in the experimental results.

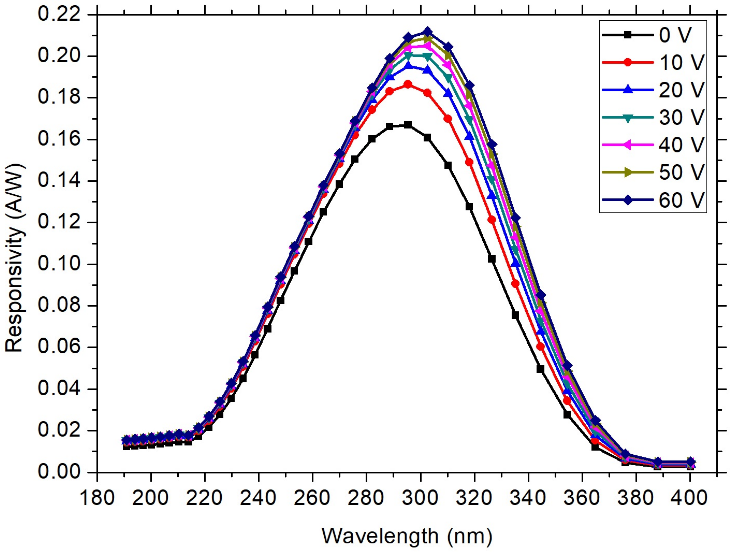

Fig. 4.21: Simulated results of the spectral responsivity of 4H-SiC UV p-i-n photodiode under different reverse biases, 0V to 60V.

Reverse bias	Responsivity Peak (A/W)		EQE (%) at responsivity peak	
	Experiments	Simulations	Experiments	Simulations
0V	0.168	0.168	72.7	70.8
10V	0.187	0.186	81.1	78.5
20V	0.198	0.195	85.6	81.7
30V	0.204	0.201	88.3	83.9
40V	0.205	0.205	89.0	85.1
50V	0.209	0.209	90.6	86.7
60V	0.212	0.212	91.8	87.9

Table 4.7: Responsivity peak and relative external quantum efficiency for experimental and simulated results measured under a voltage bias up to 60V.

The electron concentrations (cm^{-3}) were probed under an ultraviolet optical beam to mainly investigate the depletion region width modified by reverse bias. Fig 4.22 shows the numerical results of the electron concentration depth profiles evaluated at the center of the active area of the p-i-n photodiode along <y> direction for zero-bias, 20 V, 40V, and 60V. Here, the optical beam wavelength corresponds to the value at the responsivity peak.

As expected, the depletion region expands with the increasing reverse voltage. The relative expansion as a function of the reverse bias up to 60V is shown in Fig. 4.23. In Fig. 4.24, a comparison between the simulated and experimental data of the responsivities at zero bias and reverse bias of 20V, 40V, and 60V is depicted.

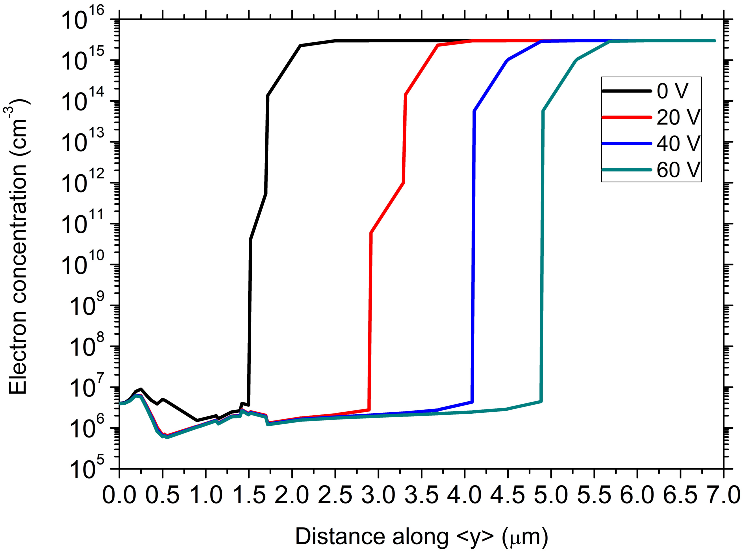

Fig. 4.22: Simulated electron concentration profile along the vertical <y> direction of the 4H-SiC photodiode under different reverse biases from 0V to 60 V at the responsivity peak wavelength.

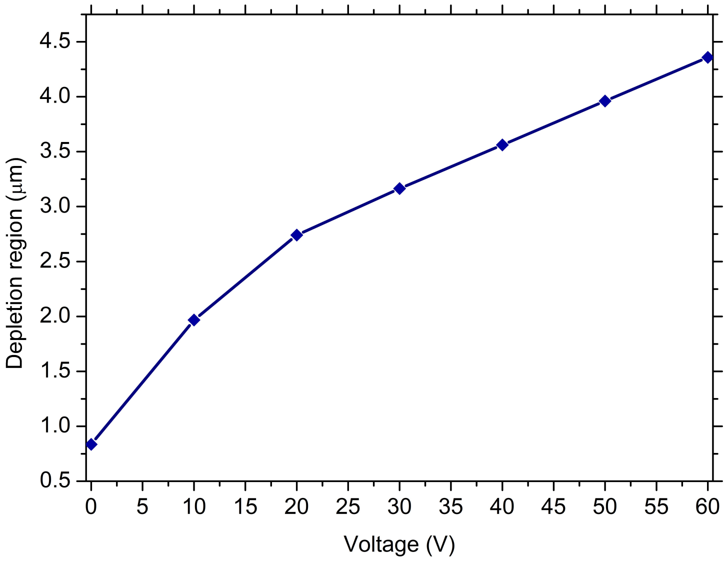

Fig. 4.23: Depletion region width when the p-i-n is illuminated with an optical beam at the responsivity peak wavelength as a function of the reverse bias.

The developed numerical model provides electro-optic results which match very well the experimental data with the theoretical ones. This agreement attests to the accuracy and reliability of these simulations. The numerical model could be a valuable instrument for an in-depth understanding of the physical processes within a 4H-SiC-based device. Furthermore, it enables reliable predictions of the behavior of next-generation devices. Simulations with properly calibrated parameters are in-

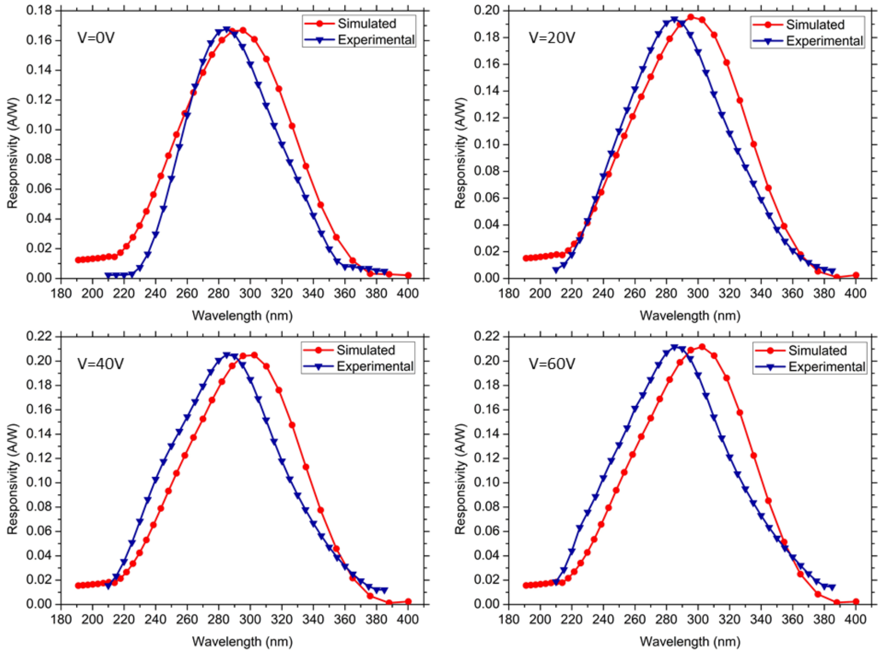

Fig. 4.24: Experimental and simulated responsivity of the 4H-SiC p-i-n photodiode at 0V, and reverse bias of 20V, 40V, and 60V.

deed invaluable for predictive parametric analysis of novel and more intricate device structures.

The *ad-hoc* numerical model was also employed for the purpose of designing an optimized structure. The optimization process is described in the following section.

Optimization of photodiode structure: geometrical and physical parameter

To enhance the device's performance, an investigation was carried out to evaluate the impact of physical and geometrical parameters on its optical response.

It's important to note that all the ensuing results and simulations concern zero-bias measurements.

The first step in efficiency optimization involved the selection of the optimum doping concentration of the intrinsic layer of the p-i-n photodiode. The doping concentration was reduced from $3 \cdot 10^{15} cm^{-3}$ to $3 \cdot 10^{14} cm^{-3}$ and subsequently to $1 \cdot 10^{14} cm^{-3}$. As illustrated in Fig. 4.25, a lower doping concentration in the intrinsic layer leads to an enhancement in responsivity. This phenomenon can be attributed to the expansion of the depletion region as doping concentration decreases. Within this region, the amount of photons with longer wavelengths, that are absorbed in-depth, increases. This leads to the additional generation of electron-hole pairs which contribute to the photocurrent and consequently to an enhancement in the optical response. As the depletion region width triples in thickness, both the peak responsivity and the relative quantum efficiency increase by approximately 20% and 17%, respectively.

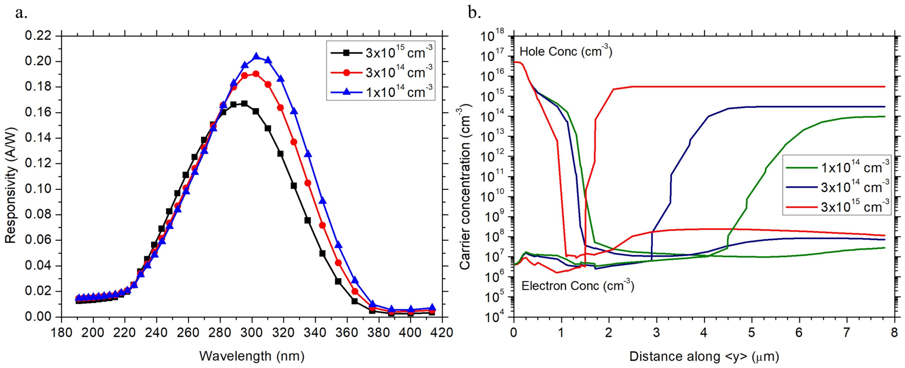

Fig. 4.25: Simulated responsivity (a), electron and hole concentration along the vertical <y> direction of the p-i-n photodiode (b) with the distinct value of the doping concentration of n- layer.

Reducing the doping concentration in the epitaxial layer leads to an increased optical response, which is a favorable outcome for enhancing the device's performance. However, it's crucial to acknowledge that achieving lower doping levels in the epitaxial layer presents a more significant technological challenge as it demands a higher level of purity and precision in the fabrication process. Various doping profiles for the anode region were examined, and it was observed that no substantial impact on the optical response has been detected [175].

The investigation of the effect of the hole lifetime on the device's optical response was carried out. Fig. 4.26 shows the dependence of responsivity on the hole lifetime. Photons with lower energy levels, which are absorbed deeper outside the depletion region, tend to generate electron-hole pairs that are more susceptible to recombination. An increase in the hole lifetime leads to a decrease in the recombination rate, and consequently, a larger amount of electrons reach the depletion region and the cathode contact. As a result, the optical response improves. It's worth noting that a slight shift in the peak of responsivity towards longer wavelengths (red-shift) occurs.

A further optimization process is related to geometric parameters, specifically the extension of the lateral region of the n-layer exposed to UV light and its thickness. In Fig. 4.27a, the responsivity is depicted for varying lateral region sizes ranging from 10 μm to 60 μm. The optimal value is 20 μm, corresponding to a responsivity of 0.169 A/W.

Furthermore, the impact of the n-layer thickness (t_{epi}) on the optical response was also investigated, with thickness variations ranging from 4 μm to 16.5 μm. In

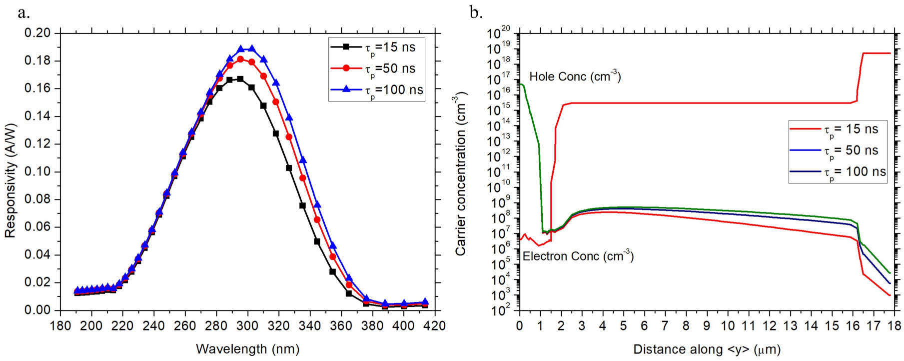

Fig. 4.26: Simulated responsivity (a), electron and hole concentration along the vertical <y> direction (b) of the p-i-n 4H-SiC photodiode with distinct value of hole lifetime.

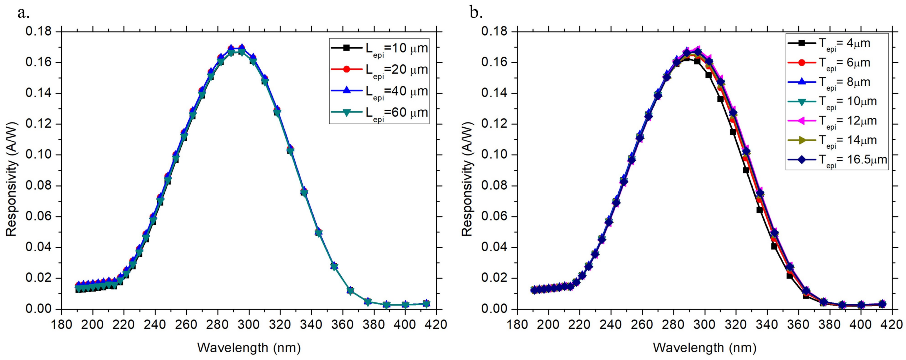

Fig. 4.27: Simulated responsivity varying geometrical parameters: length (a) and thickness (b) of the lateral region of n-layer exposed to UV light.

this case, as depicted in Fig. 4.27b, no significant variations in optical responsivity were observed for thicknesses exceeding 8 μm. As a result, to facilitate the development of a more compact device, the optimal n-layer thickness was established as 8 μm.

In summary, the optimal values obtained from the above-described simulations are listed in Table 4.8. As depicted in Fig. 4.28, when all these effects are considered, the performance of the 4H-SiC UV photodiode exhibits a substantial enhancement. Notably, the optical responsivity reaches 0.220 A/W at 303.4 nm, and the relative quantum efficiency at the peak response wavelength achieves an impressive value of 90.1 % at zero bias. Therefore, the results show an improvement in the performance of the 4H-SiC p-i-n photodiode. In particular, the responsivity and quantum efficiency enhance to 31% and 27%, respectively.

Parameter	Optimum value
Doping concentration (n-layer)	$1 \cdot 10^{14} cm^{-3}$
Hole lifetime	50 ns
L_{epi}	20 μm
t_{epi}	8 μm

Table 4.8: Model parameters achieved by means optimization process.

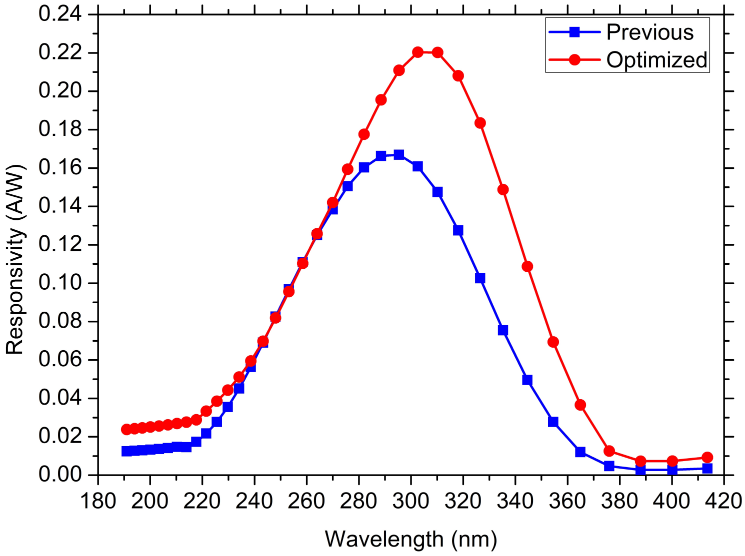

Fig. 4.28: Simulated responsivity of 4H-SiC p-i-n photodiode obtained by the optimization process.

4.3 Graphene/4H-SiC Schottky Photodetector in visible and near-infrared range

As demonstrated in the previous section, 4H-SiC is an excellent candidate for ultraviolet (UV) detection in high-temperature and high-power environments. However, it's important to note that the bandgap of SiC, approximately 3.2 eV, limits its capability to detect photons with wavelengths exceeding 380 nm. To overcome this constraint and extend its detection into the visible and near-infrared spectrum, alternative device structures need to be explored. In this research, a promising approach has been employed, involving the implementation of sub-bandgap photodetection exploiting the internal photoemission effect (IPE) within a Schottky junction by integrating a single layer of graphene (SLG) on a 4H-SiC substrate. The theory of the IPE effect was previously explained in Section 2.5.2. The experimental results are included in two research papers [176, 177].

In the forthcoming section, a Schottky photodetector, based on 4H-SiC and graphene, which enables a broadband photodetection up to the near-infrared range, is presented.

4.3.1 Device concept

The schematic cross-section of the proposed Schottky photodetector based on SLG/4H-SiC is illustrated in Fig. 4.29a. When an optical beam is launched into the upper surface of the device, specifically into the circular active area of the device (Schottky junction SLG/4H-SiC), incident photons are absorbed by SLG. Subsequently, photoexcited carriers in the conduction band, with enough energy to overcome the Schottky barrier, are emitted into the 4H-SiC substrate. Once the carriers reach the 4H-SiC substrate they are rapidly swept towards the depletion region by the electric field and then collected in the semiconductor metallic contact. This flux of carriers contributes to the photogenerated current. Therefore, this mechanism allows the detection of photons with energy between the Schottky barrier and semiconductor energy gap ($\Phi_B < h\nu < E_g$). The described photodetection mechanism is illustrated in Fig 4.29b. The main geometric parameters of the proposed SLG/4H-SiC photodetector are summarized in Table 4.9.

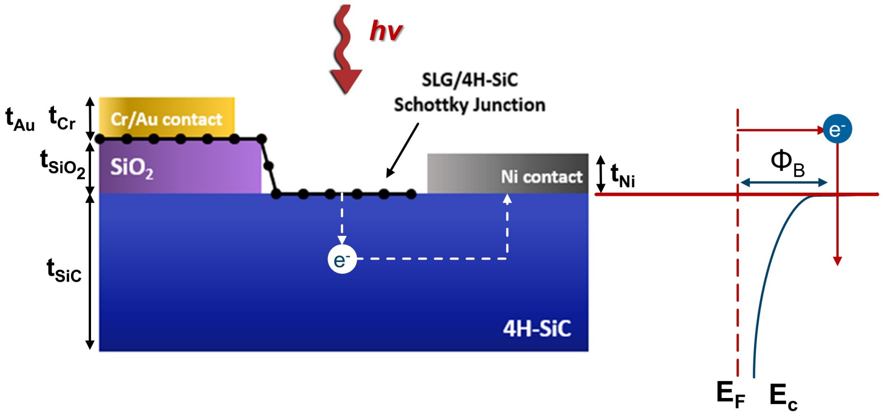

Fig. 4.29: Schematic cross-section of Schottky photodetector based on SLG/4H-SiC.

Parameters	Value
4H-SiC substrate thickness, t_{SiC} (μm)	250
Silicon oxide thickness, t_{SiO_2} (nm)	200
Nickel thickness, t_{Ni} (nm)	200
Chromium thickness, t_{Cr} (nm)	5
Gold thickness, t_{Au} (nm)	50
Circular active area (μm^2)	$7.85 \cdot 10^3$

Table 4.9: Geometrical parameters of 4H-SiC/SLG Schottky photodetectors.

4.3.2 Fabrication process

The Schottky photodetector based on Graphene/4H-SiC was fabricated at the CNR - Institute of Applied Sciences and Intelligent Systems (CNR-ISASI) of Naples (Italy). The fabrication process, which is described here, was carried out by myself.

The SLG/4H-SiC Schottky photodetectors were fabricated starting from a Si-face, highly-doped ($N_D \approx 10^{18} cm^{-3}$, n-type, Nitrogen doped), 250 μm-thick 4H-SiC substrate. The fabrication process includes eight main steps, schematically illustrated in Fig. 4.30. To begin, a standard RCA cleaning process on the 4H-SiC substrate was carried out (a). A 200 mm-thick SiO_2 layer was uniformly deposited by the sputtering process on the top of the substrate, working as an insulating layer (b). Then, the shape of the ohmic contact with the 4H-SiC substrate was defined via a bilayer photolithography process. At first, a PMGI photoresist and then a positive photoresist were spun onto the wafer, and then the optical lithography using a mask aligner was performed. After exposure, a developer was used to develop the exposed photoresist. Then, the exposed SiO_2 was etched by oxide wet etching in buffered HF solution (buffered oxide etching, BOE) (c). Subsequently, without removing the photoresist, a 200 nm-thick Nickel layer was deposited via thermal evaporation, followed by a lift-off process and rapid thermal annealing (RTA) in N_2 ambient at 950°C for 2 min in order to obtain a not-rectifying behavior (d). The nature of the ohmic contact was validated by measuring the I-V characteristics among Ni contacts of adjacent devices, and their linear behavior was confirmed. The realization of the Schottky contact involves patterning a 100 μm diameter circle followed by the BOE etching in order to expose the 4H-SiC substrate (e). The sample was then prepared for the graphene deposition.

A single layer of graphene (SLG) grown by chemical vapor deposition (CVD) was coated with a 500 nm thick poly(methyl methacrylate) (PMMA) film. This SLG/PMMA stack was placed on a polymer substrate and immersed in deionized (DI) water, allowing the SLG/PMMA film to detach and float on the water surface. Subsequently, the floating SLG/PMMA film was lifted by the substrate, and after drying, the sample was heated up and placed in acetone to remove the protective PMMA layer (f). The pattern of graphene was defined by a photolithography process, succeeded by dry etching in an oxygen plasma, which leads to the removal of the excess graphene layer. Finally, the metal electrode on graphene was lithographically patterned, and a stack of Chronium (5 nm) and Gold (50 nm) was deposited by thermal evaporation following a lift-off process.

The optical microscope image of the fabricated Schottky photodetector is depicted in Fig. 4.31. Here the SLG boundaries are highlighted by a red dashed line.

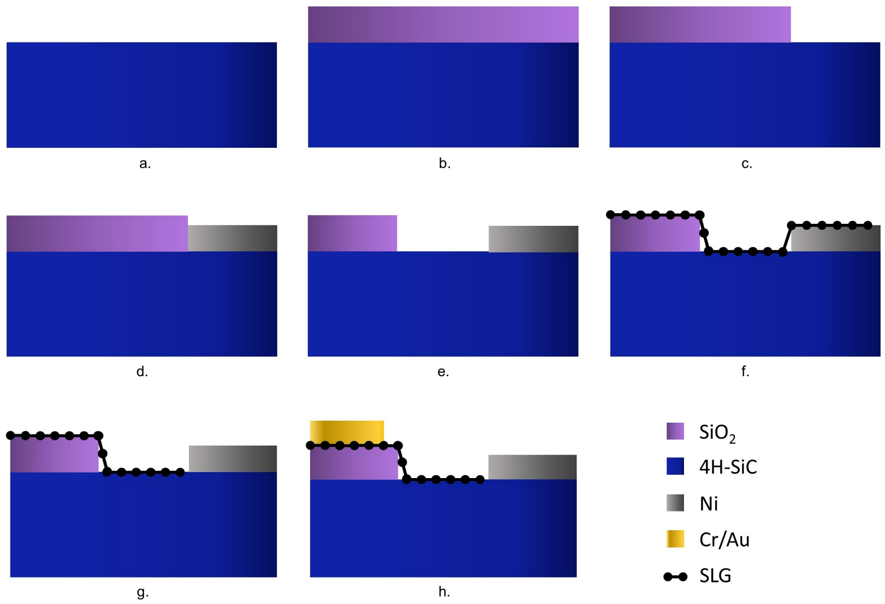

Fig. 4.30: The fabrication process of SLG/4H-SiC Schottky photodetector. RCA cleaning on 4H-SiC substrate (a), sputtering deposition of SiO_2 (b), 4H-SiC ohmic contact shape definition by a photolithography process and buffer oxide etching (BOE) (c), Nickel deposition by thermal evaporation (d), pattern of the active area (Schottky contact) by photolithography process and BOE (e), deposition of SLG by fishing procedure (f), the pattern of the SLG shape by photolithography (g), SLG contact area definition and Cr/Au deposition by thermal evaporation (h).

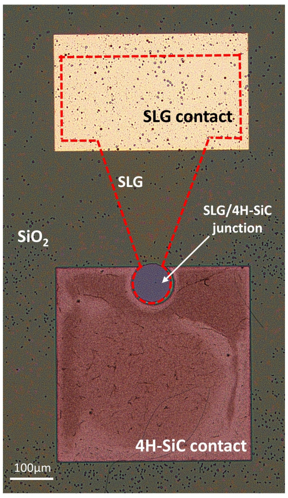

Fig. 4.31: Optical microscope image of the fabricated device. The red dashed line represents the boundary of the graphene layer.

4.3.3 Material characterization: Raman analysis

Raman spectroscopy, a non-destructive technique used for material characterization, offers a means to evaluate both stress and doping in graphene. Raman spectra were performed by a HORIBA Scientific LabRAM HR Evolution Raman spectrometer with an integrated Olympus BX41 microscope. The Raman spectrum of a freestanding graphene sheet, which is almost strain and doping-free, is characterized by the presence of a G band at 1580 cm^{-1} and a 2D band at 2700 cm^{-1} for an excitation energy of 2.33 eV. However, the concurrent presence of stress [178, 179] and doping [180] results in a shift in the position of the G and 2D peaks. By constructing a correlation map between the G and 2D peak positions, it is possible to obtain information on the simultaneous presence of stress and doping and to separate their contributions [181].

Fig. 4.33 shows the Raman spectra which were evaluated by focusing on various points within the sample, which correspond to two stacks: graphene-SiO_2-4H-SiC and graphene-4H-SiC. Here the 2D peak and G peak are highlighted.

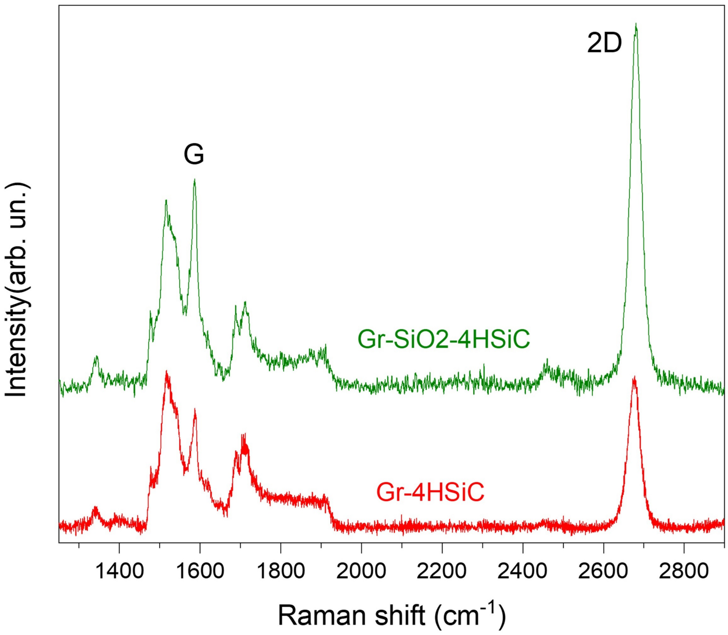

Fig. 4.32: Raman spectra of graphene on silicon oxide (green spectrum) and graphene deposited on 4H-SiC (red spectrum).

In Fig. 4.33 the correlation map between the Raman shift of the 2D peak, Pos(2D), and the Raman shift of the G peak, Pos(G), is shown. The point placed at 1582 cm^{-1} and 2670 cm^{-1} (black dot in the map) corresponds to the Raman shift of ideal graphene, with no stress and doping; from this point, two reference lines are plotted, with slope 2.45 [178, 179] and 0.07 [180] which indicate pure strain and pure doping, respectively. On the other hand, the dashed lines represent the condition of the studied sample. It's worth noting that both points show the error bars which are correlated to the different measurement points.

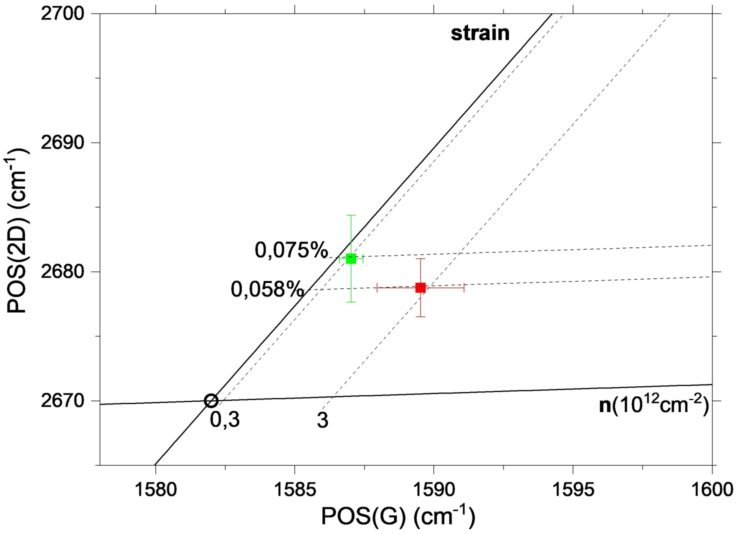

Fig. 4.33: G-2D correlation plot showing data for graphene placed in contact with SiO_2 (green dot) and when graphene is placed in contact with 4H-SiC (red dot).

The result reveals a doping concentration of $0.3 \cdot 10^{12} cm^{-2}$ when graphene was deposited on the SiO_2 layer, which increased to $3 \cdot 10^{12} cm^{-2}$ when SLG was in direct contact with 4H-SiC substrates.

4.3.4 Electrical characterization: Experimental setup and results

Experimental setup

The electrical characterization of the Schottky photodetectors based on SLG/4H-SiC involved the measurements of their current-voltage (I-V) characteristics. To perform these measurements, a probe station, as shown in Fig 4.34, equipped with a source meter (Keysight B2902A), was employed. The sample was placed on the holder of the probe station and the two electrodes, which are a Ni contact with an approximate area of $\approx 0.25\ \mu m^2$ and a Cr/Au contact with an area of $0.15\ \mu m^2$, were connected by 2 probe-tips both controlled by three-axis micromanipulators. In order to perform an accurate alignment of the probe tips into the electrodes, an optical microscope integrated into the probe station was employed. It should be noted that the probe station is enclosed in a black box which allows the measurement under dark conditions. The data acquisition involved applying a voltage bias to the graphene contact while silicon carbide was kept grounded. The source meter was connected to a PC via a GPIB cable and it was driven by codes implemented in Matlab. The I–V curve was obtained by averaging five measurements performed by varying the applied voltages repetitively across the range of -3.0 to 3.0 V.

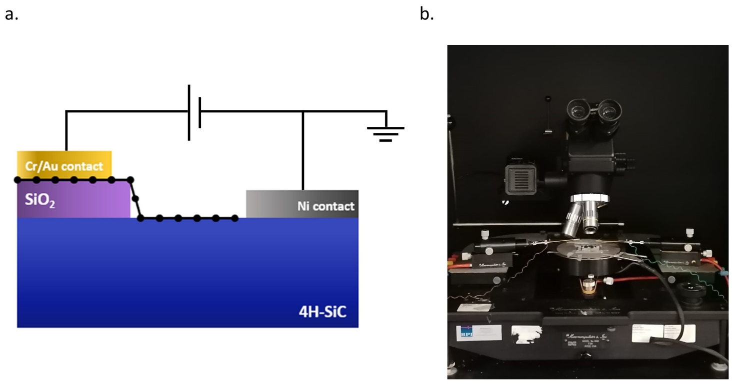

Fig. 4.34: Experimental setup of the electrical characterization: schematic illustration (a) picture of the probe station (b).

Experimental results

Firstly, the I-V characteristics under dark conditions and at room temperature were performed. The experimental results are depicted in Fig. 4.35 in semilogarithmic scale. The photodetector exhibits clear rectifying diode I-V characteristic which confirms the formation of a Schottky junction between graphene and 4H-SiC. In particular, the dark current in reverse bias at -3V is approximately 60 nA, which is more than three orders of magnitude lower than that one in the forward bias of 50 μA at 3V.

The experimental data are well-described by the thermionic theory, according to which the Schottky diode equation is expressed as follows[182]:

$$I = I_s\left(e^{\frac{q(V-R_S I)}{\eta k_B T}} - 1\right) \tag{4.4}$$

$$I_s = AA^{*}T^{2}e^{-\frac{q\Phi_B}{k_B T}} \tag{4.5}$$

where A is the active area equal to $7.85 \cdot 10^{-5} cm^2$, A^* is the Richardson constant (for n-type 4H-SiC, it is theoretically estimated to be 146 A/cm^2K^2 [183]), q is the electron charge, k_B is the Boltzmann constant, T is temperature, V is the applied voltage, R_s is the series resistance, η is the ideality factor, and Φ_B is the Schottky barrier. Many details are reported in Section 2.5.2.

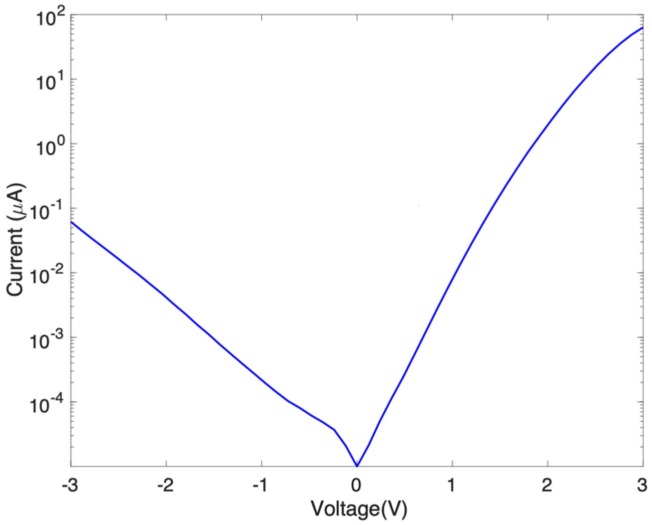

Fig. 4.35: Current-Voltage (I-V) characteristics under dark conditions and at room temperature.

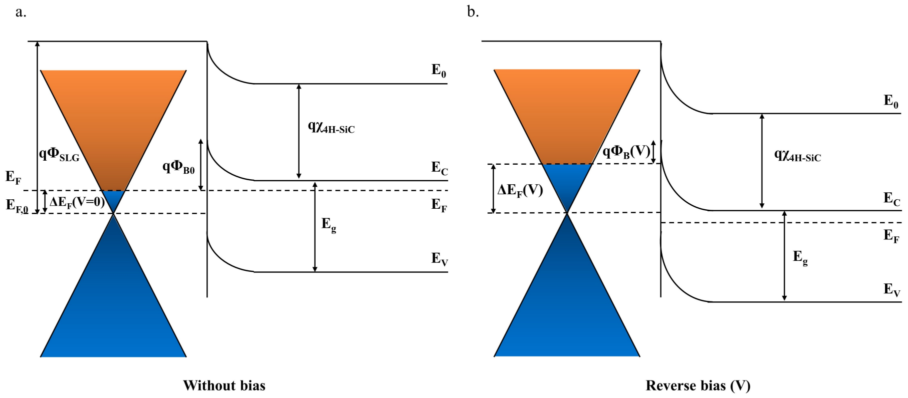

Fig. 4.36: Band diagrams of the graphene/4H-SiC n-type junction at the thermal equilibrium (a) and when a reverse bias V (b) is applied.

As shown in Section 2.5.2, the Schottky barrier exhibits a dependence on the reverse voltage, which is expressed as follows:

$$q\Phi_B(V) = q\Phi_{SLG} - q\chi_{4H-SiC} - \Delta E_F(V) \tag{4.6}$$

and at zero-bias it becomes:

$$q\Phi_{B0} = q\Phi_{SLG} - q\chi_{4H-SiC} - \Delta E_F(V = 0) \tag{4.7}$$

where Φ_{SLG}=4.6 eV[184], χ_{4H-SiC}=3.3eV[185], and the variation of Fermi level $\Delta E_F(V)$ (Fig. 4.36) can be expressed as below:

$$\Delta E_F = -sgn(n)\hbar v_F \sqrt{\pi|n|} \tag{4.8}$$

where the carrier density (n) of the graphene is defined as follows:

$$n(V) = n_0 - \sqrt{\frac{2\epsilon_{sm}}{q} N(V_{bi} - V)} \tag{4.9}$$

n_0 is the natural p-type graphene doping. By subtracting Eq. 4.6 and Eq. 4.7, it is possible to obtain the following expression:

$$q\Phi_B(V) = q\Phi_{B0} + \hbar v_F \sqrt{\pi \sqrt{\frac{2\epsilon_{sm}}{q} N V_{bi}}} - \hbar v_F \sqrt{\pi \sqrt{\frac{2\epsilon_{sm}}{q} N(V_{bi} - V)}} \tag{4.10}$$

where Φ_{B0} is the Schottky barrier without bias, $v_F = 1.1 \cdot 10^8$ cm/s is the Fermi velocity, ϵ_{sm} is the dielectric constant of the 4H-SiC, and V is the applied reverse bias. It's worth noting that in Eq 4.10 the sign of the carrier density (n), which is clearly expressed in Eq 4.8, has been considered negative, due to the n-type doping of the SiC substrate [60], and n_0 has been neglected. Indeed, the results of the Raman analysis, which was previously presented, showed that n_0 is $3 \cdot 10^{11} cm^{-2}$ which is an order of magnitude lower than $\sqrt{\frac{2\epsilon_{sm}}{q} N V_{bi}} = 3 \cdot 10^{12} cm^{-2}$. These results lead to consider n(V=0)≈ $\sqrt{\frac{2\epsilon_{sm}}{q} N V_{bi}} = 3 \cdot 10^{12} cm^{-3}$. Under this approximation, the Fermi level variation at zero-bias is evaluated by applying the Eq. 4.8 and it is $\Delta E_F(V = 0) = 0.22 eV$. Consequently, the Schottky barrier at zero-bias was extracted and its value was $\Phi_{B0} = 1.1 eV$. The extracted Φ_{B0} is consistent with other values reported in the literature [56, 186] and with the theoretical value that is $\Phi_{B0} = q\Phi_{SLG} - \chi_{4H-SiC}$=1.3 eV. Finally, the Schottky barrier as a function of reverse bias was extracted by applying the Eq. 4.10, and the results are depicted in Fig. 4.37

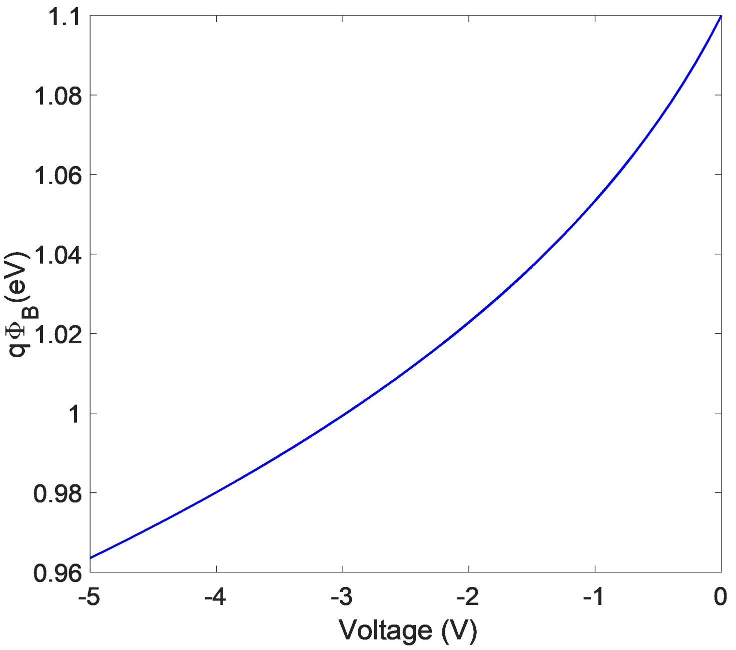

Fig. 4.37: Schottky barrier as a function of reverse bias up to 5V.

4.3.5 Optical characterization: Experimental step and results

Experimental setup

The optoelectronic characterization of the SLG/4H-SiC-based Schottky photodetector was carried out using the experimental setup depicted in Fig. 4.38. The optoelectronic characterization was performed in order to measure the photogenerated current (Fig. 4.38a) and the incident optical power (4.38b).

Firstly, the measurement of the photogenerated current was performed. It should be noted that the optical response of the photodiode has been evaluated under three distinct optical beams with wavelengths of 406 nm (L4 408-48B-TE), 633 nm (Thorlabs HRP120-1), and 785 nm (LaserSLT Diode). The experimental setup was the same for each wavelength. After a collimation step, the free-space optical beams emitted by each laser were modulated by a mechanical chopper operated at a frequency of 300Hz. Then, the modulated beam was split into two beams using a beam splitter. One beam was launched to the circular active area of the SLG/4H-SiC photodetector. The other one was collected to a microscope objective equipped with a charge-coupled device (CCD) camera. This allowed a precise alignment of the optical beam into the active area in order to achieve maximum optical response. The electrical contact to the electrode of the photodetector was performed by employing two probe-tips controlled, also in this case, by a couple of three-axis micromanipulators. The photogenerated current was amplified by a transimpedance amplifier (CVI Melles Griot 13AMP005) which also applied a voltage bias to the Schottky photodetector. Thanks to that it was possible to investigate the optical response as a function of the applied reverse bias. Furthermore, in order to enhance the measurement accuracy and minimize noise interference, a lock-in amplifier (Signal Recovery 7280 SDP) was employed.

The incident optical power measurement, whose setup is shown in Fig. 4.38b, was performed by replacing the proposed photodetector with a commercial one, which was connected to a power meter (Newport 1931), maintaining the same operation conditions. The incident optical power was measured and normalized to the active area of the device under test. It should be noted that, as explained in Section 2.3, the SLG absorbs only ≈ 2.3 %[187, 188] of the incident optical power. Therefore, the optical power absorbed by SLG was evaluated by taking into account the relationship $P_{abs} = 2.3\% P_{inc}$.

All instruments were connected to the PC with a GPIB cable in order to automatize the measurement process and to collect all data which were analyzed by an *ad-hoc* code developed in Matlab.

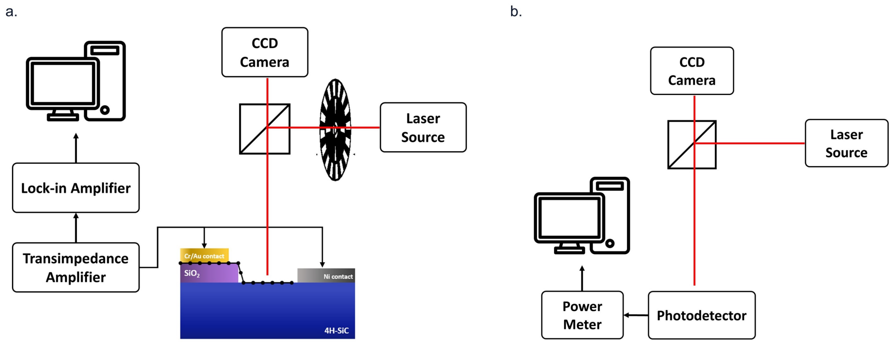

Fig. 4.38: Experimental setup of the electro-optic characterization: photogenerated current (a), and incident power (b) measurements.

Experimental results

The optoelectronic measurements were carried out at three distinct optical beam wavelengths: two in visible and one in the first window of the near-infrared spectrum range. Specifically, the optical response was investigated at λ=406 nm, λ=633 nm and λ=785 nm.

In order to evaluate the performance of the SLG/4H-SiC photodetector, the internal responsivity (R_{int}) was evaluated. This is defined as the ratio between the photocurrent I_{ph} to the absorbed optical power P_{abs}, that is $R_{int} = I_{ph}/P_{abs}$. For each wavelength, the optical response has been monitored at different optical powers and under different reverse-applied voltages.

Firstly, the electro-optic performance was characterized at zero-bias. After the device was illuminated using the optical beam, the photogenerated current and then the incident optical power were measured accurately. Specifically, the photogenerated current was evaluated as a function of the optical power absorbed by SLG. The experimental results are depicted in Fig. 4.39a,c,e for each wavelength. It's worth noting that the lock-in technique, which is employed in this case, allows to obtain highly precise measurements and the error bars are within the experimental dots, so they are not shown here. As expected, the experimental data, $I_{ph} - P_{abs}$, are suitably described by a linear curve in which the angular coefficient represents the internal responsivity at that condition of bias and wavelength. The internal responsivities evaluated at zero bias for three wavelengths are summarized in Table 4.10.

	λ=406 nm	λ=633 nm	λ=785 nm
R_{int} at 0V	3.275 mA/W	0.268 mA/W	56.73 μA/W

Table 4.10: Internal responsivity evaluated without bias for each wavelength.

Moreover, the behavior of the internal responsivity as a function of the reverse bias was evaluated. For this purpose, the photogenerated current was measured as the reverse bias increases at a fixed optical power. The experimental data are shown in Fig. 4.39b,d,f for each wavelength under a reverse bias up to approximately -5V, with steps of 0.5 V. The results exhibit a progressive increment of the responsivity as the reverse voltage increases.

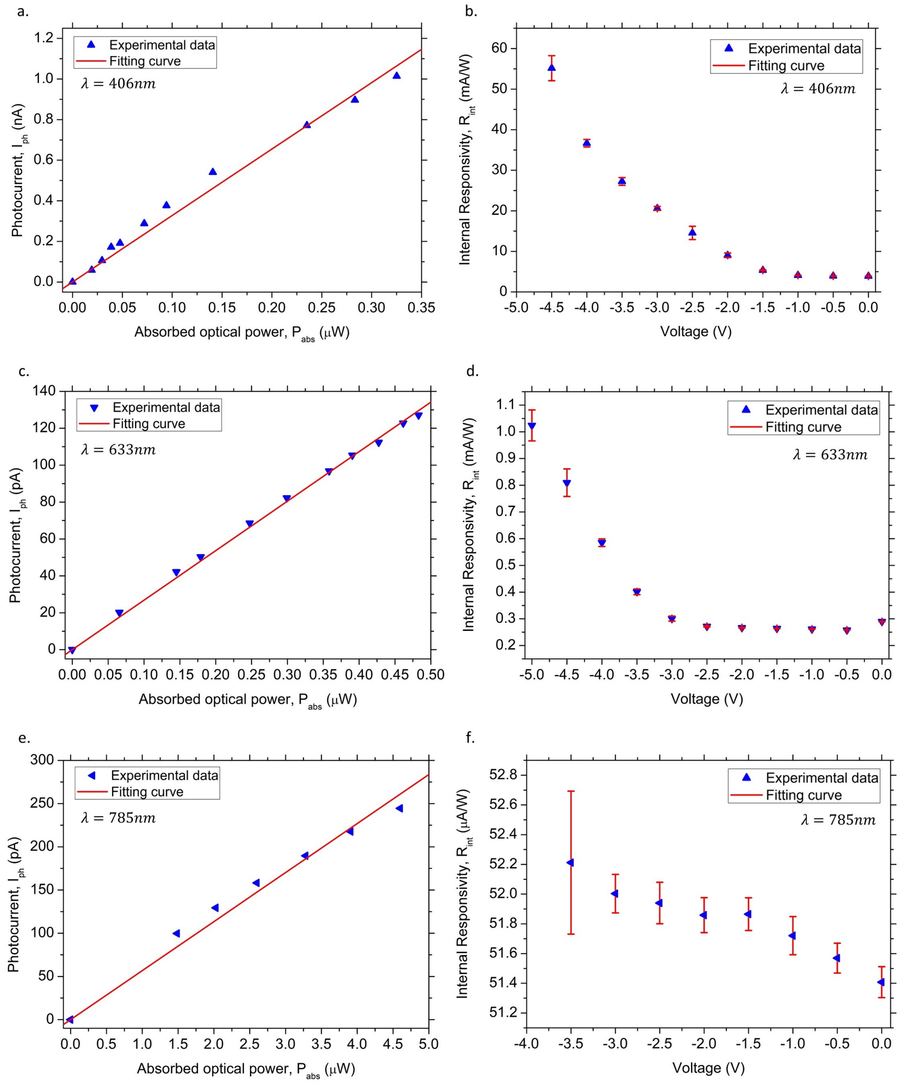

Fig. 4.39: Photogenerated current with respect to the optical power absorbed by SLG without bias (a,c,e) and internal responsivity as a function of the reverse bias (b,d,f) when the photodiode is illuminated with an optical beam at wavelength λ=406 nm, λ=633 nm, and λ=785 nm, respectively.

In the following section, a discussion of the detection mechanism that occurs in the characterized device is reported.

The optical absorption mechanism in graphene is mainly based on inter-band absorption, which occurs when an electron in the valence band reaches the conduction band after its interaction with a photon. It's worth mentioning that inter-band optical absorption manifests when half of the photon energy is higher than the graphene Fermi level ($h\nu/2 > E_F$). Conversely, when this condition is not satisfied, graphene becomes transparent to incident light. When a photon is absorbed by graphene due to the inter-band optical absorption, the photoexcited electrons can be transferred into SiC by the thermionic emission effect, which corresponds to the internal photoemission effect (IPE). As already defined in Section 2.5.2, the internal responsivity is defined as follows:

$$R_{int_{IPE}}(V) = \frac{I_{ph}^{IPE}}{P_{abs}} = K\frac{(h\nu/2)^2 - (q\Phi_B(V))^2}{(h\nu/2)^3} \tag{4.11}$$

At 406 nm, which corresponds to a photon energy of about 3.05 eV, spanning the entire range of reverse voltages in our experimental measurements (from -4.5 to 0 V), the condition $h\nu/2 > q\Phi_B(V)$ was satisfied, as it is evident in Fig. 4.37. However, the experimental results depicted in Fig. 4.39b, which represent the internal responsivity as a function of reverse bias, were not successfully fitted by Eq. 4.11. For this reason, another mechanism, which describes the transfer of photoexcited electrons into SiC to detect the signal, must be taken into account. It is the thermionic-field emission (TFE) that takes place when $E_F(V) < h\nu/2 < q\Phi_B(V)$ as illustrated in the energy band diagram of Fig. 4.40.

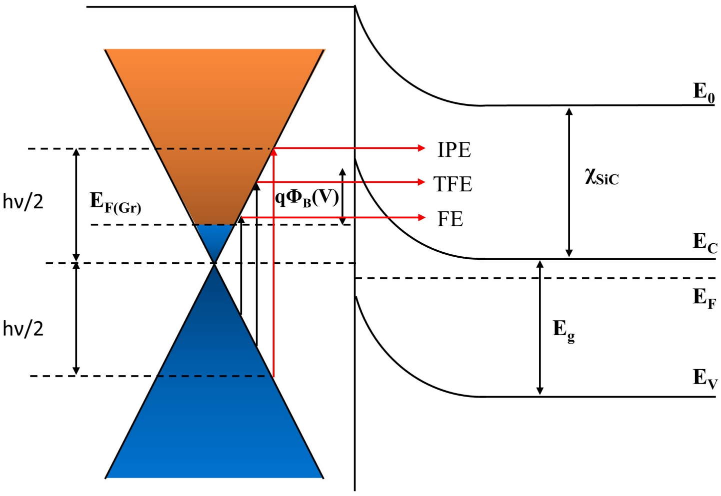

Fig. 4.40: Schematically representation of the emission effect that occurs in a Schottky junction.

TFE represents a tunneling process for photoexcited carriers, and the responsivity due to this effect can be expressed as:

$$R_{int_{TFE}}(V) = A\sqrt{qV + \frac{q\Phi_B(V)}{B}}\, e^{-\frac{q\Phi_B(V)}{C}} e^{\frac{qV}{D}} \tag{4.12}$$

where A mainly depends on the intensity and wavelength of the optical power incident on graphene while B, C, and D are energy levels defined in the TFE theory [182]. Therefore, by combining Eq. 4.11 and Eq. 4.12 and using A, B, C, D, and K as fitting parameters, the experimental data at 406 nm reported in Fig. 4.39b were successfully fitted. The experimental data and the fitted curve, whose plot is reported in Fig. 4.41, exhibit a good agreement with a large R-square of 99%. The fitting procedure gives the following parameters: A=0.31 A/W$\sqrt{eV}$, B=0.81 eV, C=0.20 eV, D=2.08 eV and K=$2.64 \cdot 10^{-3}$ (adimensional).

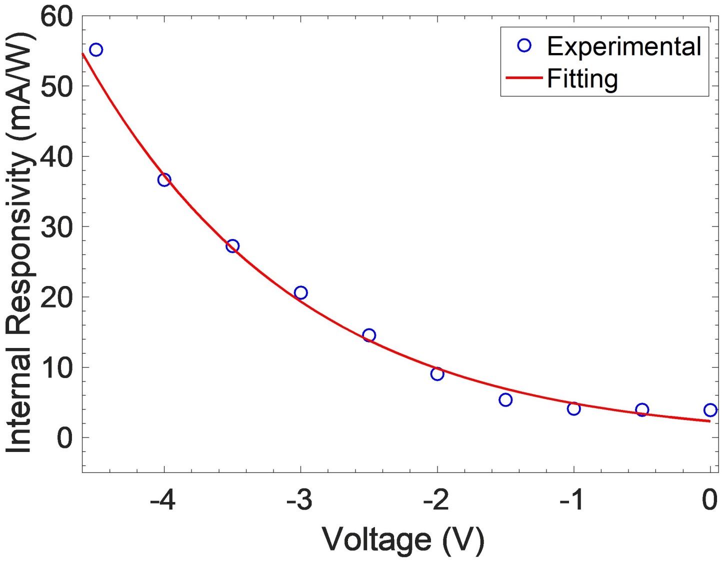

Fig. 4.41: Internal Responsivity as a function of reverse bias at a wavelength of 406 nm.

Moving our attention to the experimental responsivity at 633 nm and 785 nm, it can observed that IPE plays a limited role at 633 nm (where $h\nu/2 > q\Phi_B(V)$, $h\nu$=1.95eV) only when reverse bias is higher than -4V and it is absent at 785 nm (where $h\nu/2 > q\Phi_B(V)$, $h\nu$=1.57eV) in all range of observation. Therefore, the experimental results of Fig. 4.39d and 4.39f can not be fitted only by taking into account TFE. This means that a third charge transfer mechanism, which becomes predominant at weak photogenerated current, could have a key role. An explanation of this behavior could come from the field emission (FE) effect which is a pure tunneling process that involves the charge carriers close to the graphene Fermi level, as shown in Fig.4.40. Further investigations will have to be carried out to confirm this hypothesis.

4.4 Summary

In this chapter, demonstrations of three types of photosensors based on 4H-SiC have been demonstrated: 1) optically controlled power MOSFET 2) high-performance ultraviolet p-i-n photodetector, and 3) graphene/4H-SiC Schottky photodetector which operates in the visible and near-infrared range.

Firstly, numerical simulations were conducted to analyze an optically controlled 4H-SiC power MOSFET. This investigation introduced a novel real-time junction temperature monitoring method for the same device. Additionally, optical activation of the device was achieved through UV wavelength signals.
The monitoring technique relied on the temperature-induced refractive index change within the MOSFET-integrated Fabry-Perot (FP) cavity, exploiting multiple-beam interference. Numerical simulations at a wavelength λ=450 nm, situated within 4H-SiC's transparent window, were employed to identify thermally-induced complete FP detuning. The results indicated that in a 10-μm-thick 4H-SiC layer, a temperature variation of $\Delta T_{\pi/2} = 123.7°C$ was detected, which is vital for device health assessment and preventing overheating.

Furthermore, numerical simulations were carried out to extract the current density-voltage ($J_D - V_{DS}$) characteristics of the power MOSFET. The results demonstrated that, under sub-threshold voltage bias, the photogenerated carriers, which are induced by an optical beam (λ=285 nm), established an electron channel. Consequently, the optical drive was demonstrated.

Experimental and simulated results of a high-performance 4H-SiC ultraviolet p-i-n photodetector were reported. Experimental measurements were performed in a UV wavelength range of 210-390nm and under various reverse voltages up to 60V. The photodiode at λ=285nm exhibited a high responsivity of 0.187 A/W and a relative external quantum efficiency of 72.7% at zero bias, these results represent significant enhancements compared to prior literature. In addition, an *ad-hoc* numerical model was employed to analyze the optical response, demonstrating strong alignment between experimental and numerical results and confirming the reliability of the developed numerical model. An optimization process targeting electrical and geometrical parameters led to a substantial 31% increase in optical responsivity and a 27% in relative quantum efficiency, so the device's performance improved significantly.

In the last part of the chapter, a study focused on the fabrication and characterization of a graphene/4H-SiC-based Schottky photodetector is reported. The device exploits the sub-bandgap photodetection within a Schottky junction, which allows an optical response in both visible and near-infrared (NIR) wavelengths. Given 4H-SiC's wide bandgap (3.2 eV), intrinsic photodetection limitations exist beyond 380 nm. Electrical characterization allowed the determination of the Schottky barrier at zero bias and its behavior under reverse bias. The I-V characteristics exhibited clear rectification behaviors, with a measured Schottky barrier of $\Phi_{B0} = 1.1$ eV, consistent with literature values. Optoelectronic performance was evaluated at three different wavelengths (406 nm, 633 nm, and 785 nm), indicating internal responsivities of 3.275 mA/W, 0.268 mA/W, and 56.73 μA/W, respectively. While responsivity is limited, these findings encourage further exploration of graphene/4H-SiC photodetectors in the NIR spectral range.

5

Silicon Carbide modulators integrated on SiCOI platform

In this chapter, optical modulators based on Silicon Carbide-on-Insulator platforms are demonstrated. Firstly the design, fabrication, and characterization of a thermo-optic modulator based on amorphous-SiC (a-SiC) is presented. This modulator is based on a microring resonator integrated with a Titanium microheater. Moreover, the early simulated results, relaying on the design of a waveguide based on a p-i-n 3C-SiC platform, are discussed. Both devices operate in the near-infrared range, where SiC demonstrates exceptional properties. Specifically, SiC maintains transparency across a spectrum extending from visible to infrared wavelengths. Its substantial bandgap provides protection against nonlinear losses or generated free carrier losses at operational wavelengths within the telecommunication band of 1550 nm, where photon energies are significantly lower than the bandgap. Furthermore, within this wavelength range, SiC exhibits remarkable nonlinear optical properties, enabling functionalities such as light confinement, propagation or storage, optical modulation, and emission frequency conversion.

5.1 Design, Fabrication and Characterization of a Thermo-optic Modulator based on amorphous Silicon Carbide

As an important component of photonic integrated circuits (PICs), various thermo-optic phase shifters (TOPS) have been demonstrated so far and they have been applied for many interesting applications including switching [189, 190], sensing, advanced communication, and neural networks [191]. Typical photonic devices that implement the TOPS include microring resonators (MRRs)[192–194], Mach-Zehnder interferometers (MZIs) [9, 195], and micro-disk [196]. This kind of phase shifter allows a simple design, easy fabrication, low cost, and small footprint. However, the modulation bandwidth of TOPS is less than 100kHz, consequently, it is only suitable for applications that do not require high modulation speed [191, 197, 198].

In this section, a thermo-optic phase shifter is employed to enable an optical modulation in a Silicon Carbide-on-Insulator (SiCOI) platform based on amorphous-

SiC (a-SiC). The experimental results are included in two research papers [199, 200]. The main simulated and experimental results as well as the fabrication process are detailed in the following sections.

5.1.1 Device Concept

A thermo-optic modulator (TOM) exploits the refractive index changes of a waveguide, induced by a variation of its temperature, to modulate light passing through it. For this purpose, the TOMs include a metal heater that is placed in close proximity, generally on the top, to an optical waveguide [201].

In this case, the TOM is realized by a microring resonator based on amorphous-SiC (a-SiC). This structure is encapsulated within SiO_2, which serves as the cladding of the device. On the top of the microring resonator, separated by a SiO_2 layer, a metallic microheater based on Titanium (Ti) is placed. The schematic cross-section of the proposed device is depicted in Fig. 5.1. Briefly, when an electrical signal is applied to the microheater its temperature increases because of the Joule effect, and the generated heat is transferred to the microring. This leads to changes in the refractive index due to the thermal effect on the lattice. Consequently, the optical phase and therefore the resonance wavelength of the transmitted optical signal propagating along the microring resonator are tuned.

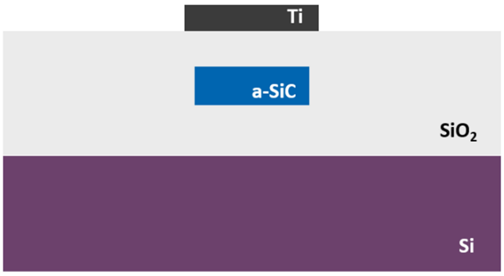

Fig. 5.1: Schematic cross-section of the thermo-optic modulator based on amorphous-SiC (a-SiC).

5.1.2 Numerical simulation of thermo-optic modulator

The a-SiC thermo-optic modulator was simulated by combining thermal and optical mode solvers in the DEVICE and MODE tools in Lumerical. The TOM was analyzed and solved using HEAT and FEM (Finite Element Eigenmode) tools. The cross-section shown in Fig. 5.1 was imported into the simulators. The thickness and width of the waveguide are 1.1 μm and 500 nm, respectively. The waveguide is defined above a 2 μm-thick SiO_2 layer which, in turn, is placed on a thick Si substrate. The metallic heater based on Ti, which is located at a distance of 1.5 μm above the waveguide, has a thickness and width of 200 nm and 1.4 μm, respectively. The geometric parameters are summarized in Table 5.1.

Parameters	Values (μm)
SiO_2 (substrate) thickness	3
a-SiC waveguide thickness	0.5
a-SiC ring width	1.1
SiO_2 (cladding) thickness	1.5
Ti (microheater) thickness	0.2
Ti (microheater) width	1.4

Table 5.1: Simulated geometric parameters of the a-SiC TOM.

The thermal simulations were carried out using the HEAT solver tool which solves the heat equation with constant power flow to the heater element. For these simulations, the temperature at the bottom of the thermal simulation region (in the Si substrate) was approximated with the ambient temperature of 300 K, and the heat convection boundary condition was applied to the top surface of the device (between the oxide layer and air above it) with fixed convection of 10 $W/m^2 \cdot K$. The details of the physical properties of each material implemented in the simulations are listed in Table 5.2, where C, ρ, and k are the specific heat capacity, density, and thermal conductivity of the material, respectively. A uniform heat source is defined across the heater. The steady-state simulations were performed and the temperature change profile in the waveguide cross-section, as shown in Fig. 5.2, was recorded. A parametric sweep on the input power from 0 to 100 mW, with steps of 10 mW, was performed and the distribution of temperature at the cross-section of the waveguide was calculated and recorded for each value of power.

Then, the temperature profile, which is a function of the input power, was imported into the optical solver wherein the same schematic cross-section was imported. The fundamental mode of the TOM as a function of the power was solved at λ=1550 nm, and the perturbation in the refractive index was calculated for the waveguide using the thermo-optic coefficient $\partial n_{SiC}/\partial T$. Therefore, the spatial temperature variations are converted into changes in the refractive index of the material. The effective refractive index was evaluated for each value of the applied power and

Material	C($J/(kg \cdot K)$)	$\rho(kg/m^3)$	k ($W/(m \cdot K)$)
Si	700	2329	156
Thermal SiO_2 (substrate)	730	2200	1.4
a-SiC	690	3216	490
PECVD SiO_2 (cladding)	650	2200	1
Ti	544	4800	17

Table 5.2: Material parameters imported in the simulation.

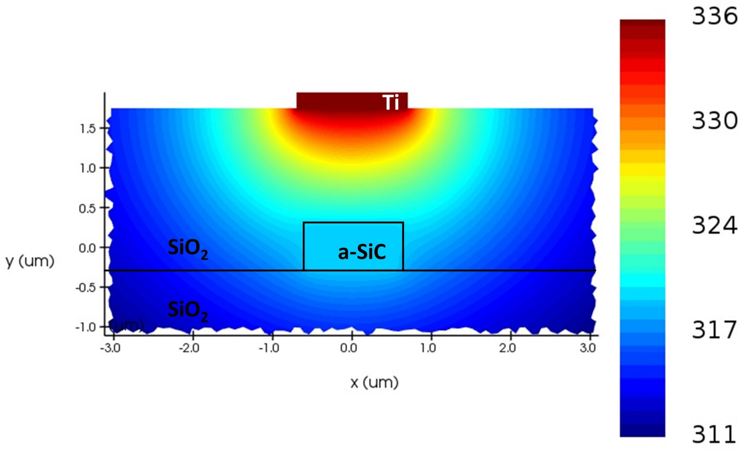

Fig. 5.2: Simulation results of the temperature distribution when the electrical power applied to the heater is P=10mW.

the relative phase shift of the optical field propagated along the waveguide was calculated by applying the formula:

$$\Delta\phi = \frac{2\pi(n_{eff} - n_{eff,0})L}{\lambda} \tag{5.1}$$

where n_{eff} and $n_{eff,0}$ are the effective refractive index with and without applied power, respectively. λ is the wavelength and L is the length of the microring resonator. According to Eq. 5.1, the phase shift as a function of the input power was evaluated, as depicted in Fig. 5.3. The results show that a $207\mu m$-long MRR requires an applied power equal to $P_\pi = 46mW$ to achieve a complete detuning, which corresponds to a phase shift $\Delta\phi = \pi$.

The dependence of the optical loss due to metal material absorption with varying SiO_2 layer thickness has been simulated. The simulation results are shown in Fig. 5.4. It's worth noting that the simulations included SiO_2 loss, while the loss contribution from the substrate wasn't included. In fact, the aim is to evaluate the impact of the only metal and not that of the surrounding materials. The simulations show that the metal absorption becomes negligible for SiO_2 thickness higher than

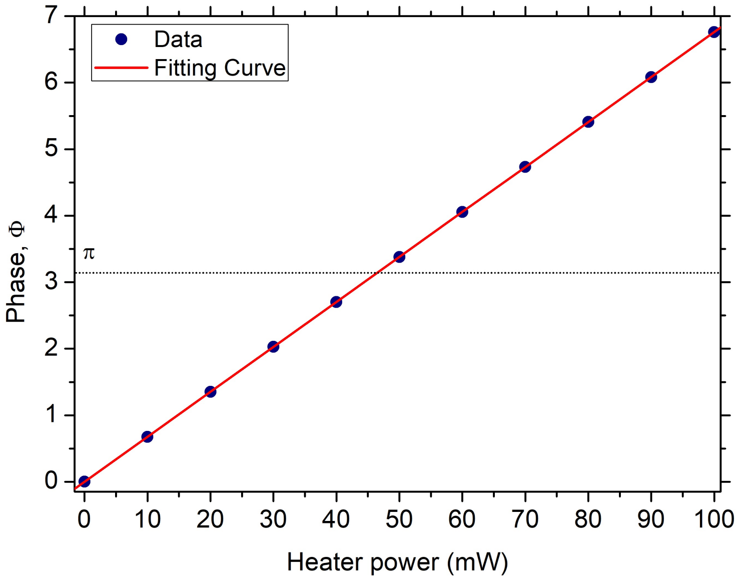

Fig. 5.3: Simulation results of the phase as a function of the applied heater power.

approximately 1 μm. The value of 1.5μm was selected in order to limit the metal absorption.

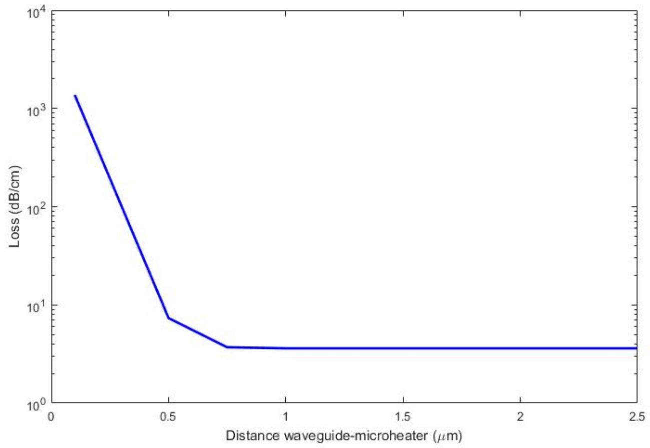

Fig. 5.4: Simulation results showing optical absorption of devices with microheater placed directly above the waveguide with different values of the gap (in SiO_2) between the waveguide and microheater.

5.1.3 Device fabrication

The designed device was fabricated with the same geometric parameters as used in the simulations. The layout design of the thermo-optic modulator, which includes the microring resonator with the microheater, was carried out using KLayout, a CAD software developed for chip design. In the same chip with dimensions 1.5 x 0.3 cm, 60 devices have been designed. Fig.5.5 shows a detail of the designed mask which clearly shows the structure of the device. Here, the blue lines represent the a-SiC microring resonator, while the red lines represent the titanium-based microheater along with its corresponding pads. The devices vary in terms of coupling gap, which ranges from 200 nm to 400 nm, and in terms of the metal width, which can be 0.7 *μm*, 1.4 *μm*, or 2 *μm*. The width of the microring is 1.1 *μm* and its outer radius is 33 *μm*. The probe pads are both 100 *μm* wide and they are separated by a 10 *μm* gap.

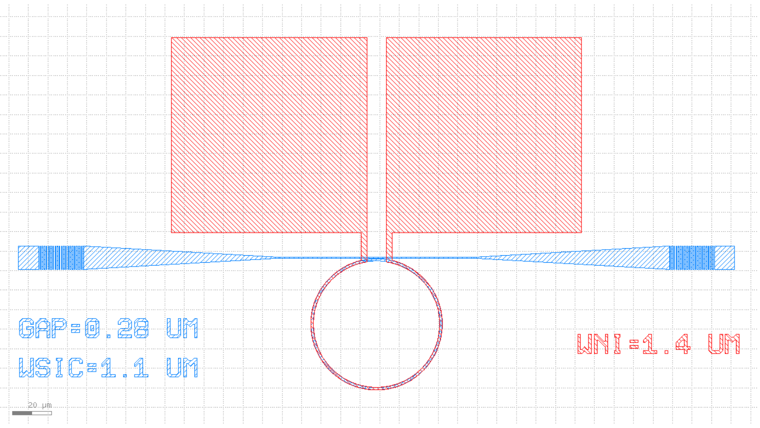

Fig. 5.5: Mask layout of the a-SiC thermo-optic modulator based on microring.

The fabrication process of the thermo-optic microheater was carried out in the cleanroom facilities at the Technical University of Denmark (DTU). The mask layout design was carried out by myself, instead, the fabrication was performed by group WISE Photonics from DTU University. Moreover, the a-SiC PECVD deposition, which was developed on a Corial D250 deposition system, was performed by the Plasma-Therm Europe Company. The detailed device fabrication process is schematically illustrated in Fig. 5.6a-g.

The fabrication began with a Si wafer with a 2.5 μm-thick thermally grown SiO_2. Subsequently, a 500 nm-thick a-SiC film (ratio Si/C of 1.473) was deposited onto it using the plasma-enhanced chemical vapor deposition (PECVD) technique (a). The first step regards the definition of the microring resonator carried out by electron beam (e-beam) lithography. For this purpose, a 300 nm-thick e-beam resist (CSAR) layer was deposited onto the sample, which was subsequently patterned by the mask layout using an e-beam writer machine (b). Following the e-beam exposure, the alumina (Al_2O_3) has been deposited and the resist was removed (c). The transferred pattern refers to the microring shape, and as a result, the a-SiC layer was etched through inductively coupled plasma reactive-ion etching (ICP-RIE) (d). After that, a 1.5 μm-thick top cladding of SiO_2 was deposited by PECVD (e). The purpose is to separate the a-SiC waveguide from the overlying metal heater in order to prevent high optical losses. Then, the heater pattern was formed on the top of the device using EBL, therefore the resist was again deposited and exposed by e-beam writer (f). Subsequently, the deposition of 200-nm thick Ti was performed using e-beam evaporation, and then a lift-off process was followed (g).

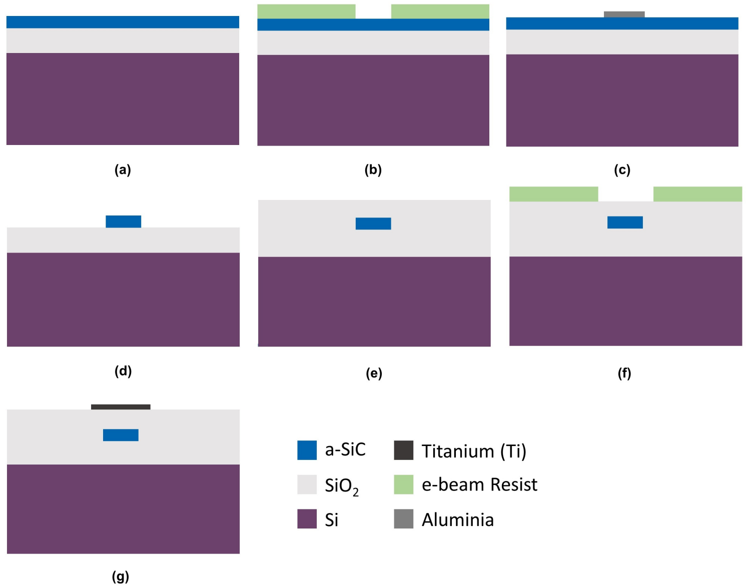

Fig. 5.6: Fabrication flow of the a-SiC thermo optic modulator.

Fig 5.9 shows optical microscope images of the thermo-optic modulator based on a-SiC after the fabrication process.

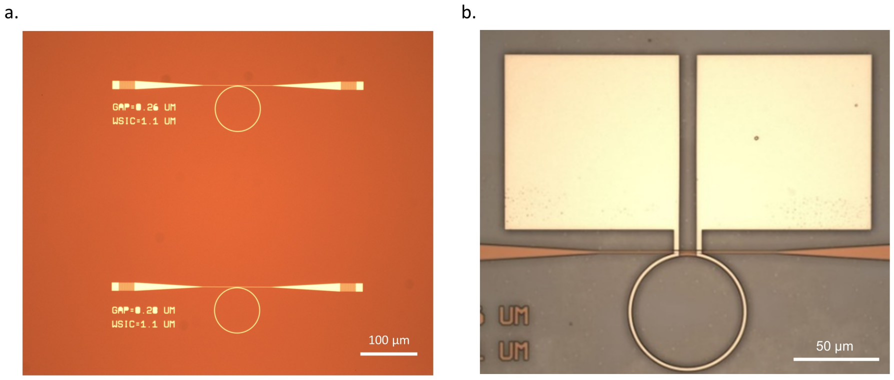

Fig. 5.7: Optical microscope image of the a-SiC thermo-optic modulator: after etching of a-SiC layer with the definition of microring structure (a) and at completed fabrication process (b).

5.1.4 Experimental setup

The measurements were conducted using the experimental setup depicted in Fig. 5.8 in which a fiber coupling system (not shown in the figure) was exploited for light coupling of the device.

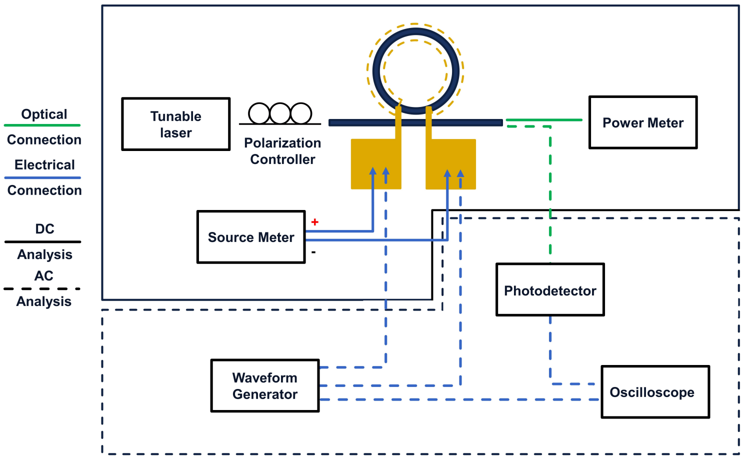

Fig. 5.8: Schematic of the experimental setup for characterization of a-SiC thermo-optic modulator based on microring resonator.

The experimental setup was divided into two parts: *DC analysis*, which has been used for measuring the transmission spectra of the microring resonator at various driving powers applied by a direct current (DC) source, and *AC analysis*, which has been used to evaluate the dynamic response of the thermo-optic modulator. The optical source was a tunable laser (TSL-550, Santec), which injected the optical beam at 0dB into the chip through a grating coupler by an SM optical fiber. A polarization controller was employed to ensure a proper input polarization to the chip optimizing the coupling efficiency. After the propagation along the microring resonator, the light is coupled with a power meter (Santec, MPM-210H) which measures the transmission spectrum. The tunable laser and power meter were connected via GPIB cable to the PC and dedicated software controls both instruments and in particular records the transmission spectrum from the power meter.

The sample was placed on a stage, and the optical fibers were supported on a metallic holder placed on a three-axis stage allowing for an accurate alignment. The first alignment was achieved by visually aligning both the input and output fibers with the waveguide using the microscope placed above the sample stage. It has allowed an approximative alignment of the SM fiber with the device, which formed an angle of approximately 75° with respect to the device's plane. At that angle, the precise position of the fiber in all three dimensions can be accurately determined by moving the holders. This process involved monitoring the signal output to maximize it in order to obtain the optimum optical response from the microring. The spectral response of all the fabricated devices was characterized in a wavelength range from 1500 nm to 1600 nm, with steps of 10 pm. Fig. 5.9 shows a labeled photograph illustrating this configuration.

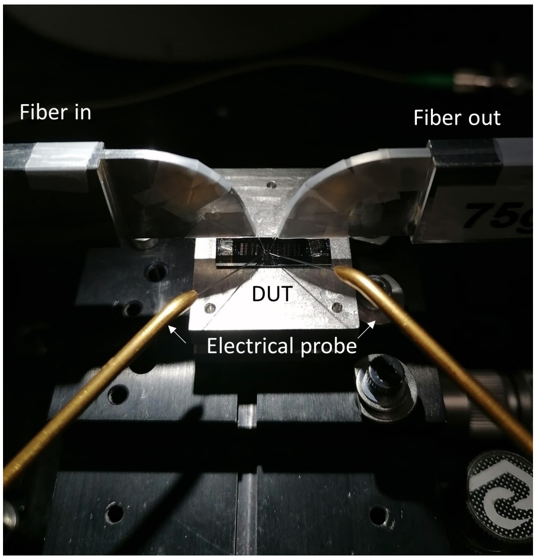

Fig. 5.9: Labelled picture of the experimental setup.

For both DC and AC measurements, two separate electrical micro-probes were employed to establish contact with the heater through two metal pads placed at its ends. Each electrical probe incorporates a 3-axis stage which enables an accurate positioning of the probe. It is worth noting that the probes were lowered before the optical alignment. Indeed, when the probes were lowered to establish electrical contact, the chip's movement could have disrupted the optical alignment. As regards the static analysis, a source meter (2450, Keithley) was used to apply voltage to the metallic heater and monitor the applied power. As the electrical contact has been established, an electrical scan ranged from 0V to 12 V, and the transmission response of the microring was collected by the power meter across the same spectral sweep for each applied voltage. On the other hand, in order to evaluate the dynamic response of the thermo-optic modulator, the wavelength of the tunable laser source was set at the resonance value around 1550 nm. Simultaneously, the heater was polarized using a pulsed electrical signal from a waveform generator (Hewlett Packard, 33120A). The output fiber was connected to a commercial NIR photodiode (Thorlabs, DET01CFC) that converts the optical modulated signal into an electrical modulated signal. The signal was collected and displayed by the oscilloscope. Finally, it was connected to the computer via a GPIB connector, and the experimental data were recorded and processed by a procedure implemented in the MATLAB environment.

5.1.5 Experimental Results

The optical loss of the a-SiC thermo-optic modulator was characterized before the investigation of its thermal tuning performance. The high-resolution spectra were measured by scanning the laser wavelength from 1500 nm to 1600 nm with a 10 pm step. Fig. 5.10 a shows the transmission spectrum of the micro-ring around 1550 nm at room temperature without bias.

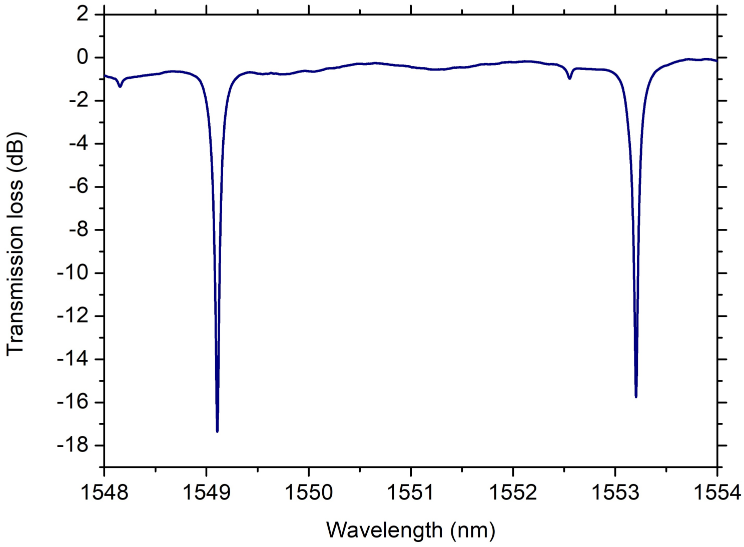

Fig. 5.10: Transmission spectrum around 1550 nm without bias.

It should be noted that the transmission spectra were measured to reveal a single-mode operation, that is fundamental transverse mode (TE). Here, the resonance peaks were observed with an extinction ratio of approximately 16 dB and a free spectral range (FSR), that is the distance between two consecutive resonance wavelength peaks, of 4.1 nm. The transmission spectrum around the 1550nm wavelength was processed using a Lorentzian fitting, and the Full Width at Half Maximum (FWHM) value was extracted. The FWHM of the a-SiC thermo-optic modulator is 119 pm. Then, according to the Eq 2.38 and 2.39, as discussed in Section 2.5.2, the loaded and the intrinsic quality factors were extracted. These values are $1.23 \cdot 10^4$ and $3 \cdot 10^4$, respectively.

To electrically characterize the thermo-optic modulator based on microring resonators, the DC response of the devices was characterized first. In this case, the phase shift of the propagated light was monitored as a function of electrical power applied to the microheater. The measurement of the transmission spectrum was performed in a range between 1500 nm to 1600 nm at room temperature. The temperature-induced effective index change of the fundamental TE mode was calculated from the measured resonance shift. Following the adjustment of the electrical probe in contact with the device and optical alignment, the transmission spectrum was recorded at zero bias for each applied voltage. Fig. 5.11 shows the transmission spectrum around the wavelength of 1550 nm at zero-bias (black line) and under different applied voltages to microheaters up to 12V. It should be noted that the resonance wavelength is red-shifted, *i.e.* towards longer wavelengths as the applied voltage increases. Indeed, as temperature increases, due to the thermo-optic effect, the refractive index and consequently the resonance wavelength increases. As a result, in order to achieve again the resonance condition, it is necessary to increase the wavelength of the optical source wavelength. These trends are in agreement with other works in literature performed for the same kind of devices [110, 193]. Furthermore, the minimum applied voltage required to achieve a high modulation depth, indicative of a high modulation effect, is 2V, which corresponds to a dissipated electrical power of 3mW. The modulation depth describes how the modulated level of the signal varies around its unmodulated level and it is defined as $M_{\%} = \frac{I_{max}-I_{min}}{I_{max}}$, where I_{max} and I_{min} are the maximum and minimum values of the transmission signal, respectively. Starting from these experimental data, the resonance wavelength at each

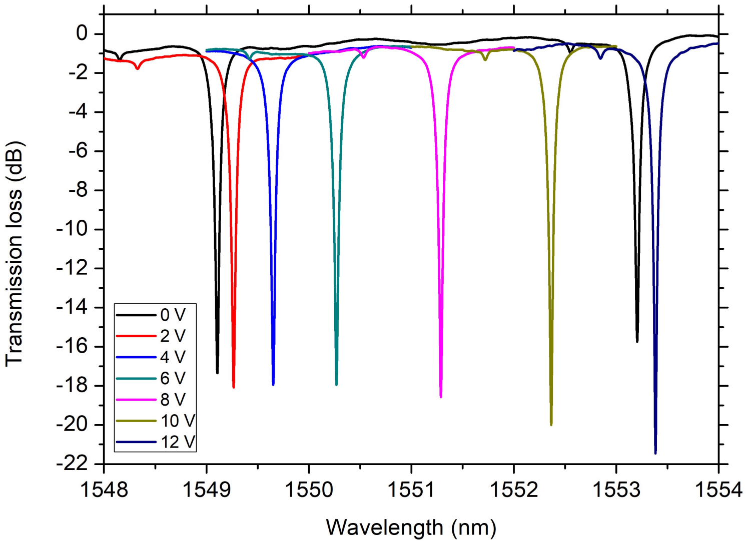

Fig. 5.11: The transmission spectra of the ring resonator at different drive voltages. The black line represents the experimental data without bias.

applied power was extracted. Using a minimum tracking code for each transmission spectrum written in MATLAB, the wavelength shift from the value at zero bias was evaluated. So, the wavelength shifts as a function of applied power with respect to the unbiased spectra were extracted, as shown in Fig. 5.12. The experimental data obtained from measurements (blue dots) were modeled with the first-order polynomial best-fits. The angular coefficient of the fitted curve represents the thermal efficiency of the modulator and it is $\eta = 52.2pm/mW$. To further analyze the thermal tuning performance of the thermo-optic modulator, the P_π, which is the power consumption necessary to detune the resonator by a phase shift of π, was evaluated. As shown in Ref [63], a complete detuning, which corresponds to a phase shift of 2π, occurs in a microring resonator within one FSR shift. For this reason, the value of P_π can be measured by applying the formula $P_\pi = \frac{FSR}{2\eta}$. As the thermal efficiency $\eta = 52.2pm/mW$ and an FSR=4.1 nm, the measured P_π is 39.24 mW.

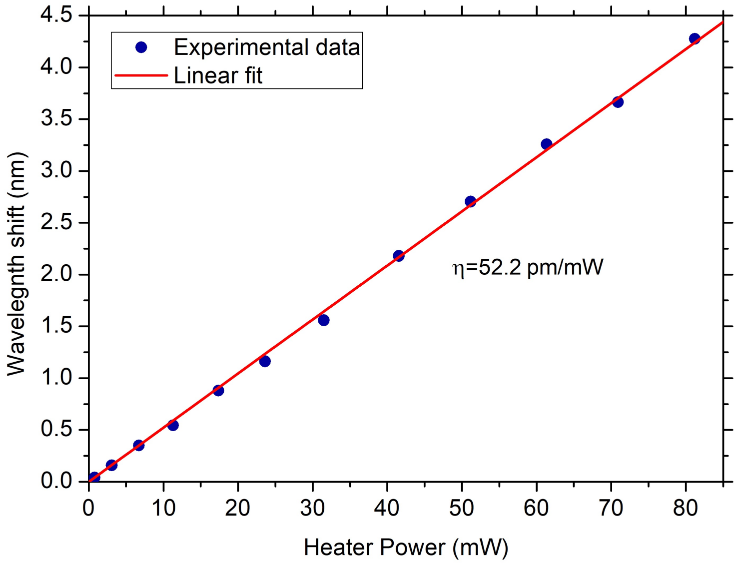

Fig. 5.12: Resonance wavelength shift as a function of the electrical power applied to the Ti microheater.

Regarding the dynamic response, a 10 kHz square-wave signal, which corresponds to the red line in the upper part of Fig. 5.13, was generated by the waveform generator to drive the Ti-based heater. It was employed to measure the dynamic response of the thermo-optic modulator. The driving electrical signal has a peak-to-peak voltage amplitude of 2V, which corresponds to an applied power of 3mW, which is the minimum value to observe an efficient modulation effect. The wavelength corresponding to the resonance at zero bias around 1550 nm was selected. While the heater was driven by the square-wave signal, the optical beam at this wavelength was injected into the microring. The transmitted optical signal was collected by a commercial photodiode. The blue line depicted at the bottom part of Fig. 5.13 describes the modulated signal.

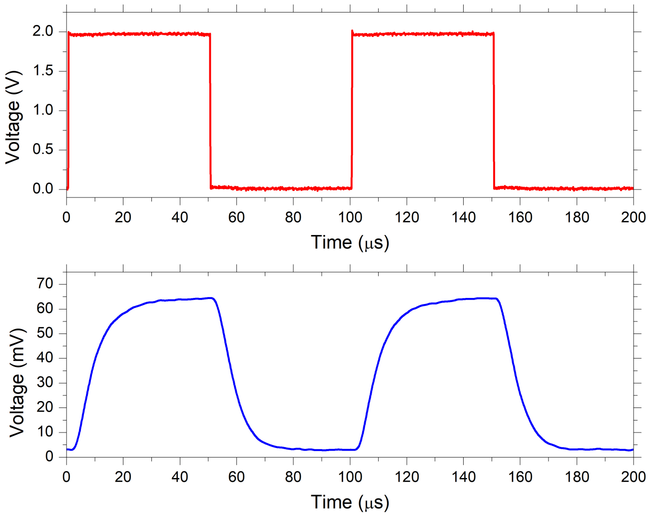

Fig. 5.13: 10kHz square electrical drive signal (top), and optical response of the a-SiC thermo-optic modulator (bottom).

To assess the performance of the thermo-optic modulator, the switching time of the modulated signal was determined. According to the 10%-90% role, the rise and fall time was evaluated. The rise time is defined as the time required for a signal to move from 10%-90% of the maximum value of the waveform, and vice-versa, the fall time is defined as the time required for a signal to move from 90%-10% of the maximum value of the waveform. The proposed thermo-optic modulator exhibits a rise and fall time of 16 μs and 13 μs, respectively.

The performance of the proposed a-SiC thermo-optic modulator based on microring is compared with other reported TO modulation devices, as shown in Table 5.3. SiC shows good performance in terms of switching time which aligns with similar devices, but due to the lower TOC of SiC compared with Si, it shows a slightly higher applied power than Si.

Based on the unique advantages of SiC as a semiconductor for integrated photonics, the proposed thermo-optic modulator based on a-SiC can be considered a good platform for the development of future photonic devices. It should be noted that the performance of the a-SiC TOM is limited mainly by heat diffusion through the SiO_2 cladding to the SiC layer and from the quality of the PECVD a-SiC.

Device	Operation wavelength (nm)	P_π power (mW)	Rise/Fall time τ (μm)
$LiNbO_3$ MRR/NiCr [202]	1550	23.2	60/53
Si MZI/TiN [203]	2000	32.3	15/15
Si MRR/Graphene [193]	1550	28	0.78/0.8
Si/TiN [201]	1500	21.4	5.6
3C-SiC MRR/NiCr [204]	1550	50	-
a-SiC MRR/Ti [*this research*]	1550	39.2	16/13

Table 5.3: Comparison between similar devices in literature with other platforms.

5.2 Prospects for 3C-SiC photonics on SOI: integrated waveguides

3C-SiC has emerged as one of the primary choices for fabricating optoelectronic devices due to the easy thin-film growth on silicon substrates by heteroepitaxial growing [95, 96]. Despite that, it has been difficult to obtain high-quality thin films due to the crystal defects associated with this approach. To overcome this limit, an alternative method, which is more complex and expensive, has been proposed. This is based on the *thinning and polished* technique described in Section 2.6. Although SiC shows many defects in the first microns of its growth, these decrease far from the interface 3C-SiC/Si. Taking this into account, this section focuses on the investigation of an optical waveguide based on a 3C-SiC p-i-n structure epitaxially growth on an SOI wafer. In this case, the optical propagating field is launched along the intrinsic layer far from the growth interface.

A first sample of the 3C-SiC p-i-n growing was performed in a 6-inch SOI wafer and the ellipsometric measurements, which results have been already discussed in section 3.1.2, were performed. Starting from these results an optimization process was performed in order to achieve an optical waveguide that was single-mode and polarization-independent. The fabrication process began with a commercially available 6-inch SOI wafer on which the 3C-SiC epitaxially growing was performed by Advanced Epi[125].

The schematic cross-section of the proposed 3C-SiC waveguide integrated into the SOI platform is depicted in Fig. 5.14. It is composed of a SOI wafer on top of which a 3C-SiC-based *p-i-n* structure is epitaxially grown. The aim is to allow the propagation of an optical field along the intrinsic layer of the *p-i-n* 3C-SiC structure. Optical simulations were performed in order to design the device. For this purpose, the schematic cross-section reported in Fig. 5.14 was implemented in MODE tool by Lumerical.

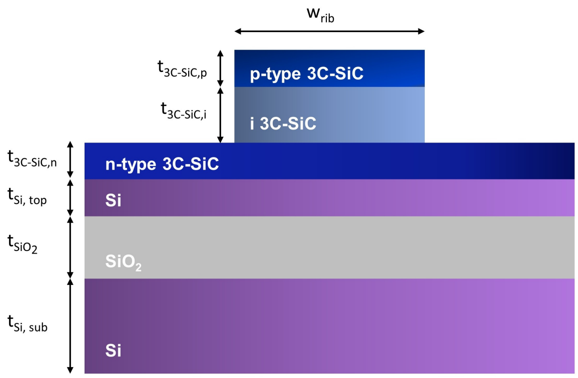

Fig. 5.14: Schematic cross-section of the p-i-n waveguide based on 3C-SiC epitaxially growth above a SOI wafer (not in scale).

According to the ellipsometric measurements reported in Section 3.1.2, which have been performed in this sample, optical simulations were carried out in order to prove the propagation of an optical field confined along the intrinsic layer based on 3C-SiC. Firstly, the best value of the Si top-layer of the SOI was chosen. Due to the low contrast of the refractive index between Si and 3C-SiC, which are 3.48 and 2.62 at λ=1550 nm respectively, a part of the optical field tends to propagate along the Si-layer. This phenomenon becomes increasingly noticeable with increasing layer thickness. To minimize this effect, the best value of the Si top-layer thickness of the SOI was evaluated. The simulated results have shown that the impact of the Si layer significantly decreased as its thickness was lower than 80 nm. For this purpose, a thickness of 50 nm was chosen. The geometry of the waveguide was defined through parametric simulations on the thickness of the three 3C-SiC layers and on the width of the rib. These simulations were performed to ensure the single-mode propagation and the polarization-independent waveguide operation. Combining several simulated results, the thickness of the slab $t_{SiC,n}$ and the top layer $t_{SiC,p}$ were assumed to be 100 nm and 50 nm, respectively. Then, the impact of the geometric parameter of the waveguide rib has been investigated. Fig. 5.15a and 5.15b show the relationships between the real part of the effective refractive index and the waveguide width for the fundamental and the first higher order modes (TE and TM) for waveguides with $t_{SiC,i}$=400nm and 500nm respectively. In both cases λ=1550 nm, $t_{SiC,n}$=100nm and $t_{SiC,p}$=50nm. The simulations were conducted for rib widths in the range 0.3 μm-2.0 μm. Comparing both results, the single mode along with polarization-independent condition was obtained when the thickness of the intrinsic layer ($t_{3C-SiC,i}$) is 500 nm and the waveguide rib width (w_{rib}) is approximatively 500 nm.

The fabrication of the designed structure started by thinning down the Si top layer of the SOI wafer from 220 nm to 50 nm, which was carried out at the clean-

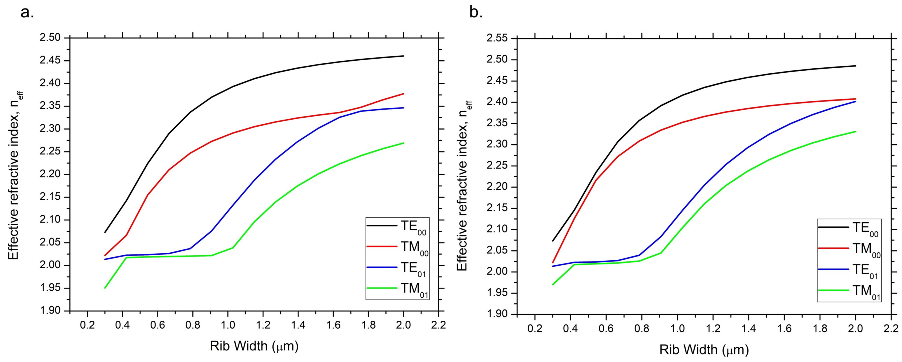

Fig. 5.15: Effective refractive index of the first four modes which propagate into the waveguide as a function of the rib width, when $t_{3C-SiC,i}$=400 nm (a) and $t_{3C-SiC,i}$=500 nm (b).

room facilities of DTU. For this purpose, dry oxidation followed by wet etching in BHF was carried out. Then, the 3C-SiC p-i-n growth was subsequently performed again. Future work involves the definition of the actual waveguide with the geometric parameters that were obtained from the simulations and its subsequent optical characterization.

Parameters	SiO_2	Si top-layer	3C-SiC		
Thickness	3 μm	50 nm	100 nm	500 nm	50 nm
Doping ($cm^{-}3$)	-	10^{19}	n-type 10^{19}	$i \approx 10^{15}$	p-type 10^{19}

Table 5.4: Geometric and optic parameter of the device layers.

5.3 Summary

In this chapter, the potential of silicon carbide for optical modulation was investigated. The design, fabrication, and characterization of a thermo-optic modulator based on amorphous silicon carbide (a-SiC) were demonstrated. It was developed into a Silicon Carbide-on-Insulator (SiCOI) platform in which an a-SiC layer was deposited via PECVD in a thermally SiO_2-on-Si substrate. The thermo-optic modulator was defined by integrating a microring resonator with a microheater based on Titanium (Ti). The geometric parameters were evaluated by performing optical simulation in Lumerical. The designed device was fabricated and characterized.

Firstly, a comprehensive optical transmission spectrum analysis was conducted across a wavelength range spanning from 1500 nm to 1600 nm. Then, in order to evaluate the static thermo-optic response of the modulator as temperature changes, the transmission spectrum was monitored under different electrical power applied to the heater up to 80 mW. As the applied voltage increased, a phase shift was induced by the refractive index change, and a red-shift in the resonance wavelength was shown, consequently. These experimental results exhibited a thermal tunability of 52.2 pm/mW.

Furthermore, the dynamic optical response of the a-SiC thermo-optic modulator was evaluated. By applying to the Ti heater a 10 kHz square wave with a peak-to-peak amplitude of 2 V, corresponding to a dissipated power of 3 mW, a large modulation depth of M=96% was measured. The switching time was also evaluated, according to 10%-90% role, and the measured rise and fall time were 16 μs and 13 μs, respectively.

Moreover, the early investigation of a waveguide based on a 3C-SiC p-i-n structure epitaxially growth in an SOI wafer was reported. Taking into account the results from the ellipsometric characterization, a 3C-SiC optical waveguide, which is single-mode and polarization-independent, was demonstrated.

6

Conclusions and Future Works

6.1 Conclusions

In this thesis, the potential of silicon carbide (SiC) as a photonics platform has been investigated. For this purpose, photonics devices based on SiC were numerically studied, fabricated, and experimentally characterized. Achieved key results include the material characterization as well as the simulation, fabrication, and characterization of photosensors operated in the ultraviolet, visible, and near-infrared range. In addition, the design, fabrication, and characterization of integrated optical modulators based on Silicon Carbide-on-Insulator platforms were performed.
More in detail, the main results can be summarized as follows.

At first, the **optical characterization of wide bandgap semiconductors** was carried out. Spectroscopic ellipsometry was conducted in several substrates including:

- n-type 4H-SiC substrates with three different doping levels (semi-insulating, $10^{18} cm^{-3}$, $10^{19} cm^{-3}$);
- a p-i-n structure based on 3C-SiC (n-type $10^{19} cm^{-3}$, intrinsic layer, p-type $10^{19} cm^{-3}$) epitaxially grown on a SOI wafer;
- a semi-insulating GaN bulk.

The experimental results were performed at room temperature in a wide spectrum range from 300 nm to 1600 nm. These results were useful for an in-depth understanding of the physics of the devices which were investigated in this thesis.

Furthermore, the **temperature dependence of the thermo-optic coefficient** ($\partial n/\partial T$) was experimentally characterized in 4H-SiC and GaN substrates. The thermo-optic coefficient (TOC) is the measurement of how the refractive index changes with temperature variations. The knowledge of the temperature dependence of the optical properties, that is the thermo-optic effect (TOE), is essential to understand the optical potential of novel materials, such as 4H-SiC and GaN. However, the investigation of the TOE for these materials is still lacking. Therefore, the experimental measurements were carried out in order to evaluate the TOCs and their temperature dependences on 4H-SiC and GaN substrates. The results were reported in a wide range of temperatures up to 500K at the fiber-optic communication wavelength of λ=1550 nm and at visible wavelength λ=632.8 nm. The experimental method was based on an interferometric technique by considering the studied samples, which are double polished at an optical grade, as a Fabry-Perot cavity. For both samples at each wavelength, the plots $\partial n/\partial T$ *vs* T was defined and the best fitting was extracted. The experimental results showed a good agreement between experimental data and the fitting curves.

The results can be helpful for the proper design of SiC/GaN-based optoelectronic and nonlinear optical devices which operate in the infrared telecommunication region and visible range, that actively use (or are affected by) the refractive index change with temperature.

The optical response of photosensors based on 4H-SiC has been investigated. Firstly, the numerical simulations of an **optically controlled 4H-SiC power MOSFET** were performed. Here, a novel real-time method for the junction temperature monitoring of the power MOSFET was proposed. It was based on the evaluation of the temperature-induced refractive index change in the MOSFET-integrated Fabry Perot cavity. This cavity is naturally defined within the structure and it is composed of the epitaxial layer sandwiched between the oxide layer and heavily-doped substrate. This technique exploited the multiple-beam interference, which occurs in an FP cavity. For this purpose, numerical simulations were performed at the wavelength λ=450 nm, which is within the transparent window of 4H-SiC, in order to monitor when the thermally-induced complete FP detuning occurs. The results showed that, in a 10 μm-thick 4H-SiC layer, a variation of $\Delta T_{\pi/2} = 123.7°C$ could be detected by monitoring the patterns of the transmission spectrum when a refractive index change of $\Delta n = 9.65 \cdot 10^{-3}$ occurs. This optical approach shows real-time junction temperature monitoring which prevents the device from overheating. This approach finds applicability in numerous power applications including signal-conditioning circuits for sensors [205] as well as in the control of switching systems based on wide bandgap semiconductors where, changes in temperature above the temperature limit, lead to a mean time to failure reduction or device disruption.

Moreover, the investigation of the optical driving of the same device has been performed. For this purpose, the photogenerated carriers by an optical beam were exploited to generate an electron channel. The numerical simulation for the extraction of the current density-voltage ($J_D - V_{DS}$) characteristics of the power MOSFET was carried out. The electro-optic simulation showed that when the device is biased with a sub-threshold voltage, the application of a UV optical beam (λ=285 nm) leads to the formation of the electron channel between drain (D) and source (S). The corresponding $J_D - V_{DS}$ characteristics were investigated under different values of the optical power density. This demonstration enables devices to work in critical environments where electromagnetic interferences may be challenging. This is attributed to the fact that it does not necessitate the application of high-frequency or high-voltage pulses to drive the gate.

Experimental and simulated results of a **high-performance 4H-SiC ultraviolet p-i-n photodetector** were illustrated. Regarding the experimental results, the optical response was measured under UV radiation (from 210 to 390nm) at different reverse voltages up to 60V. At a wavelength of λ=285 nm, the photodetector exhibits a responsivity of 0.168 A/W and a relative external quantum efficiency of 72.7 % at zero bias. It's worth noting that these values represent significant improvements compared to those reported in existing literature.

The optical response was analyzed by means of an *ad-hoc* developed numerical model. The numerical model was defined through careful finding of the physical parameters which allowed obtaining a good agreement between the experimental and numerical results. The simulations were performed in the same spectrum range of experiments and under a reverse voltage up to 60V. The experimental and theoretical results of the optical responsivity match very well, and therefore these results validate the goodness of the developed optical model.

Additionally, an optimization process was applied to enhance the photodiode's performance. This process involved the investigation of paramount parameters which were electric type such as doping concentration of n- layer, carrier lifetime as well as geometrical. The results exhibit a considerable increase in the performance of the device. In fact, the optical responsivity and the relative quantum efficiency improve by about 31% and 27%, respectively.

Although 4H-SiC photodetector in the ultraviolet range has been successfully demostrated, 4H-SiC shows an intrinsic limitation in its photodetection up to 380 nm. To extend photodetection into the visible and near-infrared spectrum, exploration of alternative device structures is essential. An encouraging strategy is integrating a two-dimensional material, like graphene, into the device. The fabrication and electrical and optical characterization of a **graphene/4H-SiC-based Schottky photodetector** was reported. The device exploits a sub-bandgap photodetection which occurs in a Schottky junction in order to enable detection in both visible and near infrared range. As it is known, 4H-SiC, due to its wide bandgap of 3.2 eV, exhibits an intrinsically limited photodetection at wavelengths up to 380 nm. The photodetector was fabricated at the CNR-Institute of Applied Sciences and Intelligent Systems (ISASI) of Naples (Italy) and the detailed fabrication process was described.

Electrical characterization, performed by the extraction of the current-voltage (I-V) characteristic in a voltage range from -3V to 3V, allowed for the determination of the Schottky barrier at zero bias and its behavior as a function of reverse bias. The I-V characteristic shows clear rectifying behaviors and the measured Schottky barrier is Φ_{B0}=1.1eV which aligns with the values reported in the literature.

In addition, the optoelectronic performance of the device was investigated at three different wavelengths: two in the visible spectrum (λ=406 nm, λ=633nm) and one in the first window of the near-infrared range(λ=785nm). For each wavelength, the internal responsivity was evaluated at zero bias and under reverse bias up to ≈ -5V. The results show at zero-bias an internal responsivity of 3.275 mA/W at 406 nm, 0.268 mA/W at 633, and 56.73 μA/W at 785 nm. Despite the limited responsivity, the results are encouraging and they open the way to a deep investigation of a new family of graphene/4H-SiC PDs operating in the NIR spectral range.

Finally, the investigation of optical modulators integrated in SiO-on-Insulator (SiCOI) platforms was performed. As a novel material, SiC is currently being investigated as a potential material for optical modulation. To date, few examples have been demonstrated on SiC-based optical modulators. Despite SiC shows a lot of advantages thanks to its exceptional physical properties, its substrate quality is still a challenge to develop advanced optical modulators. However, SiC platform has a large potential to revolutionize integrated optoelectronics.

In this context, an **amorphous-SiC (a-SiC) thermo-optic (TOM)** has been successfully demonstrated. The study consisted of its design, fabrication, and characterization. The proposed TOM, which has been fabricated at the Technical University of Denmark (DTU), was based on a microring resonator integrated with a Titanium microheater. The temperature generated by the heater, due to the Joule effect, was employed to detune the optical beam which propagated along the microring resonator, by the thermo-optic effect. The fabrication process started with a 500 nm-thick PECVD a-SiC deposited on the top of a thermally oxide Si wafer. After the realization of the microring structure, a PECVD deposition of 1.5 μm-thick SiO_2 layer was performed in order to limit the optical loss due to the metallic heater, which was deposited on the top of the structure.

Firstly, the optical characterization was carried out in a wide spectrum range from 1500 nm to 1600 nm and a quality factor of $3 \cdot 10^4$ was extracted. Then, the thermo-optic response of the device has been demonstrated by static and dynamic response. Regarding the static optical response, the investigation of the transmission spectrum for different values of voltage applied to the microheater was performed. The experimental results, which refer to a TE mode propagation at a wavelength around 1550 nm, show a progressive shift of the resonance wavelength as the applied voltage increases. The experimental data of the wavelength shift with respect the peak at zero bias was expressed as a function of the applied power and the thermal tunability of 52.2 pm/mW was extracted. In addition, a large modulation depth of 96% was demonstrated when an electrical power of 3mW was applied to the microheater.

Furthermore, this value has been employed to demonstrate the dynamic response of the thermo-optic modulator. In detail, a square-driven signal at a frequency of 10kHz was applied to the microheater when an optical beam with a wavelength of around 1550 nm was launched along the microheater. The modulated optical signal showed a rise and fall time of 16 μs and 13 μs, respectively.

Finally, an initial exploration involved the development of a **waveguide** constructed from a **3C-SiC p-i-n** structure, epitaxially grown on an SOI wafer. The simulated results, supported by experimental evaluation of the refractive index which was performed in a first prototype by spectroscopic ellipsometry, allowed for the successful design of a single-mode, polarization-independent 3C-SiC optical waveguide.

All results presented in this thesis, which are both numerical and experimental, prospect a new generation of integrated photonics devices based on SiC for applications that include photodetection, *e.g.* for sensing and optical communication, and optical modulation.

6.2 Future Works

Overall, SiC photonics represents a promising and expansive field for future research. Several possible directions for future work are outlined below.

In terms of material characterization, the exploration of wide bandgap semiconductors, such as SiC, is still lacking in the literature. Other effects, such as electro-optic or thermo-optic, and further investigations into optical properties could substantially enrich existing experimental data. This, in turn, would allow the proper design and fabrication of a new generation of both active and passive optical devices.

A novel real-time junction temperature monitoring and the optical driving of the 4H-SiC power MOSFET have been already theoretically demonstrated, and possible experimental investigation will prospect. It also paves the way for high-performance future temperature sensors. SiC photodetection in the visible spectrum range is significant, holding promise for applications in applications including sensing, biomedical, and visible optical communications. The detection of 4H-SiC in the visible and first window of the near-infrared range has been experimentally demostrated, which encourages further exploration of graphene/4H-SiC photodetectors in this field. However, the physical detection mechanism has not been fully established for all investigated wavelengths, necessitating further focused investigation. In particular, a more in-depth understanding of the physics behind the detection mechanism at wavelengths of 633 nm and 785 nm is essential.

Finally, regarding optical modulators, the experimental results show the first example in literature of a thermo-optic modulator based on a-SiC, which exhibits a large modulation depth and an appreciable switching time. Improvements in the quality of a-SiC deposition could enhance the optical performance of these devices. Additionally, exploring the same effect in crystalline forms, such as 4H-SiC, could provide further insights. Work on an electro-optic modulator based on 4H-SiC is underway, with the device design completed and the fabrication process imminent.

Another potential avenue for future work involves developing an electro-optic modulator based on the 3C-SiC-on-SOI waveguide, as demonstrated in this thesis to be single-mode and polarization-independent.

List of Publications

1. Sandro Rao, **Elisa Demetra Mallemace**, Giuliana Faggio, Mario Iodice, Giacomo Messina, and Francesco Giuseppe Della Corte. “Experimental characterization of the thermo-optic coeffi- cient vs. temperature for 4H-SiC and GaN semiconductors at the wavelength of 632 nm”. In: Scientific Reports 13.1 (2023), p. 10205.
2. Sandro Rao, **Elisa Demetra Mallemace**, and Francesco Giuseppe Della Corte. “High- Perfor- mance 4H- SiC UV p- i- n Photodiode: Numerical Simulations and Experi- mental Results”. In: Electronics 11.12 (2022), p. 1839.
3. Sandro Rao, **Elisa Demetra Mallemace**, Giuseppe Cocorullo, Giuliana Faggio, Giacomo Messina, and Della Corte. “Temperature dependence of the thermo-optic coefficient in 4H-SiC and GaN slabs at the wavelength of 1550 nm”. In: Scientific Reports 12.1 (2022), p. 4809.
4. Mohamed L Megherbi, Hichem Bencherif, Lakhdar Dehimi, **Elisa Demetra Mallemace**, Sandro Rao, Fortunato Pezzimenti, and Francesco Giuseppe Della Corte “An Efficient 4H-SiC photodiode for UV sensing applications”. In: Electronics 10.20 (2021), p. 2517.
5. Sandro Rao, **Elisa Demetra Mallemace**, Maurizio Casalino, Giuseppe Cocorullo, Lakhdar Dehimi, and Francesco Giuseppe Della Corte. “Junction temperature measurement in optically-activated power MOSFET”. In: Journal of Optics 24.3 (2022), p. 034002.
6. **Elisa Demetra Mallemace**, Sandro Rao, Maurizio Casalino, Mario Iodice, Giuliana Faggio, Giacomo Messina, and Francesco Giuseppe Della Corte. “Accurate Determination of the Temperature Dependence of the Refractive Index of 4H-SiC at the Wavelength of 632 nm”. In: Materials Science Forum. Vol. 1089. Trans Tech Publ. 2023, pp. 81–85.
7. **Elisa Demetra Mallemace**, Yaoqin Lu, Xiaodong Shi, Didier Chaussende, Vincent Tabouret, Sandro Rao, Haiyan Ou, and Francesco Giuseppe Della Corte. “Thermo-optic phase shifter based on amorphous silicon carbide”. In: EPJ Web of Conferences. Vol. 287. EDP Sciences. 2023, p. 14010.

8. **Elisa Demetra Mallemace**, Teresa Crisci, Mariano Gioffrè, Mario Medugno, Francesco Giuseppe Della Corte, Sandro Rao, and Maurizio Casalino. “Graphene/4H-SiC Schottky photodetector operat- ing in the visible spectrum range”. In: EPJ Web of Conferences. Vol. 287. EDP Sciences. 2023, p. 14006.
9. **Elisa Demetra Mallemace**, Yaoqin Lu, Xiaodong Shi, Didier Chaussende, Vincent Tabouret, S Rao, Haiyan Ou, and Francesco Giuseppe Della Corte. “Amorphous silicon-carbide modulator based on the thermo-optic effect”. In: International conference on silicon carbide and related materials. 2023.
10. **Elisa Demetra Mallemace**, Teresa Crisci, Francesco Giuseppe Della Corte, Sandro Rao, and Maurizio Casalino. “Near-Infrared Graphene/4H-SiC Schottky Photodetectors”. In: 2022 17th Conference on Ph. D Research in Microelectronics and Electronics (PRIME). IEEE. 2022, pp. 281–284.
11. Sandro Rao, **Elisa Demetra Mallemace**, Giuseppe Cocorullo, Lakhdar Dehimi, and Francesco Giuseppe Della Corte. “Junction Temperature Measurement in Optically-Controlled Power Mosfet.” In: PHOTOPTICS. 2021, pp. 110–114.

References

[1] Iraj Sadegh Amiri et al. “Introduction to photonics: Principles and the most recent applications of microstructures”. In: *Micromachines* 9.9 (2018), p. 452.

[2] David Thomson et al. “Roadmap on silicon photonics”. In: *Journal of Optics* 18.7 (2016), p. 073003.

[3] Muhammad Shahbaz, Muhammad A Butt, and Ryszard Piramidowicz. “Breakthrough in Silicon Photonics Technology in Telecommunications, Biosensing, and Gas Sensing”. In: *Micromachines* 14.8 (2023), p. 1637.

[4] Christoforos Kachris, Konstantinos Kanonakis, and Ioannis Tomkos. “Optical interconnection networks in data centers: recent trends and future challenges”. In: *IEEE Communications Magazine* 51.9 (2013), pp. 39–45.

[5] Richard A Soref. “Silicon-based optoelectronics”. In: *Proceedings of the IEEE* 81.12 (1993), pp. 1687–1706.

[6] Graham Reed et al. “Optical modulators”. In: *Integrated Photonics for Data Communication Applications*. Elsevier, 2023, pp. 69–121.

[7] Yikai Su et al. “Silicon photonic platform for passive waveguide devices: Materials, fabrication, and applications”. In: *Advanced Materials Technologies* 5.8 (2020), p. 1901153.

[8] Lirong Cheng et al. “Grating couplers on silicon photonics: Design principles, emerging trends and practical issues”. In: *Micromachines* 11.7 (2020), p. 666.

[9] Milos Nedeljkovic et al. “Mid-infrared thermo-optic modulators in SoI”. In: *IEEE Photonics Technology Letters* 26.13 (2014), pp. 1352–1355.

[10] Jian Liu, Sorin Cristoloveanu, and Jing Wan. “A Review on the Recent Progress of Silicon-on-Insulator-Based Photodetectors”. In: *physica status solidi (a)* 218.14 (2021), p. 2000751.

[11] Shawn Yohanes Siew et al. “Review of silicon photonics technology and platform development”. In: *Journal of Lightwave Technology* 39.13 (2021), pp. 4374–4389.

[12] *Yole Group*, URL: `https://www.yolegroup.com/product/report/silicon-photonics-2022/`.

[13] Giuseppe Cocorullo, FG Della Corte, and I Rendina. “Temperature dependence of the thermo-optic coefficient in crystalline silicon between room temperature and 550 K at the wavelength of 1523 nm”. In: *Applied physics letters* 74.22 (1999), pp. 3338–3340.

[14] Francesco La Via et al. “Emerging SiC Applications beyond Power Electronic Devices”. In: *Micromachines* 14.6 (2023), p. 1200.

[15] IJ Wu and GY Guo. “Second-harmonic generation and linear electro-optical coefficients of SiC polytypes and nanotubes”. In: *Physical Review B* 78.3 (2008), p. 035447.

[16] Jaime Cardenas et al. “Optical nonlinearities in high-confinement silicon carbide waveguides”. In: *Optics letters* 40.17 (2015), pp. 4138–4141.

[17] Francesco Martini and Alberto Politi. “Four wave mixing in 3C SiC ring resonators”. In: *Applied Physics Letters* 112.25 (2018), p. 251110.

[18] Tsunenobu Kimoto and James A Cooper. *Fundamentals of silicon carbide technology: growth, characterization, devices and applications*. John Wiley & Sons, 2014.

[19] Gary Lynn Harris. *Properties of silicon carbide*. 13. Iet, 1995.

[20] Houyem Abderrazak and ESBH Hmida. “Silicon carbide: synthesis and properties”. In: *Properties and applications of Silicon Carbide* (2011), pp. 361–388.

[21] Wei-Cheng Lien et al. “4H–SiC Metal–Semiconductor–Metal Ultraviolet Photodetectors in Operation of 450°C”. In: *IEEE electron device letters* 33.11 (2012), pp. 1586–1588.

[22] Eva Monroy, Franck Omnès, and FJSS Calle. “Wide-bandgap semiconductor ultraviolet photodetectors”. In: *Semiconductor science and technology* 18.4 (2003), R33.

[23] Hiroaki Sato et al. “Accurate measurements of second-order nonlinear optical coefficients of 6H and 4H silicon carbide”. In: *JOSA B* 26.10 (2009), pp. 1892–1896.

[24] Xiuru Yu et al. “Third-order optical nonlinearity in nonstoichiometric amorphous silicon carbide films”. In: *Journal of Alloys and Compounds* 794 (2019), pp. 518–524.

[25] RICHARDA Soref and BRIANR Bennett. “Electrooptical effects in silicon”. In: *IEEE journal of quantum electronics* 23.1 (1987), pp. 123–129.

[26] Keith Powell et al. “Integrated silicon carbide electro-optic modulator”. In: *Nature Communications* 13.1 (2022), p. 1851.

[27] Salvatore Musumeci and Vincenzo Barba. “Gallium Nitride Power Devices in Power Electronics Applications: State of Art and Perspectives”. In: *Energies* 16.9 (2023), p. 3894.

[28] Haneen D Jabbar, Makram A Fakhri, and Mohammed Jalal AbdulRazzaq. “Gallium nitride–based photodiode: a review”. In: *Materials Today: Proceedings* 42 (2021), pp. 2829–2834.

[29] Jose Luis Pau et al. “Optical sensors based on III-nitride photodetectors for flame sensing and combustion monitoring”. In: *Applied optics* 45.28 (2006), pp. 7498–7503.

[30] Xumin Gao et al. “Monolithic III-nitride photonic integration toward multifunctional devices”. In: *Optics Letters* 42.23 (2017), pp. 4853–4856.

[31] Qifeng Lyu, Huaxing Jiang, and Kei May Lau. “Monolithic integration of ultraviolet light emitting diodes and photodetectors on a p-GaN/AlGaN/GaN/Si platform”. In: *Optics Express* 29.6 (2021), pp. 8358–8364.

[32] Matteo Buffolo et al. “Defects and reliability of GaN-based LEDs: review and perspectives”. In: *physica status solidi (a)* 219.8 (2022), p. 2100727.

[33] Steven P DenBaars et al. “Development of gallium-nitride-based light-emitting diodes (LEDs) and laser diodes for energy-efficient lighting and displays”. In: *Acta Materialia* 61.3 (2013), pp. 945–951.

[34] Daniel Feezell and Shuji Nakamura. “Invention, development, and status of the blue light-emitting diode, the enabler of solid-state lighting”. In: *Comptes Rendus Physique* 19.3 (2018), pp. 113–133.

[35] Yanzhen Zheng et al. “Integrated gallium nitride nonlinear photonics”. In: *Laser & Photonics Reviews* 16.1 (2022), p. 2100071.

[36] Iännis Roland et al. “Near-infrared gallium nitride two-dimensional photonic crystal platform on silicon”. In: *Applied Physics Letters* 105.1 (2014).

[37] Wonbong Choi et al. “Synthesis of graphene and its applications: a review”. In: *Critical Reviews in Solid State and Materials Sciences* 35.1 (2010), pp. 52–71.

[38] Lei Liao et al. “High-κ oxide nanoribbons as gate dielectrics for high mobility top-gated graphene transistors”. In: *Proceedings of the national academy of sciences* 107.15 (2010), pp. 6711–6715.

[39] Kirill I Bolotin et al. “Ultrahigh electron mobility in suspended graphene”. In: *Solid state communications* 146.9-10 (2008), pp. 351–355.

[40] Edward McCann and Mikito Koshino. “The electronic properties of bilayer graphene”. In: *Reports on Progress in physics* 76.5 (2013), p. 056503.

[41] IW Frank et al. “Mechanical properties of suspended graphene sheets”. In: *Journal of Vacuum Science & Technology B: Microelectronics and Nanometer Structures Processing, Measurement, and Phenomena* 25.6 (2007), pp. 2558–2561.

[42] Alexander A Balandin et al. “Superior thermal conductivity of single-layer graphene”. In: *Nano letters* 8.3 (2008), pp. 902–907.

[43] Francesco Bonaccorso et al. “Graphene photonics and optoelectronics”. In: *Nature photonics* 4.9 (2010), pp. 611–622.

[44] Andrew TS Wee, Xinmao Yin, and Chi Sin Tang. *Introduction to Spectroscopic Ellipsometry of Thin Film Materials: Instrumentation, Data Analysis, and Applications*. John Wiley & Sons, 2022.

[45] Xin Mu et al. “Edge couplers in silicon photonic integrated circuits: A review”. In: *Applied Sciences* 10.4 (2020), p. 1538.

[46] Siddharth Nambiar, Purnima Sethi, and Shankar Kumar Selvaraja. “Grating-assisted fiber to chip coupling for SOI photonic circuits”. In: *Applied Sciences* 8.7 (2018), p. 1142.

[47] Riccardo Marchetti et al. “Coupling strategies for silicon photonics integrated chips”. In: *Photonics Research* 7.2 (2019), pp. 201–239.

[48] Graham T Reed. “Silicon photonics: the state of the art”. In: (2008).

[49] Vilson R Almeida, Roberto R Panepucci, and Michal Lipson. “Nanotaper for compact mode conversion”. In: *Optics letters* 28.15 (2003), pp. 1302–1304.

[50] T Shoji et al. “Low loss mode size converter from 0.3 μm square Si wire waveguides to singlemode fibres”. In: *Electronics Letters* 38.25 (2002), pp. 1669–1670.

[51] Didier Decoster and Joseph Harari. *Optoelectronic sensors*. John Wiley & Sons, 2013.

[52] Maurizio Casalino. “Internal photoemission theory: Comments and theoretical limitations on the performance of near-infrared silicon Schottky photodetectors”. In: *IEEE Journal of Quantum Electronics* 52.4 (2016), pp. 1–10.

[53] Antonio Di Bartolomeo et al. “Graphene–silicon Schottky diodes for photodetection”. In: *IEEE Transactions on Nanotechnology* 17.6 (2018), pp. 1133–1137.

[54] Teresa Crisci et al. “Mono-and Bilayer Graphene/Silicon Photodetectors Based on Optical Microcavities Formed by Metallic and Double Silicon-on-Insulator Reflectors: A Theoretical Investigation”. In: *Micromachines* 14.5 (2023), p. 906.

[55] Maurizio Casalino. “Silicon Meets Graphene for a New Family of Near-Infrared Schottky Photodetectors”. In: *Applied Sciences* 9.18 (2019), p. 3677.

[56] Sefaattin Tongay et al. “Rectification at graphene-semiconductor interfaces: zero-gap semiconductor-based diodes”. In: *Physical Review X* 2.1 (2012), p. 011002.

[57] Maurizio Casalino et al. “Vertically illuminated, resonant cavity enhanced, graphene–silicon Schottky photodetectors”. In: *ACS nano* 11.11 (2017), pp. 10955–10963.

[58] Antonio Di Bartolomeo. “Graphene Schottky diodes: An experimental review of the rectifying graphene/semiconductor heterojunction”. In: *Physics Reports* 606 (2016), pp. 1–58.

[59] Mina Amirmazlaghani et al. “Graphene-Si schottky IR detector”. In: *IEEE Journal of Quantum electronics* 49.7 (2013), pp. 589–594.

[60] Teresa Crisci, Luigi Moretti, and Maurizio Casalino. "Theoretical Investigation of Responsivity/NEP Trade-off in NIR Graphene/Semiconductor Schottky Photodetectors Operating at Room Temperature". In: *Applied Sciences* 11.8 (2021), p. 3398.

[61] Wim Bogaerts et al. "Compact wavelength-selective functions in silicon-on-insulator photonic wires". In: *IEEE Journal of Selected Topics in Quantum Electronics* 12.6 (2006), pp. 1394–1401.

[62] John Heebner, Rohit Grover, and Tarek Ibrahim. *Optical microresonator theory*. Springer, 2008.

[63] Wim Bogaerts et al. "Silicon microring resonators". In: *Laser & Photonics Reviews* 6.1 (2012), pp. 47–73.

[64] Otto Schwelb. "Transmission, group delay, and dispersion in single-ring optical resonators and add/drop filters-a tutorial overview". In: *Journal of Lightwave Technology* 22.5 (2004), pp. 1380–1394.

[65] Jaime Cardenas et al. "High q sic microresonators". In: *Optics express* 21.14 (2013), pp. 16882–16887.

[66] Yoo Seung Lee et al. "Hybrid Si-LiNbO 3 microring electro-optically tunable resonators for active photonic devices". In: *Optics letters* 36.7 (2011), pp. 1119–1121.

[67] Georgios Sinatkas et al. "Electro-optic modulation in integrated photonics". In: *Journal of Applied Physics* 130.1 (2021).

[68] Keigo Iizuka. *Elements of Photonics, Volume I: In Free Space and Special Media*. Vol. 41. John Wiley & Sons, 2002.

[69] Mingxiao Li et al. "Lithium niobate photonic-crystal electro-optic modulator". In: *Nature Communications* 11.1 (2020), p. 4123.

[70] Felix Eltes et al. "A BaTiO 3-based electro-optic Pockels modulator monolithically integrated on an advanced silicon photonics platform". In: *Journal of Lightwave Technology* 37.5 (2019), pp. 1456–1462.

[71] Zhengyuan Xu and Brian M Sadler. "Ultraviolet communications: potential and state-of-the-art". In: *IEEE Communications Magazine* 46.5 (2008), pp. 67–73.

[72] EV Gorokhov et al. "Solar-blind UV flame detector based on natural diamond". In: *Instruments and Experimental Techniques* 51.2 (2008), pp. 280–283.

[73] M Mazzillo and A Sciuto. "4H-SiC Schottky photodiodes for ultraviolet flame detection". In: *Journal of Instrumentation* 10.10 (2015), P10029.

[74] Jerzy Golimowski and Katarzyna Golimowska. "UV-photooxidation as pretreatment step in inorganic analysis of environmental samples". In: *Analytica Chimica Acta* 325.3 (1996), pp. 111–133.

[75] Joseph L Robichaud. "SiC optics for EUV, UV, and visible space missions". In: *Future EUV/UV and Visible Space Astrophysics Missions and Instrumentation*. Vol. 4854. SPIE. 2003, pp. 39–49.

[76] Antonella Sciuto et al. "Radiation hardness of 4H-SiC PN junction UV photodetector". In: *Materials* 15.1 (2021), p. 264.

[77] Antonella Sciuto et al. "On the aging effects of 4H-SiC Schottky photodiodes under high intensity mercury lamp irradiation". In: *IEEE Photonics Technology Letters* 22.11 (2010), pp. 775–777.

[78] Deepak Prasai et al. "Highly reliable silicon carbide photodiodes for visible-blind ultraviolet detector applications". In: *Journal of Materials Research* 28 (2013), pp. 33–37.

[79] Franck Omnès et al. "Wide bandgap UV photodetectors: A short review of devices and applications". In: *Gallium Nitride Materials and Devices II* 6473 (2007), pp. 111–125.

[80] Tadao Toda et al. "Operation at 700 C of 6H-SiC UV sensor fabricated using N+ implantation". In: *Japanese journal of applied physics* 43.1A (2003), p. L27.

[81] Debbie G Senesky et al. "Harsh environment silicon carbide sensors for health and performance monitoring of aerospace systems: A review". In: *IEEE Sensors Journal* 9.11 (2009), pp. 1472–1478.

[82] John F Seely et al. "Response of a SiC photodiode to extreme ultraviolet through visible radiation". In: *Optics letters* 30.23 (2005), pp. 3120–3122.

[83] Antonella Sciuto et al. "UV-A sensor based on 6H-SiC Schottky photodiode". In: *IEEE Photonics Journal* 9.1 (2017), pp. 1–10.

[84] Antoni Rogalski et al. "Ultraviolet Photodetectors: From Photocathodes to Low-Dimensional Solids". In: *Sensors* 23.9 (2023), p. 4452.

[85] G Lioliou et al. "Electrical and ultraviolet characterization of 4H-SiC Schottky photodiodes". In: *Optics express* 23.17 (2015), pp. 21657–21670.

[86] Yisong Xu et al. "High-temperature and reliability performance of 4H-SiC Schottky-barrier photodiodes for UV detection". In: *Journal of Vacuum Science & Technology B* 33.4 (2015).

[87] Feng Yan et al. "Development of ultra high sensitivity UV silicon carbide detectors". In: *Materials science forum*. Vol. 527. Trans Tech Publ. 2006, pp. 1461–1464.

[88] Xiaping Chen et al. "High-performance 4H-SiC-based ultraviolet pin photodetector". In: *Journal of Applied Physics* 102.2 (2007).

[89] Jiafa Cai et al. “High-performance 4H-SiC-based pin ultraviolet photodiode and investigation of its capacitance characteristics”. In: *Optics Communications* 333 (2014), pp. 182–186.

[90] Xiaogang Bai et al. “High detection sensitivity of ultraviolet 4H-SiC avalanche photodiodes”. In: *IEEE journal of quantum electronics* 43.12 (2007), pp. 1159–1162.

[91] Dong Zhou et al. “High-temperature single photon detection performance of 4H-SiC avalanche photodiodes”. In: *IEEE Photonics Technology Letters* 26.11 (2014), pp. 1136–1138.

[92] Lianghui Li et al. “4H–SiC avalanche photodiode linear array operating in Geiger mode”. In: *IEEE Photonics Journal* 9.5 (2017), pp. 1–7.

[93] Xiaobin Xin et al. “Demonstration of 4H-SiC UV single photon counting avalanche photodiode”. In: *Electronics Letters* 41.4 (2005), p. 1.

[94] AL Beck et al. “Geiger mode operation of ultraviolet 4H-SiC avalanche photodiodes”. In: *IEEE photonics technology letters* 17.7 (2005), pp. 1507–1509.

[95] Ailun Yi et al. “Silicon carbide for integrated photonics”. In: *Applied Physics Reviews* 9.3 (2022).

[96] Xiyuan Lu et al. “Silicon carbide microdisk resonator”. In: *Optics letters* 38.8 (2013), pp. 1304–1306.

[97] Marina Radulaski et al. “Photonic crystal cavities in cubic (3C) polytype silicon carbide films”. In: *Optics express* 21.26 (2013), pp. 32623–32629.

[98] Haiyan Ou et al. “Novel Photonic Applications of Silicon Carbide”. In: *Materials* 16.3 (2023), p. 1014.

[99] Ailun Yi et al. “Wafer-scale 4H-silicon carbide-on-insulator (4H–SiCOI) platform for nonlinear integrated optical devices”. In: *Optical Materials* 107 (2020), p. 109990.

[100] Peng Cong and Darrin J Young. “Single crystal 6H-SiC MEMS fabrication based on smart-cut technique”. In: *Journal of Micromechanics and Microengineering* 15.12 (2005), p. 2243.

[101] Lea Di Cioccio et al. “Silicon carbide on insulator formation by the Smart-Cut® process”. In: *Materials Science and Engineering: B* 46.1-3 (1997), pp. 349–356.

[102] Yi Zheng et al. “High-quality factor, high-confinement microring resonators in 4H-silicon carbide-on-insulator”. In: *Optics express* 27.9 (2019), pp. 13053–13060.

[103] Xiaodong Shi et al. “Compact low-birefringence polarization beam splitter using vertical-dual-slot waveguides in silicon carbide integrated platforms”. In: *Photonics Research* 10.1 (2022), A8–A13.

[104] Daniil M Lukin et al. “4H-silicon-carbide-on-insulator for integrated quantum and nonlinear photonics”. In: *Nature Photonics* 14.5 (2020), pp. 330–334.

[105] Tianren Fan et al. “High-Q integrated photonic microresonators on 3C-SiC-on-insulator (SiCOI) platform”. In: *Optics express* 26.20 (2018), pp. 25814–25826.

[106] Peng Xing et al. “CMOS-compatible PECVD silicon carbide platform for linear and nonlinear optics”. In: *ACS Photonics* 6.5 (2019), pp. 1162–1167.

[107] Melissa A Guidry et al. “Optical parametric oscillation in silicon carbide nanophotonics”. In: *Optica* 7.9 (2020), pp. 1139–1142.

[108] Chengli Wang et al. “High-Q microresonators on 4H-silicon-carbide-on-insulator platform for nonlinear photonics”. In: *Light: Science & Applications* 10.1 (2021), p. 139.

[109] FG Della Corte et al. “Electro-optical modulation in a 4H-SiC slab induced by carrier depletion in a Schottky diode”. In: *IEEE Photonics Technology Letters* 30.9 (2018), pp. 877–880.

[110] Li-Yang Sunny Chang, Steve Pappert, and KL Paul. “High thermo-optic tunability in PECVD silicon-rich amorphous silicon carbide”. In: *Optics letters* 48.5 (2023), pp. 1188–1191.

[111] Ivan Gueorguiev Ivanov, Anne Henry, and Erik Janzén. “Ionization energies of phosphorus and nitrogen donors and aluminum acceptors in 4 H silicon carbide from the donor-acceptor pair emission”. In: *Physical Review B* 71.24 (2005), p. 241201.

[112] G Xiao et al. “Incomplete ionization in a semiconductor and its implications to device modeling”. In: *Microelectronics Reliability* 39.8 (1999), pp. 1299–1303.

[113] Ulf Lindefelt. “A model for doping-induced band gap narrowing in 3C-, 4H-, and 6H-SiC”. In: *Materials Science and Engineering: B* 61 (1999), pp. 225–228.

[114] WTRW Shockley and WT Read Jr. “Statistics of the recombinations of holes and electrons”. In: *Physical review* 87.5 (1952), p. 835.

[115] J Dziewior and W Schmid. “Auger coefficients for highly doped and highly excited silicon”. In: *Applied Physics Letters* 31.5 (1977), pp. 346–348.

[116] Siegfried Selberherr. *Analysis and simulation of semiconductor devices*. Springer Science & Business Media, 1984.

[117] *RSoft BeamPROP*, URL: `https://www.synopsys.com/photonic-solutions/rsoft-photonic-device-tools/passive-device-beamprop.html`.

[118] *Lumerical*, URL: `https://www.lumerical.com/`.

[119] *Lumerical Device*, URL: https://www.lumerical.com/learn/news_release/lumerical-announces-device-an-advanced-tcad-optoelectronic-device-simulator/.

[120] *Lumerical Device Heat*, URL: https://optics.ansys.com/hc/en-us/articles/360034917713-HEAT.

[121] *Lumerical Mode*, URL: https://optics.ansys.com/hc/en-us/articles/360034917233-MODE-Finite-Difference-Eigenmode-FDE-solver-introduction.

[122] Zhaoming Zhu and Thomas G Brown. "Full-vectorial finite-difference analysis of microstructured optical fibers". In: *Optics express* 10.17 (2002), pp. 853–864.

[123] *Horiba*, URL: https://www.horiba.com/int/scientific/.

[124] *Crystal-Material*, URL: http://www.crystal-material.com/Substrate-Materials/list_44_1.html.

[125] *Advanced Epi*, URL: https://advancedepi.com/.

[126] *SOITEC*, URL: https://www.soitec.com/en/.

[127] E Hecht. *Optics 4th ed. A. Black, ed*. 2002.

[128] Naoki Watanabe, Tsunenobu Kimoto, and Jun Suda. "Thermo-optic coefficients of 4H-SiC, GaN, and AlN for ultraviolet to infrared regions up to 500 C". In: *Japanese Journal of Applied Physics* 51.11R (2012), p. 112101.

[129] Peter TB Shaffer. "Refractive index, dispersion, and birefringence of silicon carbide polytypes". In: *Applied optics* 10.5 (1971), pp. 1034–1036.

[130] Hisashi Yoshikawa Hisashi Yoshikawa and Sadao Adachi Sadao Adachi. "Optical constants of ZnO". In: *Japanese Journal of Applied Physics* 36.10R (1997), p. 6237.

[131] Steven R Bowman et al. "Broadband measurements of the refractive indices of bulk gallium nitride". In: *Optical Materials Express* 4.7 (2014), pp. 1287–1296.

[132] Sandro Rao et al. "Experimental characterization of the thermo-optic coefficient vs. temperature for 4H-SiC and GaN semiconductors at the wavelength of 632 nm". In: *Scientific Reports* 13.1 (2023), p. 10205.

[133] Sandro Rao et al. "Temperature dependence of the thermo-optic coefficient in 4H-SiC and GaN slabs at the wavelength of 1550 nm". In: *Scientific Reports* 12.1 (2022), p. 4809.

[134] Elisa Demetra Mallemace et al. "Accurate Determination of the Temperature Dependence of the Refractive Index of 4H-SiC at the Wavelength of 632 nm". In: *Materials Science Forum*. Vol. 1089. Trans Tech Publ. 2023, pp. 81–85.

[135] Po Dong et al. “Wavelength-tunable silicon microring modulator”. In: *Optics express* 18.11 (2010), pp. 10941–10946.

[136] Nabeel A Riza, Muzzamil Arain, and Frank Perez. “6-H single-crystal silicon carbide thermo-optic coefficient measurements for ultrahigh temperatures up to 1273 K in the telecommunications infrared band”. In: *Journal of applied physics* 98.10 (2005).

[137] R De Nalda et al. “Limits to the determination of the nonlinear refractive index by the Z-scan method”. In: *JOSA B* 19.2 (2002), pp. 289–296.

[138] V Anjos et al. “Thermal-lens and photo-acoustic methods for the determination of SiC thermal properties”. In: *Microelectronics journal* 36.11 (2005), pp. 977–980.

[139] P Ščajev and K Jarašiūnas. “Application of a time-resolved four-wave mixing technique for the determination of thermal properties of 4H–SiC crystals”. In: *Journal of Physics D: Applied Physics* 42.5 (2009), p. 055413.

[140] Hans Joachim Eichler, Peter Günter, and Dieter W Pohl. *Laser-induced dynamic gratings*. Vol. 50. Springer, 2013.

[141] Chunhua Xu et al. “Temperature dependence of refractive indices for 4H-and 6H-SiC”. In: *Journal of Applied Physics* 115.11 (2014).

[142] Francesco G Della Corte et al. “Temperature dependence of the thermo-optic coefficient of InP, GaAs, and SiC from room temperature to 600 K at the wavelength of 1.5 μm”. In: *Applied Physics Letters* 77.11 (2000), pp. 1614–1616.

[143] Masashi Nakabayashi et al. “Precise determination of thermal expansion coefficients observed in 4H-SiC single crystals”. In: *Materials science forum*. Vol. 527. Trans Tech Publ. 2006, pp. 699–702.

[144] Robert R Reeber and Kai Wang. “Lattice parameters and thermal expansion of GaN”. In: *Journal of Materials Research* 15.1 (2000), pp. 40–44.

[145] *Thorlabs-DET210/M High Speed Si Photo Detector, 1ns Rise Time, Metric*. URL: https://www.thorlabs.com/thorproduct.cfm?partnumber=DET210/M.

[146] *Thorlabs-PDA10CS-EC InGaAs Switchable Gain Amplified Detector*, URL: https://www.thorlabs.com/thorproduct.cfm?partnumber=PDA10CS-EC.

[147] Sandro Rao et al. “Junction temperature measurement in optically-activated power MOSFET”. In: *Journal of Optics* 24.3 (2022), p. 034002.

[148] Sandro Rao et al. “Junction Temperature Measurement in Optically-Controlled Power Mosfet.” In: *PHOTOPTICS*. 2021, pp. 110–114.

[149] Ridwanullahi Isa et al. “Junction Temperature Optical Sensing Techniques for Power Switching Semiconductors: A Review”. In: *Micromachines* 14.8 (2023), p. 1636.

[150] Bangbing Shi et al. “Junction temperature measurement method for power MOSFETs using turn-on delay of impulse signal”. In: *IEEE Transactions on Power Electronics* 33.6 (2017), pp. 5274–5282.

[151] Maxime Berthou, Philippe Godignon, and Jose Millan. “Monolithically integrated temperature sensor in silicon carbide power MOSFETs”. In: *IEEE Transactions on Power Electronics* 29.9 (2013), pp. 4970–4977.

[152] Fausto Stella et al. “Online junction temperature estimation of SiC power MOSFETs through on-state voltage mapping”. In: *IEEE Transactions on Industry Applications* 54.4 (2018), pp. 3453–3462.

[153] Giovanni Pangallo et al. “Power MOSFET intrinsic diode as a highly linear junction temperature sensor”. In: *IEEE Sensors Journal* 19.23 (2019), pp. 11034–11040.

[154] David L Blackburn. “Temperature measurements of semiconductor devices-a review”. In: *Twentieth Annual IEEE Semiconductor Thermal Measurement and Management Symposium (IEEE Cat. No. 04CH37545)*. IEEE. 2004, pp. 70–80.

[155] Chin C Lee and Jeong Park. “Temperature measurement of visible light-emitting diodes using nematic liquid crystal thermography with laser illumination”. In: *IEEE Photonics Technology Letters* 16.7 (2004), pp. 1706–1708.

[156] Makoto Horiuchi et al. “Development of junction temperature estimation system for light-emitting LED using pulsed-laser Raman scattering”. In: *Journal of Solid State Lighting* 2.1 (2015), pp. 1–7.

[157] Arno Keppens et al. “Modeling high power light-emitting diode spectra and their variation with junction temperature”. In: *Journal of applied physics* 108.4 (2010).

[158] Z Vaitonis, P Vitta, and A Žukauskas. “Measurement of the junction temperature in high-power light-emitting diodes from the high-energy wing of the electroluminescence band”. In: *Journal of Applied Physics* 103.9 (2008).

[159] Francesco G Della Corte et al. “Numerical simulation study of a low breakdown voltage 4H-SiC MOSFET for photovoltaic module-level applications”. In: *IEEE Transactions on Electron Devices* 65.8 (2018), pp. 3352–3360.

[160] Mohamed L Megherbi et al. “An Efficient 4H-SiC photodiode for UV sensing applications”. In: *Electronics* 10.20 (2021), p. 2517.

[161] SP Karanth et al. “Electro-optical performance study of 4H-SiC/Pd Schottky UV photodetector array for space applications”. In: *IEEE Transactions on Electron Devices* 67.8 (2020), pp. 3242–3249.

[162] John A Edmond, Hua-Shuang Kong, and Calvin H Carter Jr. “Blue LEDs, UV photodiodes and high-temperature rectifiers in 6H-SiC”. In: *Physica B: Condensed Matter* 185.1-4 (1993), pp. 453–460.

[163] Antonella Sciuto et al. “High responsivity 4H-SiC Schottky UV photodiodes based on the pinch-off surface effect”. In: *Applied physics letters* 89.8 (2006).

[164] Bin Chen et al. “Analysis of temperature-dependent characteristics of a 4H-SiC metal-semiconductor-metal ultraviolet photodetector”. In: *Chinese Science Bulletin* 57 (2012), pp. 4427–4433.

[165] BK Ng et al. “Multiplication and excess noise characteristics of thin 4H-SiC UV avalanche photodiodes”. In: *IEEE Photonics Technology Letters* 14.9 (2002), pp. 1342–1344.

[166] Qiugui Zhou et al. “Proton-implantation-isolated 4H-SiC avalanche photodiodes”. In: *IEEE Photonics Technology Letters* 21.23 (2009), pp. 1734–1736.

[167] Stéphane Biondo et al. “Influence on electrical characteristics of the design of 4H-SiC ultraviolet photodetectors: Theoretical analysis and simulations”. In: *Journal of Applied Physics* 111.2 (2012).

[168] A Galeckas et al. “Auger recombination in 4H-SiC: Unusual temperature behavior”. In: *Applied Physics Letters* 71.22 (1997), pp. 3269–3271.

[169] Michael E Levinshtein et al. “" Paradoxes" of carrier lifetime measurements in high-voltage SiC diodes”. In: *IEEE Transactions on Electron Devices* 48.8 (2001), pp. 1703–1710.

[170] Tesfaye Ayalew et al. “Modeling of lattice site-dependent incomplete ionization in α-SiC devices”. In: *Materials Science Forum*. Vol. 483. Trans Tech Publ. 2005, pp. 845–848.

[171] Stefan Zollner et al. “Dielectric functions of bulk 4H and 6H SiC and spectroscopic ellipsometry studies of thin SiC films on Si”. In: *Journal of applied physics* 85.12 (1999), pp. 8353–8361.

[172] SG Sridhara, RP Devaty, and WJ Choyke. “Absorption coefficient of 4H silicon carbide from 3900 to 3250 Å”. In: *Journal of applied physics* 84.5 (1998), pp. 2963–2964.

[173] Sandro Rao, Elisa D Mallemace, and Francesco G Della Corte. “High- Performance 4H- SiC UV p- i- n Photodiode: Numerical Simulations and Experimental Results”. In: *Electronics* 11.12 (2022), p. 1839.

[174] Bahaa EA Saleh and Malvin Carl Teich. *Fundamentals of photonics*. john Wiley & sons, 2019.

[175] Alex Burenkov, Christian D Matthus, and Tobias Erlbacher. “Optimization of 4H-SiC UV photodiode performance using numerical process and device simulation”. In: *IEEE Sensors Journal* 16.11 (2016), pp. 4246–4252.

[176] Elisa D Mallemace et al. “Graphene/4H-SiC Schottky photodetector operating in the visible spectrum range”. In: *EPJ Web of Conferences*. Vol. 287. EDP Sciences. 2023, p. 14006.

[177] Elisa Demetra Mallemace et al. "Near-Infrared Graphene/4H-SiC Schottky Photodetectors". In: *2022 17th Conference on Ph. D Research in Microelectronics and Electronics (PRIME)*. IEEE. 2022, pp. 281–284.

[178] TMG Mohiuddin et al. "Uniaxial strain in graphene by Raman spectroscopy: G peak splitting, Grüneisen parameters, and sample orientation". In: *Physical Review B* 79.20 (2009), p. 205433.

[179] Jakob Zabel et al. "Raman spectroscopy of graphene and bilayer under biaxial strain: bubbles and balloons". In: *Nano letters* 12.2 (2012), pp. 617–621.

[180] Anindya Das et al. "Monitoring dopants by Raman scattering in an electrochemically top-gated graphene transistor". In: *Nature nanotechnology* 3.4 (2008), pp. 210–215.

[181] Ji Eun Lee et al. "Optical separation of mechanical strain from charge doping in graphene". In: *Nature communications* 3.1 (2012), p. 1024.

[182] Simon M Sze, Yiming Li, and Kwok K Ng. *Physics of semiconductor devices*. John wiley & sons, 2021.

[183] Akira Itoh, Tsunenobu Kimoto, and Hiroyuki Matsunami. "Excellent reverse blocking characteristics of high-voltage 4H-SiC Schottky rectifiers with boron-implanted edge termination". In: *IEEE Electron Device Letters* 17.3 (1996), pp. 139–141.

[184] Samira Naghdi, Gonzalo Sanchez-Arriaga, and Kyong Yop Rhee. "Tuning the work function of graphene toward application as anode and cathode". In: *Journal of Alloys and Compounds* 805 (2019), pp. 1117–1134.

[185] Michael Wiets, Martin Weinelt, and Thomas Fauster. "Electronic structure of SiC (0001) surfaces studied by two-photon photoemission". In: *Physical Review B* 68.12 (2003), p. 125321.

[186] S Sonde et al. "Electrical properties of the graphene/4 H-SiC (0001) interface probed by scanning current spectroscopy". In: *Physical Review B* 80.24 (2009), p. 241406.

[187] Rahul Raveendran Nair et al. "Fine structure constant defines visual transparency of graphene". In: *science* 320.5881 (2008), pp. 1308–1308.

[188] Jahan M Dawlaty et al. "Measurement of the optical absorption spectra of epitaxial graphene from terahertz to visible". In: *Applied Physics Letters* 93.13 (2008).

[189] Francesco G Della Corte et al. "Modulation speed improvement in a Fabry–Perot thermo-optical modulator through a driving signal optimization technique". In: *Optical Engineering* 48.7 (2009), pp. 074601–074601.

[190] Giuseppe Cocorullo et al. “Thermo-optical modulation at/spl lambda/= 1.5 μm in an/spl alpha/-SiC-/spl alpha/-Si-/spl alpha/-SiC planar guided-wave structure”. In: *IEEE Photonics Technology Letters* 8.7 (1996), pp. 900–902.

[191] Shengping Liu et al. “Thermo-optic phase shifters based on silicon-on-insulator platform: State-of-the-art and a review”. In: *Frontiers of Optoelectronics* 15.1 (2022), p. 9.

[192] Biswajeet Guha, Jaime Cardenas, and Michal Lipson. “Athermal silicon microring resonators with titanium oxide cladding”. In: *Optics express* 21.22 (2013), pp. 26557–26563.

[193] Sheng Gan et al. “A highly efficient thermo-optic microring modulator assisted by graphene”. In: *Nanoscale* 7.47 (2015), pp. 20249–20255.

[194] Hongyan Yu and Feng Qiu. “Compact thermo-optic modulator based on a titanium dioxide micro-ring resonator”. In: *Optics Letters* 47.8 (2022), pp. 2093–2096.

[195] Folkert Horst et al. “Cascaded Mach-Zehnder wavelength filters in silicon photonics for low loss and flat pass-band WDM (de-) multiplexing”. In: *Optics express* 21.10 (2013), pp. 11652–11658.

[196] Longhai Yu et al. “Thermally tunable silicon photonic microdisk resonator with transparent graphene nanoheaters”. In: *Optica* 3.2 (2016), pp. 159–166.

[197] Akio Sugita et al. “Bridge-suspended silica-waveguide thermo-optic phase shifter and its application to Mach-Zehnder type optical switch”. In: *IEICE TRANSACTIONS (1976-1990)* 73.1 (1990), pp. 105–109.

[198] Chaoran Huang et al. “On-chip programmable nonlinear optical signal processor and its applications”. In: *IEEE Journal of Selected Topics in Quantum Electronics* 27.2 (2020), pp. 1–11.

[199] Elisa D Mallemace et al. “Thermo-optic phase shifter based on amorphous silicon carbide”. In: *EPJ Web of Conferences*. Vol. 287. EDP Sciences. 2023, p. 14010.

[200] ED Mallemace et al. “Amorphous silicon-carbide modulator based on the thermo-optic effect”. In: *International conference on silicon carbide and related materials*. 2023.

[201] Maxime Jacques et al. “Optimization of thermo-optic phase-shifter design and mitigation of thermal crosstalk on the SOI platform”. In: *Optics express* 27.8 (2019), pp. 10456–10471.

[202] Xiaoyue Liu et al. “Highly efficient thermo-optic tunable micro-ring resonator based on an LNOI platform”. In: *Optics letters* 45.22 (2020), pp. 6318–6321.

[203] Li Shen et al. "High-Performance Silicon 2x2 Thermo-Optic Switch for the 2-μm Wavelength Band". In: *IEEE Photonics Journal* 11.4 (2019), pp. 1–6.

[204] Xi Wu et al. "High-Q microresonators integrated with microheaters on a 3C-SiC-on-insulator platform". In: *Optics letters* 44.20 (2019), pp. 4941–4944.

[205] Sandro Rao, Giovanni Pangallo, and Francesco Giuseppe Della Corte. "Integrated amorphous silicon pin temperature sensor for CMOS photonics". In: *Sensors* 16.1 (2016), p. 67.